Rotational Dynamic Stability

Research and Development Report

Prepared for NARCON 2024

Jan 26-28, 2024

Rev 1.2

Sep 21, 2024

Thomas B Fetter

NAR 15551

C Division

© 2024
Thomas B Fetter
ALL RIGHTS RESERVED

Summary

The objective of this work is to understand why model rockets are more stable than predicted by the rotational dynamics equation developed by Mandell in *Topics in Advanced Model Rocketry* (Mandell, Caporaso, & Bengen, 1973). A 2-D rotational dynamics and flight trajectory model is shown to agree with the observed rotational behavior of typical model rocket flights. That model is then used to determine which parameters impact the rocket's rotational stability. Coupling between the rotational dynamics equation and the X-axis equation of motion through the lift force term is found to increase the rotational dynamic stability. The side-to-side flight path motion of the rocket due to the lift force is shown to add to the rotational damping term by increasing the effective angle of attack. Two "coupled" linearized rotational dynamics equations that include the parameters necessary to predict the actual rotational stability are developed and analyzed in both the time and frequency domains. The damping ratio from the second order differential equations is shown to be a good measure of the rotational dynamic stability. The coupled linearized model is then used to analyze the rocket's rotational dynamic stability behavior through a series of sensitivity analyses to key rocket design parameters. The root locus technique is used to show what happens to the rotational stability as the center of pressure crosses over the center of gravity and the rocket becomes unstable. Finally, the rotational dynamics models are verified using a detailed analysis of measured flight data from a rocket designed specifically for testing the models' results. The side-to-side motion of the rocket, isolated from the accelerometer data is shown to match closely in amplitude and phase the side-to-side motion calculated in the 2-D rotational dynamics and flight trajectory model.

Table of Contents

1 Introduction

1.1 Objective and Approach

The objective of this work is to understand why model rockets are so stable. Stability in this case refers to the rotational oscillation that occurs as the rocket leaves the launch guide and is subject to a step in the velocity of the lateral wind. The less the rocket oscillates before settling to a final rotational angle, the more stable it is. Model rockets typically oscillate fewer than 5-10 cycles, which is consistent with a second order differential equation damping ratio on the order of 0.05. Mandell's rotational dynamics equation (a second order differential equation), using aerodynamic parameters calculated by the Barrowman equations, predicts a damping ratio on the order of 0.01, which would result in large oscillations over a significant portion of a rocket's flight. This work is focused on understanding the discrepancy between the modeled and observed behavior and understanding the mechanisms behind the model rocket's rotational dynamic stability.

Although this work, by itself, does not lead to new recommendations for changes to the model rocket stability design guidelines that have been used successfully since Barrowman first proposed them[1], it does provide a more complete explanation for the behavior we observe every time we see a rocket launch, and that should be a part of our fundamental understanding of rocket dynamics. The practical application for this work is the design of vertical trajectory control systems where the rocket's rotational dynamics are needed to complete the control loop design.

The approach to this problem starts with a complete 2-dimensional flight model that describes both the rotational behavior as well as the flight trajectory of the rocket. After verifying the flight model matches the observed flight behavior, the model is used to determine which model parameters impact the rocket's rotational stability. A linearized dynamic stability model that includes the parameters necessary to predict the actual stability is then developed. Both the complete model and the linearized models are then used to analyze the rocket's rotational dynamic stability behavior. Finally, the models are verified using a detailed analysis of measured flight data from a rocket designed specifically for testing the model results.

1.2 Prior Work

This paper is an outgrowth of the work of Gordon K. Mandell presented in *A Unified Approach to Aerodynamic Stability*, a chapter from the book *Topics in Advanced Model Rocketry*[2]. In his work, Mandell describes the

---

[1] (Barrowman J. , 1968, p. 5)

[2] (Mandell, Caporaso, & Bengen, 1973).

dynamics of a rocket's rotation about its center of gravity in free flight using Euler's dynamic equations of motion. From this, the linearized second order differential equations describing the rotational dynamics of the rocket are developed, and the rotational stability is analyzed. Mandell mentions that there are side-to-side motions of the rocket that result from the angular rotation of the rocket, and that these side-to-side motions reduce the effective angle of attack[3], but he does not analyze this effect to determine its quantitative impact on the rotational stability. Mandell's work was originally published in a series of articles in Model Rocketry[4] magazine that was later reprinted as TR-201[5].

Mandell uses Barrowman's static stability equations[6] to determine the rotational forces on the rocket. Barrowman's work is based on NACA research on determining the stability of aerodynamically stabilized sounding rockets. Barrowman simplified the methods for the set of flight conditions that apply to model rockets. He developed a unified method for predicting the static stability of model rockets by calculating the aerodynamic center of pressure. This work was presented at NARAM 8[7] and published in *TIR-33 Calculating the Center of Pressure of a Model Rocket*[8], and *TIR-30 Stability of a Model Rocket in Flight*[9]. Barrowman also derived the rotational damping moment term that is used in the rotational dynamics equation[10].

Mandell also references Gurkin's NARAM 6 paper, Basic Missile Aerodynamic Stability,[11] as the first to look at model rocket dynamic stability, although the model presented is mostly qualitative.

In his NARAM 41 paper, A Design Procedure for Maximizing Altitude Performance[12], LaBudde presents a 3 degree of freedom model with coupling between the rotation and the X-axis motion. From that model, he derives equations for the natural frequency and damping ratio that are the same as the coupled natural frequency and damping ratio presented in this paper[13]. The focus of LaBudde's paper is altitude optimization and he does not take

---

[3] (Mandell, Caporaso, & Bengen, 1973, p. 101)

[4] (Mandell G. K., Fundamentals of Dynamic Stability, 1968-1969)

[5] (Mandell G. K., Fundamentals of Dynemic Stability, TR-201)

[6] (Barrowman J. S., The Practical Calculation of the Aerodynamic Characteristics of Slender Finned Vehicles, Master's Thesis, 1967)

[7] (Barrowman & Barrowman, The Theoretical Prediction of Center of Pressure, NARAM-8, 1966)

[8] (Barrowman J. , 1968)

[9] (Barrowman J. , 1970)

[10] (Barrowman J. S., The Practical Calculation of the Aerodynamic Characteristics of Slender Finned Vehicles, Master's Thesis, 1967, p. 40)

[11] (Gurkin, 1964)

[12] (LaBudde, 1999)

[13] See Appendix 5 - Coupled Damping Comparison to LaBudde's Model

the dynamic stability investigation any further into the motions of the rocket that lead to the enhanced rotational stability.

There are two other NARAM papers focused on rotational dynamic stability. In his NARAM 18 paper, Dynamic Stability Criteria for Model Rockets[14], Micci observes that the stability models do not accurately predict the stability of rocket with small fins. He developed an empirical method for designing stable rockets with small fins. Philips' NARAM 21 paper, A Study of Rotational Motions in Rocket Flight Dynamics[15], covers roll coupling due to spin. Neither of these papers talks about coupling between the rocket's rotation and it is lateral motion.

Some of the tools and models used in this paper are based on prior work done by the author to model and visualize a rocket's flight in 3-dimensional space. Those same tools were also used to visualize the measured flight data from an RAF Datalogger board. The modeling is done in Mathcad, and the flight and attitude visualization is written using the Visual Python library in Python. Examples of this work are available on the authors web site[16], but it otherwise has not been published to date.

The flight data analysis was originally done in an Excel spreadsheet that was described in a series of articles by the author in Sport Rocketry magazine[17].

1.3 Acknowledgements

I would like to thank Jim Barrowman for sending me a copy of his master's thesis back in 2000, long before it was made available on NASA's NTRS website, and finally make good on a promise I made to him at that time. In the e-mail request, I explained I was researching model rocket dynamic stability and that I would be sure to share with him any R&D report that resulted from the work. I doubt he is still expecting it 24 years later.

I would also like to thank Gordon Mandell, whose work inspired my interest in flight dynamics. After sending him a preliminary copy of the paper this R&D report is based upon, he brought to my attention Edward LaBudde's NARAM-41 R&D paper, *Design Procedure for Maximizing Altitude Performance.* I had searched through all the past NARAM R&D papers for those related to dynamic stability but had missed this one due to its title. LaBudde derives the same expression for the coupled damping coefficient using a different approach to the one presented in

[14] (Micci, 1976)

[15] (Philips, 1979)

[16] (Fetter T. , 2014-2016)

[17] (Fetter T. B., 2015)

this paper, so thanks to Gordon I did not miss crediting LaBudde for being the first to recognize the coupled damping ratio concept.

My special thanks goes to Kurt Gunther. Kurt had contacted me after an online PTC Mathcad users conference where I had talked about using Mathcad in model rocketry. He was interested in the Mathcad modeling I had been doing, so I sent him a preliminary version of the paper this R&D report is based upon. Kurt read the entire paper and sent me many pages of feedback that has been very helpful.

1.4 A Note About the Appendices

Normally, in a technical paper, the appendices are reserved for details, such proofs, algorithms, or code listings, provided for completeness, but that most readers would not be interested in. In this paper, the appendices 1-4 include background information on the mathematical tools, methods, and aerodynamical models used in this paper. The information is not part of the main contributions of this paper. The decision was made to include this background information, knowing that the reading audience has a wider range of backgrounds than is typical for most technical papers and to help make the paper more accessible to those readers. By moving this background information to the appendices, it helps keep the body focused on the actual contributions.

2 Rotational Dynamic Stability Model

2.1 The Rotational Dynamics Equation

The rotational dynamics equation describes the orientation of the rocket during its flight as well as the rocket's dynamic stability. The rotational dynamics equation from Section 7, leaving out the jet damping moment, which is shown to be small compared to the rotational damping, is

$$I_L \frac{d}{dt}\omega_y = M_{2y} + M_{1y} \tag{2.1-1}$$

Expanding M_{1y} and M_{2y} using equations (7.1-24) through (7.1-28)

$$M_{1y} = -F_{N1} \cdot (L_{CP} - L_{CG}) \tag{2.1-2}$$

$$M_{2y} = -F_{N2} \cdot (L_{CP} - L_{CG}) \tag{2.1-3}$$

$$F_{N1} = -\frac{\rho}{2} \cdot A_r \cdot C_{N\alpha} \cdot {v_T}^2 \cdot \alpha_{at} \tag{2.1-4}$$

$$F_{N2} = +\frac{\rho}{2} \cdot A_r \cdot C_{N\alpha} \cdot v_T \cdot \omega_r \cdot (L_{CP} - L_{CG}) \tag{2.1-5}$$

Equation (2.1-1) can then be written as[18]

$$I_L \cdot \frac{d^2}{dt^2}\alpha_y + C_2 \cdot \frac{d}{dt}\alpha_y = C_1 \cdot \alpha_{at} \tag{2.1-6}$$

where the forcing coefficient is[19]

$$C_1 = \frac{\rho}{2} \cdot {v_T}^2 \cdot A_r \cdot C_{N\alpha} \cdot (L_{CP} - L_{CG}) \tag{2.1-7}$$

and the damping coefficient is[20]

$$C_2 = \frac{\rho}{2} \cdot v_T \cdot A_r \cdot C_{N\alpha} \cdot (L_{CP} - L_{CG})^2 \tag{2.1-8}$$

---

[18] (Mandell, Caporaso, & Bengen, 1973, p. 88):

[19] (Mandell, Caporaso, & Bengen, 1973, p. 201):

[20] (Mandell, Caporaso, & Bengen, 1973, p. 202)

Equation (7.1-16) shows the angle of attack is

$$\alpha_{at} = \alpha_T - \alpha_y \tag{2.1-9}$$

where α_T which is the angle of the total oncoming airstream, θ_T, reflected into same quadrant as α_y. Then, equation (2.1-6) can then be written as

$$I_L \cdot \frac{d^2}{dt^2}\alpha_y + C_2 \cdot \frac{d}{dt}\alpha_y + C_1 \cdot \alpha_y = C_1 \cdot \alpha_T \tag{2.1-10}$$

Equation (2.1-10) is a second order differential equation that describes the rotation of the rocket, α_y, in response to the driving function, α_T. α_T is the input variable, and α_y is the output variable. If α_T changes due to changes in the wind or velocity of the rocket, then α_y follows with the dynamics described by the differential equation. If α_T is a step function, then α_y will eventually settle to value of α_T since both variables are multiplied by the same constant, C_1. The angle of attack, α_{at}, or the difference between α_T and α_y, tends to zero over time, as does the normal force, which is a function of α_{at}.

The time response of α_y is determined by solving the differential equation (2.1-10). To solve equation (2.1-10), the Laplace transform is used to transform the linear time domain differential equation into a linear algebraic frequency domain equation. The Laplace transform of equation (2.1-10) is

$$I_L \cdot s^2 \cdot \alpha_y + C_2 \cdot s \cdot \alpha_y + C_1 \cdot \alpha_y = C_1 \cdot \alpha_T \tag{2.1-11}$$

Regrouping the terms to ratio the output variable to the input variable creates a frequency gain function:

$$\frac{\alpha_y}{\alpha_T} = \frac{1}{\frac{I_L \cdot s^2}{C_1} + \frac{C_2}{C_1} \cdot s + 1} \tag{2.1-12}$$

The dynamics of a second order differential equation are described by two parameters, the natural frequency, ω_n, and the damping ratio, ζ. Written in terms of these two parameters, the second order equation is

$$\frac{\alpha_y}{\alpha_T} = \frac{1}{\frac{s^2}{\omega_n^{\,2}} + \frac{2 \cdot \zeta \cdot s}{\omega_n} + 1} \tag{2.1-13}$$

where:

$$\omega_n = \sqrt{\frac{C_1}{I_L}} \tag{2.1-14}$$

and

$$\zeta = \sqrt{\frac{C_2^{\,2}}{4 \cdot C_1 \cdot I_L}} \tag{2.1-15}$$

Solving for ω_n and ζ in terms of the rocket parameters by replacing C_1 and C_2 in equations (2.1-14) and (2.1-15) with equations (2.1-7) and (2.1-8) gives

$$\omega_n = v_T \cdot \sqrt{\frac{\rho \cdot A_r \cdot C_{N\alpha} \cdot (L_{CP} - L_{CG})}{2 \cdot I_L}} \tag{2.1-16}$$

$$\zeta = \sqrt{\frac{\rho \cdot A_r \cdot C_{N\alpha} \cdot (L_{CP} - L_{CG})^3}{8 \cdot I_L}} \tag{2.1-17}$$

The natural frequency, ω_n, is a function of velocity, but the damping constant, ζ, is constant with velocity.

The second-order time domain equation (2.1-10), rewritten in terms of the natural frequency and damping ratio coefficients, is

$$\frac{1}{\omega_n^{\,2}} \cdot \frac{d^2 \alpha_y}{dt^2} + \frac{2 \cdot \zeta}{\omega_n} \cdot \frac{d \alpha_y}{dt} + \alpha_y = \alpha_T \tag{2.1-18}$$

The next sections will focus on the solution of the rotational dynamics equation using the parameters for the test rocket TR-1. The physical parameters for TR-1 are given in Section 3.1.

2.2 Rotational Stability

The dynamic stability of a rocket is a measure of its rotational response to perturbations as it moves along its flight path. The perturbations can be due to a change in the angle of the incident airstream, a change in the angle the thrust of the motor, or a change in a control surface of the airframe such as the angle of a canard or fin tab. The perturbations used here to examine stability are changes in the angle of the incident airstream, α_T .

When a rocket leaves the launch guide, it will see a step in lateral force due to the wind. That step in the wind velocity, which is a part of the total airstream velocity, creates a step in the angle of the oncoming airstream that is the input, α_T , to the rotational equation. The rocket responds to this perturbation in α_T by rotating into the direction of the wind, to align its rotational angle, α_y , with α_T . The response of α_y is governed by the dynamics of the rotational equation (2.1-18). This is called a step response. Three parameters describe the step response. The magnitude of the step, α_T determines the magnitude of the step response. The natural frequency, ω_n , describes the rate of the step response and the frequency of the oscillations in the step response. The larger ω_n , the faster the rocket responds to the wind perturbation. The damping ratio, ζ , describes the amount of overshoot and the decay time of the ringing in the step response. The damping ratio describes the stability of the rotational system. The smaller the damping ratio, the larger the step response overshoot and the longer the ringing, and the less stable the system. For an unstable system, the step response increases exponentially without bound.

Normally, the input step used to characterize a system response is a constant magnitude step. But in the rotational system input, α_T will continue to change after the initial step due to the wind as rocket accelerates and the velocity of the oncoming airstream increases relative to the velocity of the lateral wind. The complete flight model takes into account the initial step in α_T due to the wind, as well as the continued change in α_T as the rocket accelerates along the X and Z-axes due to the thrust of the motor and the acceleration due to gravity. But the complete model can only be solved numerically as it is a series of nonlinear differential equations. By making the assumption that the rocket is traveling at a fixed velocity and the perturbation in α_T is small, the rotational response of the rocket can be determined by a linearized version of rotational equation (2.1-18). The linearized equation can be solved in closed form and has the natural frequency, ω_n , and damping ratio, ζ , parameters that describe the rotational stability of the rocket. Mandell's stability analysis for model rockets[21] is based on a detailed analysis of this dynamic stability equation.

[21] (Mandell, Caporaso, & Bengen, 1973, pp. 55-259)

From equation (7.1-16), making the assumption that the rocket is flying straight up at the time of the perturbation so that $v_X = 0$

$$\alpha_T = -\arcsin\frac{v_w - v_X}{v_T} \simeq \left.\frac{v_w - v_X}{v_T}\right|_{v_X=0} = \frac{v_w}{v_T} \tag{2.2-1}$$

Using the parameters from test rocket TR-1 (see Section 3 for model parameters) and assuming a fixed velocity of 110 mph, then the natural frequency, $\omega_n = 1.05Hz$, and the damping ratio, $\zeta = .0095$. Figure 2-1 shows the step response to a 10 mph cross wind where the magnitude of the input step in the direction of the oncoming airstream is

$$\alpha_T = \frac{v_w}{v_T} = -\frac{-10mph}{110mph} = 5.2\,\text{deg}$$

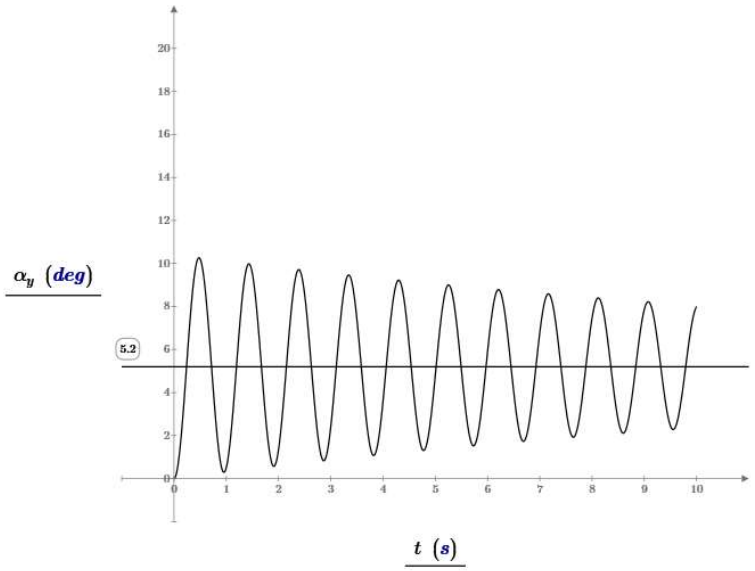

Figure 2-1 Second order model rotation step response for ω_n = 1.05 Hz and ζ = 0.0095

This would indicate that the rocket's oscillations start at an amplitude of ± 10 degrees and continue for many cycles, with the oscillation amplitude decaying very slowly. In the actual flight, the frequency of the oscillation, ω_n , would change as the rocket's velocity changes, but the damping ratio remains constant with velocity. A rocket that oscillates like this is not very stable, which is expected if the damping ratio is only 0.0095. But this is surprising for a rocket with the center of gravity 2.4 calipers, or body diameters, ahead of the center of pressure, as most rockets with this stability margin do not exhibit this much rotational oscillation.

A full simulation of test rocket TR-1, using the Mathcad numerical solution of the complete model from Section 7, shows that the rocket indeed is much more stable than rotational dynamics equation alone predicts, as shown in Figure 2-2. The oscillations decay after only a few cycles, which is closer to the observed behavior of most model rockets.

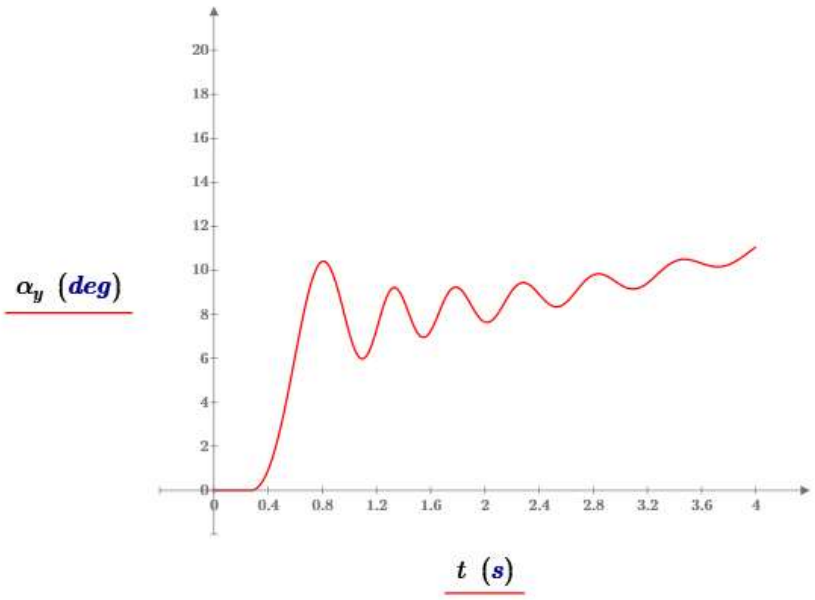

Figure 2-2 Rotation of Test Rocket 1 from a full simulation due to a 10 mph step in wind speed as the rocket leaves the launch guide

The difference between the full simulation and the response predicted by the rotational equation (2.1-18) alone, with a fixed step in α_T, must be due to something else in the model that modifies the behavior of the rotational equation, so that the rotational equation by itself does not describe the rotational dynamic stability of the rocket. An interaction between the differential equations in the complete model must have the effect of increasing the rotational damping, and thus the dynamic stability of the rocket.

If there is a cross-coupling of terms between the rotational equation and the trajectory equations, then it must be through one or more of the forces that make up the equations. To determine which of the trajectory forces have an impact on the rotation, each of the forces can individually be set to zero in the model, and the result compared to the complete model. Doing this, it was found that setting F_{DX}, F_{DZ}, F_{LZ}, and $m_o \cdot g$ to zero in equations (7.1-4) to (7.1-9), leaving just the X-axis lift force, F_{LX}, and thrust forces F_{TX} and F_{TZ}, had minimal impact on the model's prediction of the rockets rotational stability. Setting those forces to zero in equations (7.1-4) to (7.1-9), the model equations reduce to

$$\frac{d}{dt}d_X = v_X \tag{2.2-2}$$

$$m_o \frac{d}{dt}v_X = F_{TX} + F_{LX} \tag{2.2-3}$$

$$\frac{d}{dt}d_Z = v_Z \tag{2.2-4}$$

$$m_o \frac{d}{dt}v_Z = F_{TZ} \tag{2.2-5}$$

$$\frac{d}{dt}\alpha_y = \omega_y \tag{2.2-6}$$

$$I_L \frac{d}{dt}\omega_y = M_{2y} + M_{1y} \tag{2.2-7}$$

The resulting simulation based on this simplified model is shown in Figure 2-3 compared to the full simulation. The α_y trace (red) is the result of the full simulation, which is the same as in Figure 2-2. The α_{y2} trace (blue) is the result of the simplified of equations above. Since the thrust force is an input to the system and is constant for the duration of the motor burn, it must be the X-axis lift force that provides coupling from the X-axis equation of motion to the rotational equation and that plays a role in the damping of the rotational response of the rocket. The drag terms and Z-axis lift force have little effect on the damping or oscillation frequency. Removing the gravity force does impact the final value of the rotational angle but does not impact the system damping.

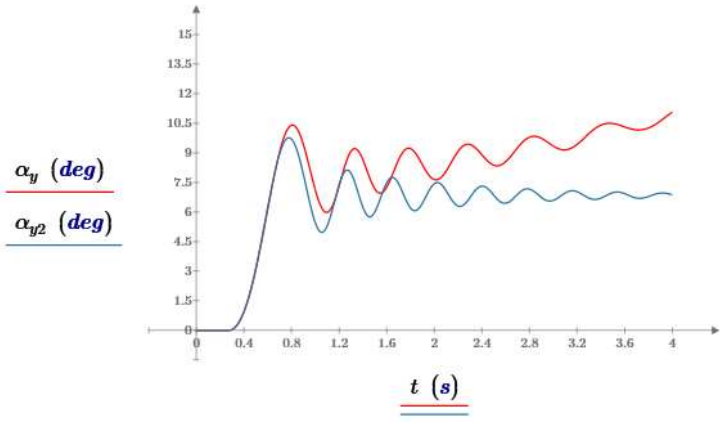

Figure 2-3 A comparison of the complete model (red trace) and the simplified model (blue trace) with F_{DX}, F_{DZ}, F_{LX}, and $m_o \cdot g$ set to zero for TR-1

Narrowing the cause of the coupling down to the X-axis lifting force, F_{LX} , begins to provide some insight into the mechanism that enhances the stability of the rocket. Since F_{LX} drives the motion of the rocket along the X-axis, the stability must be due to that motion, and v_X is the likely state variable providing the coupling.

Figure 2-4 shows the driving function for the rotational equation, α_T , from the full simulation for test rocket TR-1. If there were no cross coupling between the equations, and driving function was just a function of v_w, α_T would be a simple step function as the rocket leaves the launch guide and the step response solution of the rotational equation alone would determine the rotational response and stability of the rocket. But due to the cross coupling, the driving function changes with time and has a sinusoidal component. Figure 2-4 shows that the sinusoidal component of α_T is 90 degrees out of phase with the rotation angle α_y . The damping in a second order differential equation comes from the first order term, which is 90 degrees out of phase with the zero order term, so the phase of the sinusoidal oscillation on the input to the rotational equation, α_T , indicates that sinusoidal component is providing the enhanced damping to the overall system.

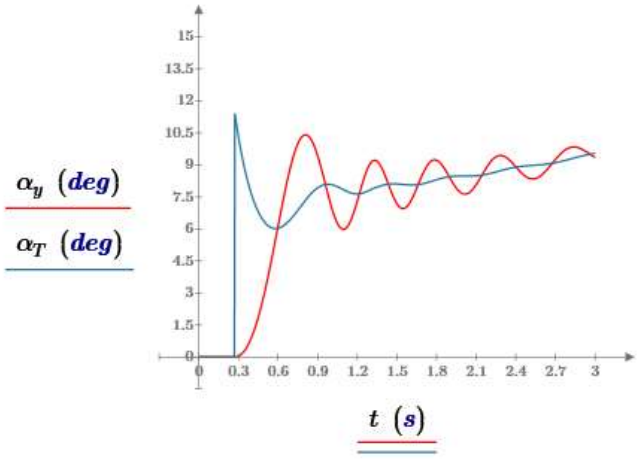

Figure 2-4 Driving function, α_T , and rotational output, α_y , of TR-1 simulation for TR-1

From equation (7.1-16) , where $v_w \ll v_T$ and $v_X \ll v_T$

$$\alpha_T = -\arcsin\left(\frac{v_w - v_X}{v_T}\right) \simeq \frac{v_X}{v_T} - \frac{v_w}{v_T} \tag{2.2-8}$$

α_T is a function of v_X/v_T and v_w/v_T . Figure 2-5 shows the two component parts of α_T from the complete model for TR-1. The wind velocity, v_w is an input to the model, and the v_w/v_T term has no sinusoidal component, so the

X-axis velocity, v_X , is the term that provides the cross coupling with X-axis equation of motion that leads to the increased rotational stability of the overall system.

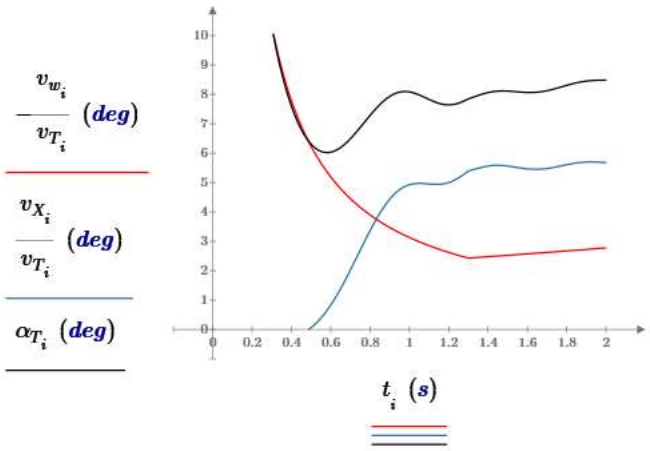

Figure 2-5 The component parts of α_T

2.3 X-Axis Motion of the Rocket

Figure 2-6 shows a plot of the flight trajectory of test rocket TR-1 along the X and Z-axis ground frame of reference with a 10 mph wind blowing in the -X direction (left to right). As the rocket leaves the launch guide, the rocket rotates into the direction of the oncoming wind. Once the rocket has rotated, there is a component of the thrust force aligned with the X-axis, and the rocket accelerates along the X-axis, as shown in Figure 2-7. The small sinusoidal component of v_X can be seen, especially after motor burn-out where the rocket is decelerating slowly due to drag. The sinusoidal component of v_X due to the lift force is small compared to the much larger velocity due to the thrust force, but the small sinusoidal motion is still visible.

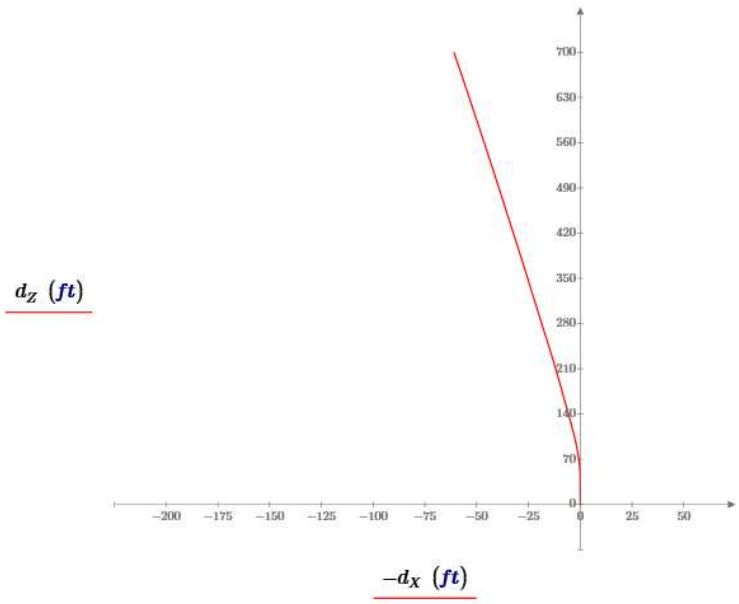

Figure 2-6 Ground-based frame of reference trajectory of test rocket TR-1 (note the positive x is on the left side of the graph – the double negative is required so larger values are to the right)

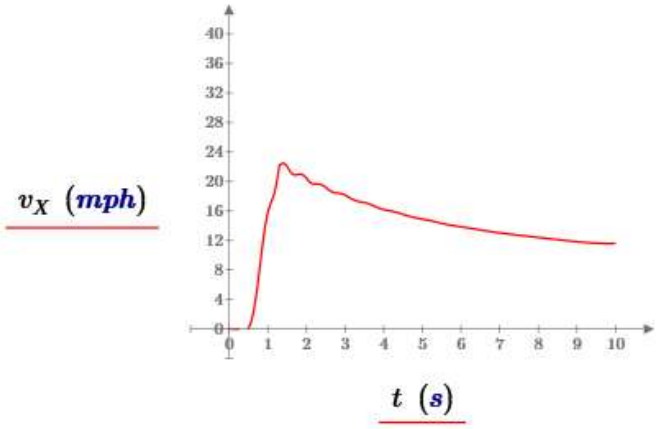

Figure 2-7 X-axis velocity of test rocket TR-1

The small sinusoidal velocity rides on top of a much larger velocity trend as shown in Figure 2-7. To get just the small sinusoidal component of v_X, the X-axis equation of motion, equation (7.1-5) can be solved with the thrust and drag forces set to zero, leaving just the lift force.

$$m_o \frac{dv_{X\,ss}}{dt} = F_{LX} = \frac{\rho}{2} \cdot A_r \cdot C_{L\alpha} \cdot \alpha_{at} \cdot {v_T}^2 \cdot \cos\theta_T \tag{2.3-1}$$

This is a nonlinear equation because the lift force is a function of the total airstream velocity squared. The lift force that creates the small sinusoidal motion in v_X must be calculated using the larger velocity. To do this, equation (2.3-1) is solved simultaneously along with the other equations of the complete flight model, equations (7.1-4) to (7.1-9), including the full equation for the X-axis motion. The values for the state variables v_X, v_Z, and α_y from the complete model are then used to solve equation (2.3-1) for the small sinusoidal component, v_{Xss}, where both v_T and θ_T are functions of those state variables. Figure 2-8 shows the result value of the small sinusoidal X-axis velocity due to the lift force from equation (2.3-1).

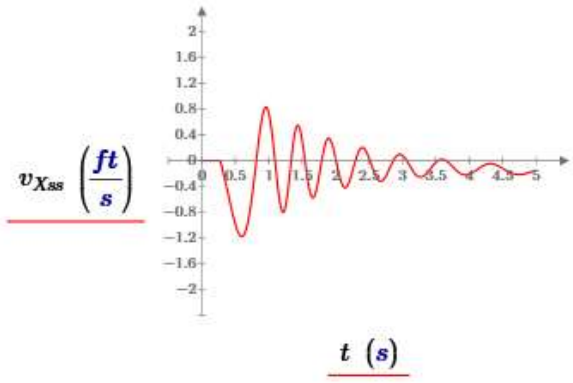

Figure 2-8 Sinusoidal portion of X-axis velocity, v_X

Next, the rotational dynamics equation can be written in terms of v_X. Starting with the rotational dynamics equation (2.1-10)

$$I_L \cdot \frac{d^2}{dt^2}\alpha_y + C_2 \cdot \frac{d}{dt}\alpha_y + C_1 \cdot \alpha_y = C_1 \cdot \alpha_T$$

and substituting the expression for α_T in terms of v_X from equation (7.1-16)

$$\alpha_T = -\arcsin\left(\frac{v_w - v_X}{v_T}\right) \simeq \frac{v_X}{v_T} - \frac{v_w}{v_T}$$

results in

$$I_L \cdot \frac{d^2}{dt^2}\alpha_y + C_2 \cdot \frac{d}{dt}\alpha_y + C_1 \cdot \alpha_y = C_1 \cdot \frac{v_X}{v_T} - C_1 \cdot \frac{v_w}{v_T} \tag{2.3-2}$$

If the sinusoidal portion of v_X is contributing to the overall rotational damping, then v_X must be in phase with the first order damping term. To show the relative phasing, the rotation rate $d\alpha_y / dt = \omega_y$, can be projected onto the X-axis to get a tangential rotational velocity. The tangential velocity will depend upon the distance from the center of gravity to the projection point. Since this is being done to compare just the phase of the X-axis side-to-side velocity to the rotational velocity, the distance used is not critical. The center of pressure will be chosen as the reference point. Figure 2-9 shows the relationship between the rocket's rotation rate about the y-axis and the rotational velocity at the center of pressure projected onto the X-axis. A positive rotation about the rocket's y-axis, which is projecting out of the page, is counterclockwise, and maps to a negative excursion along the X-axis, with the positive X-axis to the left.

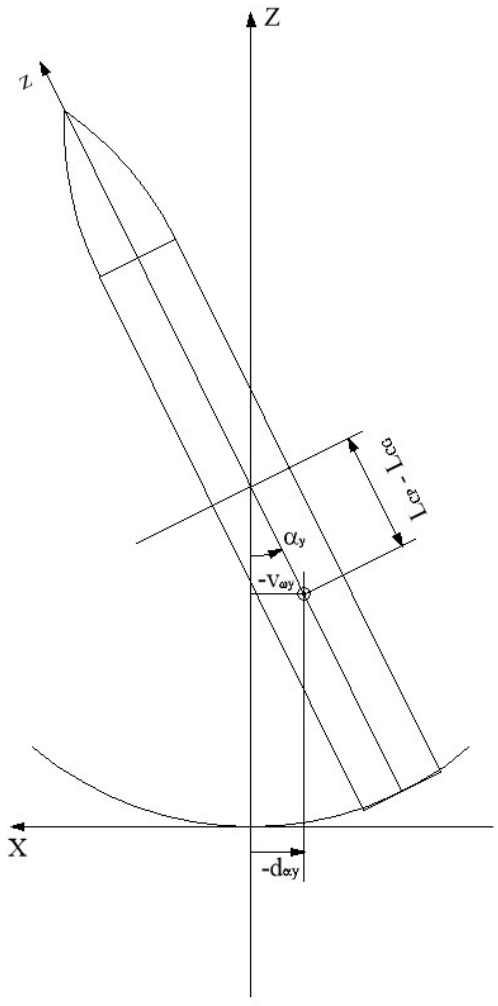

Figure 2-9 Rotational motion and tangential velocity of the rocket in the X-Z axis frame

The tangential velocity of the center of pressure for small angular rotation rates about the center of gravity is given by

$$v_{\omega y} = -\left(L_{CP} - L_{CG}\right) \cdot \sin(\omega_y) \simeq -\left(L_{CP} - L_{CG}\right) \cdot \omega_y \tag{2.3-3}$$

Rearranging equation (2.3-3) to express the angular rotation rate in terms of the linear X-axis velocity of the rocket at the center of pressure

$$\omega_y \simeq -\frac{v_{\omega y}}{L_{CP} - L_{CG}} \tag{2.3-4}$$

Figure 2-10 shows the velocity of the X-axis side-to-side velocity of the center of gravity of the rocket, v_{Xss}, and the tangential velocity of the center of pressure of the rocket due to the angular rotation rate of the rocket, $v_{\omega y}$, projected onto the X-axis for TR-1. The negative values of $v_{\omega y}$ and v_{Xss} are used so that both linear velocities are in phase with the first order damping term in the rotational dynamics equation that is proportional to ω_y. This shows the side-to-side velocity is in phase with the rotational velocity when they both have the same signs, so they would add constructively. It also shows the velocity due to the side-to-side motion is about 4 times larger in magnitude than the tangential velocity due to the rocket's rotation for test rocket TR-1 when the center of pressure is used as the reference point for translating the rotation of velocity to a tangential velocity.

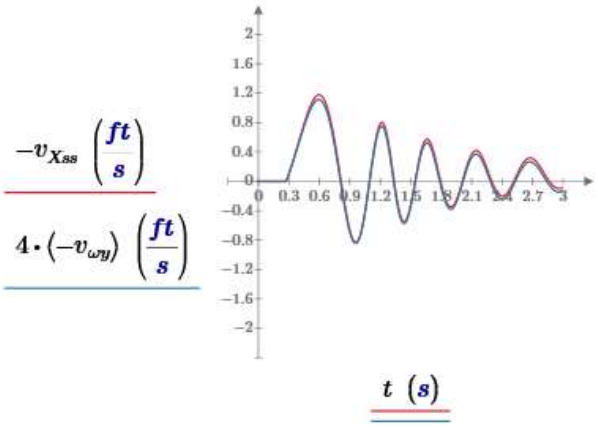

Figure 2-10 A comparison of the velocity of the X-axis side-to-side velocity, v_{Xss}, and the velocity of the rocket base along the X-axis due to the angular rotation rate of the rocket, ω_n

Knowing that the X-axis side-to-side velocity is in phase with the tangential rotational velocity, both of those terms can be grouped together in the rotational equation. Replacing $d\alpha_y/dt$ in equation (2.3-2) with equation (2.3-4), adding $-(C_1/v_T)\cdot v_{Xss}$ to both sides of the equation, and grouping the velocity terms, shows the two components of the damping term

$$I_L \cdot \frac{d^2}{dt^2}\alpha_y + \left(-\frac{C_2}{L_{CP}-L_{CG}} \cdot v_{\omega y} - \frac{C_1}{v_T} \cdot v_{Xss} \right) + C_1 \cdot \alpha_y = C_1 \cdot \frac{(v_X - v_{Xss})}{v_T} - C_1 \cdot \frac{v_w}{v_T} \tag{2.3-5}$$

The $(v_X - v_{Xss})$ term on the right-hand side of the equation is the X-axis velocity minus the small sinusoidal velocity and represents the part of the driving function that is due to the X-axis velocity of the rocket after it rotates away from vertical due to just the thrust force.

Substituting the expressions for C_1 and C_2 into the terms that multiply $v_{\omega y}$ and v_{Xss} in equation (2.3-5)

$$\frac{C_1}{v_T} = \frac{\frac{\rho}{2} \cdot A_r \cdot C_{N\alpha} \cdot {v_T}^2 \cdot (L_{CP}-L_{CG})}{v_T} = \frac{\rho}{2} \cdot A_r \cdot C_{N\alpha} \cdot v_T \cdot (L_{CP}-L_{CG})$$

and

$$\frac{C_2}{L_{CP}-L_{CG}} = \frac{\frac{\rho}{2} \cdot A_r \cdot C_{N\alpha} \cdot v_T \cdot (L_{CP}-L_{CG})^2}{L_{CP}-L_{CG}} = \frac{\rho}{2} \cdot A_r \cdot C_{N\alpha} \cdot v_T \cdot (L_{CP}-L_{CG})$$

Therefore

$$\frac{C_1}{v_T} = \frac{C_2}{L_{CP}-L_{CG}}$$

so each of the terms multiplying the velocities in the damping term of equation (2.3-5) are equal.

Creating a new rotational velocity damping coefficient

$$C_4 = \frac{\rho}{2} \cdot A_r \cdot C_{N\alpha} \cdot v_T \cdot (L_{CP}-L_{CG}) \tag{2.3-6}$$

equation (2.3-5) becomes

$$I_L \cdot \frac{d^2}{dt^2}\alpha_y + C_4\left(-v_{\omega y} - v_{Xss}\right) + C_1 \cdot \alpha_y = -C_{\cdot 1}\frac{v_w}{v_T} + C_{\cdot 1}\frac{\left(v_X - v_{Xss}\right)}{v_T} \tag{2.3-7}$$

The tangential velocity due to the rocket's rotation at the center of pressure and the side-to-side velocity of the rocket due the coupling between the rotational equation and the X-axis equation of motion have the same gain in the damping moment. Had a different reference point been used for translating the rotational velocity to tangential velocity, the gain and amplitude would have scaled inversely, but the product, and therefore the total rotational damping, would have remained constant. The gains being equal when the center of pressure is used as a reference point is an interesting result. It says that equal side-to-side velocities of the entire rocket and tangential rotational velocities at the center of pressure have the same effect on the rotational damping.

Figure 2-11 shows that the damping term in the rotational equation comes from an induced angle of attack, $\alpha_{\omega y}$, caused by the vector sum of the total income airstream velocity vector, v_T, and the tangential rotational velocity vector, $v_{\omega y}$. This induced angle of attack creates a normal force that pushes back on the rocket opposite the direction it is rotating, providing the rotational damping moment. The side-to-side velocity adds to the tangential rotational velocity in phase, increasing the induced angle of attack, for a total angle of attack, $\alpha_{\omega y+Xss}$, that provides the enhanced damping to the overall system.

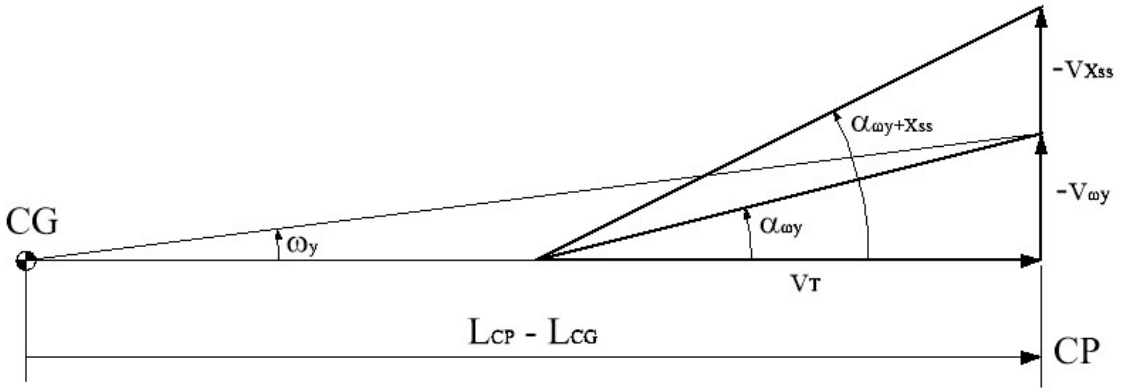

Figure 2-11 Determining the total damping velocity from $v_{\omega y}$ and $v_{X ss}$

The coupled damping moment is a simple modification of Barrowman's damping moment equation[22] with the addition of $v_{X ss}$

[22] (Barrowman J. S., The Practical Calculation of the Aerodynamic Characteristics of Slender Finned Vehicles, Master's Thesis, 1967)

$$M_2' = -C_{N\alpha} \cdot A_r \cdot \frac{\rho}{2} \cdot v_T \cdot \left(L_{CP} - L_{CG}\right) \cdot \left(v_{\omega y} + v_{X\,ss}\right) \tag{2.3-8}$$

Figure 2-10 shows the X-axis side-to-side velocity is 4 times the tangential rotational velocity for test rocket TR-1. The sum of the two is 5 times the tangential rotational velocity alone.

The distance the rocket moves due to the rotational and side-to-side motion is calculated from the rotational angle, α_y

$$d_{\alpha y} = -\left(L_{CP} - L_{CG}\right) \cdot \sin(\alpha_y) \simeq -\left(L_{CP} - L_{CG}\right) \cdot \alpha_y \tag{2.3-9}$$

Figure 2-12 shows the plot of the side-to-side distance, d_{Xss}, and the distance the center of pressure of the rocket moves due to its rotation about its center of gravity, $d_{\alpha y}$, projected onto the X-axis for test rocket TR-1. Like the velocities, the distances are aligned in phase, with the distance traveled due to the side-to-side motion being 4 times larger than the tangential distance traveled at the center of pressure due to its rotation. The side-to-side distance traveled is less than 2 inches, and the rotational distance the center of pressure moves is less than 0.5 inches. The tail and nose of the rocket both move further, due to the rocket's rotation, than the center of pressure, since they are further from the center of gravity, so the overall rotation of the rocket is more noticeable. In the case of TR-1, the nose swings about 2 inches, which is the same as the side-to-side motion of the rocket.

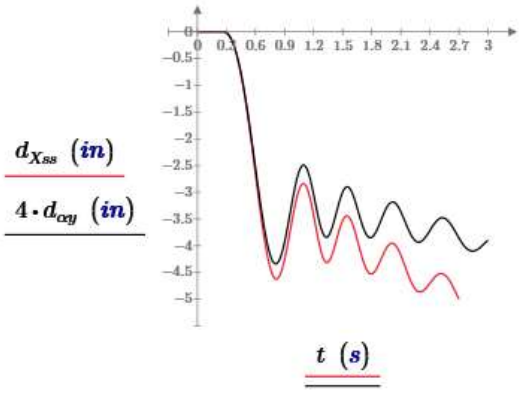

Figure 2-12 A comparison of the X-axis side-to-side distance, d_{Xss}, and the angular displacement of the rocket center of pressure, $d_{\alpha y}$, along the X-axis

Figure 2-13 shows the same trajectory of test rocket TR-1 as shown in Figure 2-6 in the red trace, and with an 80 x exaggerated version of the sinusoidal X-axis motion superimposed on the trajectory in the blue trace. This shows where along its vertical trajectory the rocket moves side-to-side.

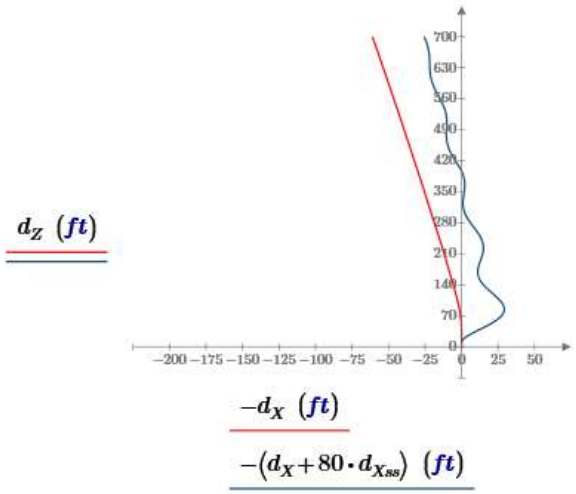

Figure 2-13 Rocket trajectory with 80 x exaggerated X-axis motion

Figure 2-14 shows a plot of the small sinusoidal X-axis side-to-side displacement versus the Z-axis altitude. The series of vectors shows the rotation angle of the rocket along its flight path. The X-axis scale is 1000 times the Z-axis scale, and the rotation angle, α_y, has been scaled by a factor 10 larger, both to show motion of the rocket of the rocket more clearly. This plot shows that the center of gravity of the rocket moves in phase with the rotational displacement of the center of pressure of the rocket. As the rocket is sliding to the right, the center of pressure (and tail of the rocket) are rotating to the right. And as the rocket is sliding to the left, the center of pressure is rotating to the left. If the displacements are in phase, then the velocities are also in phase.

Figure 2-14 shows the cause of the side-to-side motion of the rocket. The rotation of the rocket creates an angle of attack resulting in an X-axis lift force that causes the rocket to move sideways along the X-axis. To the left of the center line of the sinusoid, the X-axis lift force is negative, and to the right of the vertical center line, the lift force is positive. As the rocket reaches its maximum X-axis velocity, the angle of attack of the rocket passes through zero, causing the lift force to reverse direction, which causes the rocket's X-axis velocity to slow down, turn around, and then increase in the opposite direction. Because the rocket's motion is not constrained in flight, the center of gravity is free to move side-to-side sinusoidally in response to the lift force due to the rocket's rotational angle. The X-axis side-to-side motion continues after motor burnout because the motion is due to the lift force and not the thrust force, so the enhanced damping also continues after motor burnout.

The rotational damping is a function of the X-axis velocity due to both the side-to-side motion and the rotational motion of the center of pressure. Both velocities are positive as the rocket is moving in the positive X direction, and both are negative as the rocket is moving in the negative X direction.

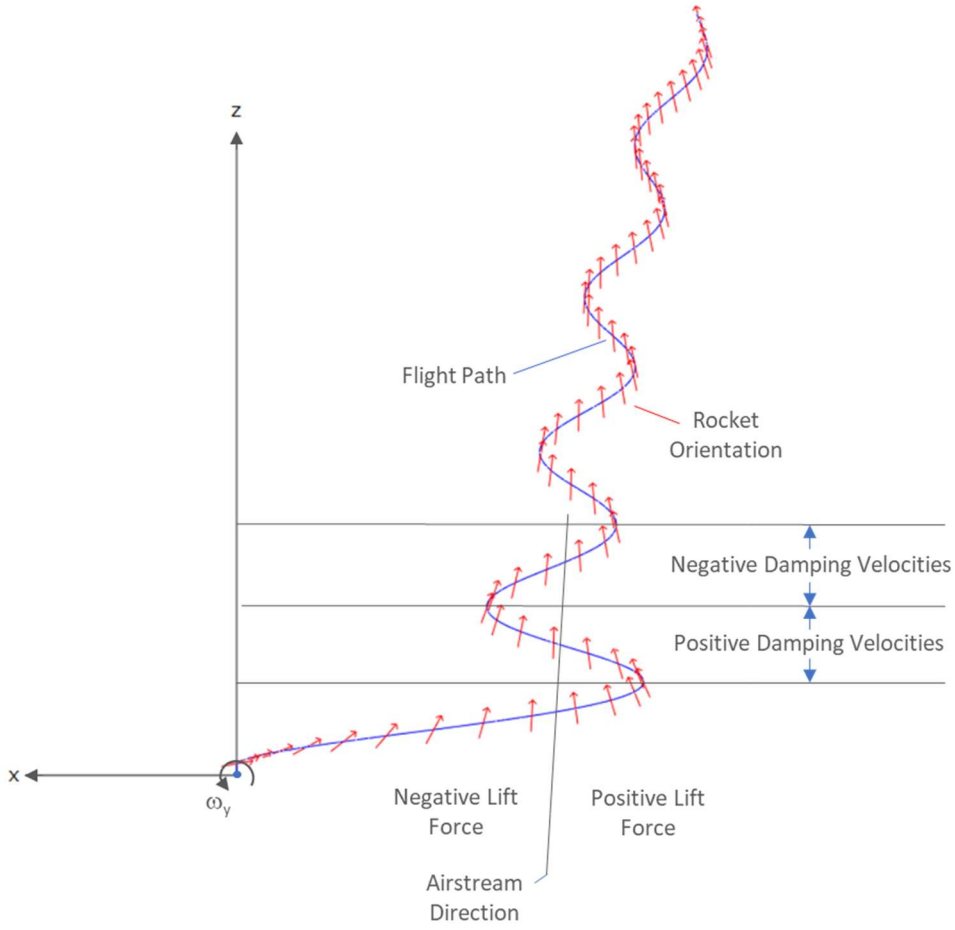

Figure 2-14 – Exaggerated X-Z frame motion and rocket angle: $X = 1000 \cdot Z$ and arrow rotation $= 10 \cdot \alpha_y$

(from a Python visualization of Mathcad data)

2.4 Linearized Coupled Rotational Dynamics Equation

The previous sections covered the mechanism of the enhanced rotational stability. This section will quantify the enhanced stability by deriving a single second order linearized rotational dynamics equation that includes the effects of the X-axis motion of the rocket on the damping. The previous sections showed that, for test rocket TR-1, the side-to-side velocity is 4 times the tangential rotational velocity at the center of pressure, and that both velocities are multiplied by the same damping coefficient to determine the total damping moment. But it did not quantify the

magnitude of the X-axis velocity, v_X, in terms of α_y. A single rotational dynamics equation just in terms of α_y is required to quantify the magnitude of the side-to-side motion in the damping moment.

Once again, the complete set of differential equations (7.1-4) to (7.1-9) that describe the rocket's position and rotation are

$$\frac{d}{dt} d_X = v_X \tag{2.4-1}$$

$$m_o \frac{d}{dt} v_X = F_{TX} + F_{DX} + F_{LX} \tag{2.4-2}$$

$$\frac{d}{dt} d_Z = v_Z \tag{2.4-3}$$

$$m_o \frac{d}{dt} v_Z = F_{TZ} + F_{DZ} + F_{LZ} - m_o g \tag{2.4-4}$$

$$\frac{d}{dt} \alpha_y = \omega_y \tag{2.4-5}$$

$$I_L \frac{d}{dt} \omega_y = M_{2y} + M_{1y} \tag{2.4-6}$$

First, these equations can be simplified as described in Section 2.2. The F_{DX}, F_{DZ}, F_{LZ}, and $m_o \cdot g$ terms do not have a significant impact on the rotational dynamics, as shown in Figure 2-3, so those terms can be left out.

The rocket velocity due to the thrust of the motor comes from the thrust force terms in the X and Z-axes equations of motion. For a constant thrust, both the v_Z and v_X increase as a nearly linear ramp (linear if there is no drag) until motor burn-out as shown in Figure 2-15. For a near vertical flight, the total airstream velocity is close to the upward Z-axis velocity, so $v_T \simeq v_Z$.

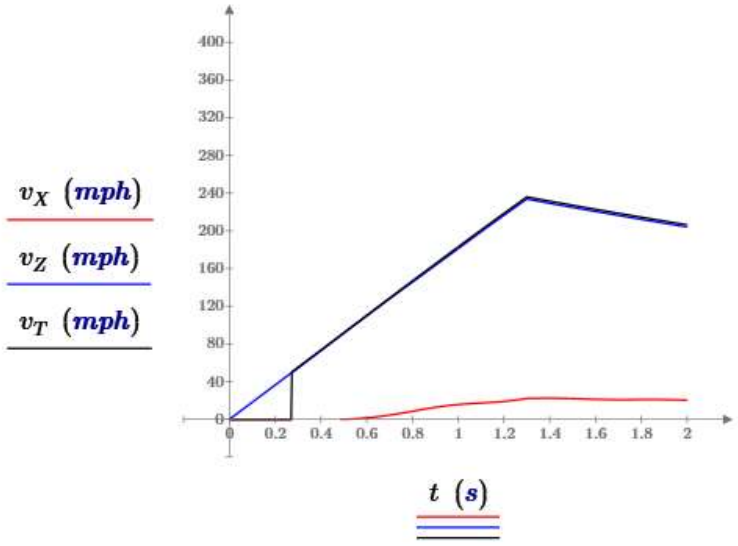

Figure 2-15 Velocity ramp in X and Z axes due to constant thrust, and the resulting total airstream velocity for the full model with all terms

Since the drag, lift, and forcing moment are all a function of v_T, which is a function of time, the system is non-linear when solving for α_y. To linearize the model so that it can be solved in closed form, a constant value for v_T must be assumed. If v_T is constant, then the thrust force terms F_{TX} and F_{TZ} must be zero. Because a fixed value of v_T is being used, the equations will only be valid for small, or incremental changes in velocity about that operating point velocity.

Assuming the thrust forces are zero, the differential equations of motion now reduce to

$$\frac{d}{dt} d_X = v_X \tag{2.4-7}$$

$$m_o \frac{d}{dt} v_X = F_{LX} \tag{2.4-8}$$

$$\frac{d}{dt} \alpha_y = \omega_y \tag{2.4-9}$$

$$I_L \frac{d}{dt} \omega_y = M_{2y} + M_{1y} \tag{2.4-10}$$

Equations (2.4-7) through (2.4-10) can be written in terms of the state variables d_X, v_X, d_Z, v_Z, α_y, and ω_y. Starting with the equation for X-axis lift, equation (7.1-20),

$$F_{LX} = \frac{\rho}{2} \cdot A_r \cdot C_{L\alpha} \cdot \alpha_{at} \cdot {v_T}^2 \cdot \cos\theta_T$$

For small angles of attack

$$C_L \simeq C_N$$

and then defining

$$C_3 = \frac{\rho}{2} \cdot A_r \cdot C_{N\alpha} \cdot {v_T}^2 \tag{2.4-11}$$

Since C_3 is a function of the total airstream velocity, v_T, C_3 must be determined for a fixed operating point value of v_T. Then

$$F_{LX} = C_3 \cdot \alpha_{at} \cdot \cos\theta_T$$

For $\theta_T \simeq \pi$, $\cos(\theta_T) \simeq -1$, and

$$F_{LX} = -C_3 \cdot \alpha_{at}$$

From equation (7.1-17),

$$\alpha_{at} = \alpha_T - \alpha_y$$

then

$$F_{LX} = -C_3 \cdot (\alpha_T - \alpha_y)$$

From equation (2.2-8), for small α_T

$$\alpha_T = -\arcsin\left(\frac{v_w - v_X}{v_T}\right) \simeq -\frac{v_w - v_X}{v_T}$$

then

$$F_{LX} = C_3 \cdot \frac{v_w}{v_T} - C_3 \cdot \frac{v_X}{v_T} + C_3 \cdot \alpha_y$$

Then the X-axis equation of motion, equation (2.4-8) , in terms of the state variables, becomes

$$m_o \frac{d}{dt} v_X + \frac{C_3}{v_T} \cdot v_X = C_3 \cdot \frac{v_w}{v_T} + C_3 \cdot \alpha_y$$

For the rotational equation, starting with equation (2.1-10)

$$I_L \cdot \frac{d^2}{dt^2} \alpha_y + C_2 \cdot \frac{d}{dt} \alpha_y + C_1 \cdot \alpha_y = C_1 \cdot \alpha_T$$

and substituting for α_T , the state variable form of the rotational equation is,

$$I_L \cdot \frac{d^2}{dt^2} \alpha_y + C_2 \cdot \frac{d}{dt} \alpha_y + C_1 \cdot \alpha_y = -C_1 \cdot \frac{v_w}{v_T} + C_1 \cdot \frac{v_X}{v_T}$$

Summarizing the system of linearized equations in terms of the state variables d_X , v_X , α_y , ω_y , and constant v_T

$$\frac{d}{dt} d_X = v_X \tag{2.4-12}$$

$$m_o \frac{d}{dt} v_X + \frac{C_3}{v_T} \cdot v_X = C_3 \cdot \frac{v_w}{v_T} + C_3 \cdot \alpha_y \tag{2.4-13}$$

$$\frac{d}{dt} \alpha_y = \omega_y \tag{2.4-14}$$

$$I_L \cdot \frac{d^2}{dt^2} \alpha_y + C_2 \cdot \frac{d}{dt} \alpha_y + C_1 \cdot \alpha_y = -C_1 \cdot \frac{v_w}{v_T} + C_1 \cdot \frac{v_X}{v_T} \tag{2.4-15}$$

Where, from equations (2.1-7) , (2.1-8), and, (2.4-11)

$$C_1 = \frac{\rho}{2} \cdot A_r \cdot C_{N\alpha} \cdot {v_T}^2 \cdot (L_{CP} - L_{CG}) \tag{2.4-16}$$

$$C_2 = \frac{\rho}{2} \cdot A_r \cdot C_{N\alpha} \cdot v_T \cdot (L_{CP} - L_{CG})^2 \tag{2.4-17}$$

$$C_3 = \frac{\rho}{2} \cdot A_r \cdot C_{N\alpha} \cdot {v_T}^2 \tag{2.4-18}$$

The state variables α_y and v_X now appear in both equation (2.4-13) and equation (2.4-15), so the X-axis trajectory equation is coupled to the rotational dynamics equation.

The Laplace transform can be applied to the linearized equations (2.4-12) to (2.4-15) to convert them from time domain differential equations to the frequency domain algebraic equations

$$s \cdot d_X = v_X \tag{2.4-19}$$

$$m_o \cdot s \cdot v_X + \frac{C_3}{v_T} \cdot v_X = C_3 \cdot \frac{v_w}{v_T} + C_3 \cdot \alpha_y \tag{2.4-20}$$

$$s \cdot \alpha_y = \omega_y \tag{2.4-21}$$

$$I_L \cdot s^2 \cdot \alpha_y + C_2 \cdot s \cdot \alpha_y + C_1 \cdot \alpha_y = -C_1 \cdot \frac{v_w}{v_T} + C_1 \cdot \frac{v_X}{v_T} \tag{2.4-22}$$

Solving equation (2.4-20) for v_X in terms of α_y

$$v_X = \frac{C_3 \cdot \frac{v_w}{v_T} + C_3 \cdot \alpha_y}{m_o \cdot s + \frac{C_3}{v_T}} \tag{2.4-23}$$

and substituting (2.4-23) into (2.4-22), and grouping terms

$$I_L \cdot s^2 \cdot \alpha_y + \left(C_2 + \frac{C_3 \cdot I_L}{v_T \cdot m_o} \right) \cdot s \cdot \alpha_y + \left(C_1 + \frac{C_2 \cdot C_3}{v_T \cdot m_o} \right) \cdot \alpha_y = -C_1 \cdot \frac{v_w}{v_T} \tag{2.4-24}$$

Both the rotational forcing coefficient and the damping coefficient have been modified by the inclusion of the rockets X-axis motion in the rotational equation. In both cases, a term has been added to the coefficients of the original rotational equation. Defining the new coupled coefficients as C_1' and C_2'

$$C_1' = C_1 + \frac{C_2 \cdot C_3}{v_T \cdot m_o} \tag{2.4-25}$$

$$C_2' = C_2 + \frac{C_3 \cdot I_L}{v_T \cdot m_o} \tag{2.4-26}$$

This paper uses the terms coupled rotational model, coupled coefficients, C_1' and C_2', coupled natural frequency, ω_n', and coupled damping ratio, ζ' to refer to those parameters derived from a coupling between the lateral rotational equation and X-axis equation of motion[23].

Solving the coefficients in terms of their constituent parameters from (2.4-16) to (2.4-18)

$$C_1' = \left(\frac{\rho}{2}\cdot A_r \cdot C_{N\alpha}\cdot {v_T}^2 \cdot (L_{CP}-L_{CG})\right)+\left(\frac{\left(\rho\cdot A_r \cdot C_{N\alpha}\cdot v_T \cdot (L_{CP}-L_{CG})\right)^2}{4\cdot m_o}\right) \tag{2.4-27}$$

$$C_2' = \left(\frac{\rho}{2}\cdot A_r \cdot C_{N\alpha}\cdot v_T \cdot (L_{CP}-L_{CG})^2\right)+\left(\frac{\rho}{2}\cdot A_r \cdot C_{N\alpha}\cdot v_T \cdot \frac{I_L}{m_o}\right) \tag{2.4-28}$$

Writing the coupled rotational equation (2.4-24) in terms of the new coupled coefficients

$$I_L \cdot s^2 \cdot \alpha_y \cdot + C_2' \cdot s \cdot \alpha_y + C_1' \cdot \alpha_y = -C_1 \cdot \frac{v_w}{v_T} \tag{2.4-29}$$

Equation (2.4-29) is the linearized coupled rotational dynamics equation just in terms of the state variable α_y, that includes the effects of the side-to-side X-axis motion of the rocket in free flight that increases the rockets rotational stability. The time domain equivalent of the linearized rotational equation (2.4-29) is

$$I_L \cdot \frac{d^2}{dt^2}\alpha_y + C_2' \cdot \frac{d}{dt}\alpha_y + C_1' \cdot \alpha_y = -C_1 \cdot \frac{v_w}{v_T} \tag{2.4-30}$$

If the rocket's side-to-side motion is constrained, for example, by a gimbal test mount used for wind tunnel testing, then the uncoupled rotational dynamics equation (2.1-10) would describe the rotational dynamics.

Regrouping the terms of the frequency domain equation (2.4-29) to ratio the output variable to the input variable creates a frequency gain function

---

[23] Mandell used the terms coupled natural frequency, ω_c, and coupled damping ratio, ζ_c, to refer to a different set of rotational parameters derived from a coupling between the lateral and longitudinal rotational equations in a 3-dimensional rotational stability model (Mandell, Caporaso, & Bengen, 1973, p. 175)

$$\frac{\alpha_y}{v_w} = \frac{-\frac{1}{v_T}\cdot\frac{C_1}{C_1'}}{\frac{I_L\cdot s^2}{C_1'}+\frac{C_2'}{C_1'}\cdot s+1} \tag{2.4-31}$$

Looking again at the general form of the second order differential equation from equation (2.1-13):

$$\frac{\alpha_y}{v_w} = K_{\alpha y}\cdot\frac{1}{\frac{s^2}{(\omega_n')^2}+\frac{2\cdot\zeta'\cdot s}{\omega_n'}+1} \tag{2.4-32}$$

then the coupled functions for natural frequency, damping ratio, and gain are:

$$\omega_n' = \sqrt{\frac{C_1'}{I_L}} = \sqrt{\frac{C_1+\frac{C_2\cdot C_3}{v_T\cdot m_o}}{I_L}} \tag{2.4-33}$$

$$\zeta' = \sqrt{\frac{(C_2')^2}{4\cdot C_1'\cdot I_L}} = \sqrt{\frac{\left(C_2+\frac{C_3\cdot I_L}{v_T\cdot m_o}\right)^2}{4\cdot\left(C_1+\frac{C_2\cdot C_3}{v_T\cdot m_o}\right)\cdot I_L}} \tag{2.4-34}$$

$$K_{\alpha y} = -\frac{1}{v_T}\cdot\frac{C_1}{C_1'} \tag{2.4-35}$$

Substituting back in the expressions for C_1' and C_2' from equations (2.4-27) and (2.4-28):

$$\omega_n' = v_T\cdot\sqrt{\frac{(\frac{\rho}{2})^2\cdot {A_R}^2\cdot C_{N\alpha}\cdot C_{L\alpha}\cdot(L_{CP}-L_{CG})^2+\frac{\rho}{2}\cdot A_R\cdot C_{N\alpha}\cdot(L_{CP}-L_{CG})\cdot m_o}{m_o\cdot I_L}} \tag{2.4-36}$$

$$\zeta' = \sqrt{\frac{\rho\cdot A_R\cdot\left(m_o\cdot C_{N\alpha}\cdot\left(L_{CP}-L_{CG}\right)^2+C_{L\alpha}\cdot I_L\right)^2}{8\cdot m_o\cdot I_L\cdot C_{N\alpha}\cdot\left(L_{CP}-L_{CG}\right)\cdot\left(\frac{\rho}{2}\cdot A_R\cdot C_{L\alpha}\cdot(L_{CP}-L_{CG})+m_o\right)}} \tag{2.4-37}$$

$$K_{\alpha y} = -\frac{1}{v_T} \cdot \frac{2 \cdot m_o}{\rho \cdot A_r \cdot C_{L\alpha} \cdot (L_{CP} - L_{CG}) + 2 \cdot m_o} \tag{2.4-38}$$

Like the uncoupled ω_n and ζ from equations (2.1-16) and (2.1-17), the coupled natural frequency, ω_n', and the coupled gain, $K_{\alpha y}$, are functions of the airstream velocity, v_T, but the coupled damping ratio, ζ', is not, so the same value of the damping ratio applies to the entire flight of the rocket.

The step response of equation (2.4-32) can be found by multiplying the step response for a second order system from equation (8.1-12) by the gain of equation (2.4-38)

$$\alpha_y\Big|_{step} = v_w \cdot K_{\alpha y} \cdot \left(-\frac{\zeta' \cdot \omega_n'}{\sqrt{(-\zeta'^2 + 1) \cdot \omega_n'^2}} \cdot e^{-(\zeta' \cdot \omega_n' \cdot t)} \cdot \sin\left(t \cdot \sqrt{(-\zeta'^2 + 1) \cdot \omega_n'^2} \right) - e^{-(\zeta' \cdot \omega_n' \cdot t)} \cdot \cos\left(t \cdot \sqrt{(-\zeta'^2 + 1) \cdot \omega_n'^2} \right) + 1 \right) \tag{2.4-39}$$

2.5 Comparing the Coupled and Uncoupled Linearized Models

This section will compare the output of the coupled and uncoupled linearized models to the complete model and look at the parametric differences between the two linearized models. The parameters for test rocket TR-1 are used for all the calculations.

The new linearized coupled rotational dynamics equation (2.4-29) and the coupled natural frequency and damping ratio were derived assuming a fixed value for v_T which does not occur during a normal model rocket flight. But the equations are valid for small perturbations that occur over small, or incremental changes in velocity centered about a fixed value of v_T, or operating point. Equation (2.4-29) can be used to analyze the rocket's rotational dynamic response to small perturbations in wind velocity compared to the velocity of the rocket. The second order step response equation (2.4-39) is used to calculate the step response of the second order equation (2.4-29) in terms of ω_n' and ζ'.

To compare the models, a 1 mph step in wind velocity that occurs at 1.5 seconds into the flight, just after motor burn out, when the rocket is travelling at 227 mph, will be used. At this velocity, for the coupled model, from equations (2.4-36) and (2.4-37)

$$\omega_n' = 2.240 Hz$$

$$\zeta' = 0.0539$$

and for the uncoupled model, from equations (2.1-16) and (2.1-17)

$$\omega_n = 2.238Hz$$
$$\zeta = 0.0105$$

Since

$$\omega_n = \sqrt{\frac{C_1}{I_L}}$$

and since the coupled and uncoupled natural frequencies are nearly the same, the coupled and uncoupled forcing coefficients must be nearly the same

$$\omega_n ' \simeq \omega_n \Rightarrow C_1 ' \simeq C_1 \tag{2.5-1}$$

The natural frequencies are nearly identical, but the coupled damping ratio is 5.13 times larger than the uncoupled damping ratio.

$$\frac{\zeta '}{\zeta} = 5.13$$

From the equation for the coupled damping coefficient, $C_2 '$, equation (2.4-28)

$$C_2 ' = \left(\frac{\rho}{2} \cdot A_r \cdot C_{N\alpha} \cdot v_T \cdot (L_{CP} - L_{CG})^2 \right) + \left(\frac{\rho}{2} \cdot A_r \cdot C_{N\alpha} \cdot v_T \cdot \frac{I_L}{m_o} \right)$$

The first term is the contribution due to the tangential rotational velocity and the second term is due to the X-axis side-to-side motion of the rocket. Taking the ratio of these two terms evaluating using the parameters for TR1

$$\frac{\left(\frac{\rho}{2} \cdot A_r \cdot C_{N\alpha} \cdot v_T \cdot \frac{I_L}{m_o} \right)}{\left(\frac{\rho}{2} \cdot A_r \cdot C_{N\alpha} \cdot v_T \cdot (L_{CP} - L_{CG})^2 \right)} = \frac{\frac{I_L}{m_o}}{(L_{CP} - L_{CG})^2} = 4.13$$

which says that the side-to-side X-axis motion is 4.13 times larger than the tangential rotational motion at the center of pressure. The sum of the two components would then be 5.13 times the tangential rotational motion alone, which is consistent with the ratio of the damping ratios.

Figure 2-16 compares the step response of the full model simulation (red trace) to the coupled equation (2.4-29) (black trace) for the 1 mph step in wind velocity. This plot shows the closed form linear rotational dynamics equation (2.4-29) is a very good approximation of the rocket's initial rotational dynamic behavior. The initial step and overshoot matches the full simulation very closely as the fixed value of v_T used for equation (2.4-29) was taken from the full simulation for that point in time. The frequency of the ringing of the full simulation does decrease a little with time compared to equation (2.4-29) because the rocket is in coast phase and the velocity is decreasing, and the final value of the step for the full model increases a little due to the other forces, including the force due to gravity, that are not included in the linearized model, that cause the rocket to arc over as its velocity decreases. As the natural frequency decreases, the time it takes for the oscillations to decay increases, even though the damping ratio remains constant, so the damping ratio is a good predictor of the rotational stability.

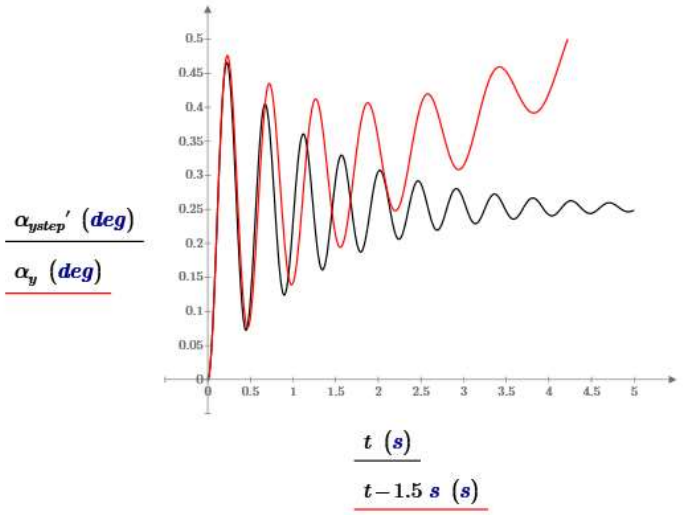

Figure 2-16 Full simulation (red trace) and second order equation response (black trace) to a 1 mph step in wind velocity at 1.5 seconds into the flight, just after motor burn-out, using the value $\zeta' = 0.052$ from the coupled rotational equation (2.4-39)

Figure 2-17 shows the step response for the same 1 mph step in wind velocity using the uncoupled rotational equation. The smaller damping ratio results in a step response that has a much longer exponential decay than the full simulation. This shows how the rotational equation (2.2-7) alone without the v_X cross coupling term significantly underpredicts the stability of the system.

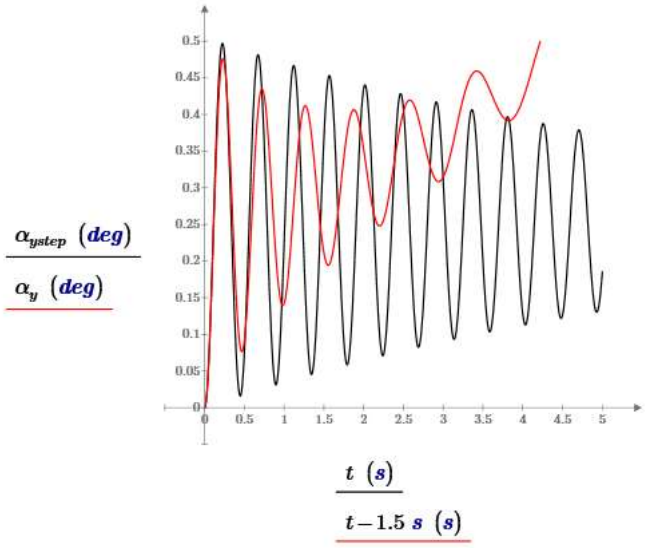

Figure 2-17 Full simulation (red trace) and second order equation response (black trace) to a 1 mph step in wind velocity at 1.5 seconds into the flight, just after motor burn-out, using the value of $\zeta = 0.011$ from the rotational equation (2.1-18) alone

The equations for the coupled natural frequency, (2.4-36), and coupled damping ratio, (2.4-37), are more complex than the equations for the uncoupled natural frequency, (2.1-16), and the uncoupled damping ratio (2.1-17). The simpler the equation the easier it is to see its dependence on each of the rocket parameters. Knowing that the coupled and uncoupled natural frequencies are nearly the same, it is possible to replace the coupled equation with the simpler uncoupled equation

$$\omega_n' = \sqrt{\frac{C_1'}{I_L}} \simeq \omega_n = \sqrt{\frac{C_1}{I_L}} = v_T \cdot \sqrt{\frac{\rho \cdot A_r \cdot C_{N\alpha} \cdot (L_{CP} - L_{CG})}{2 \cdot I_L}} \tag{2.5-2}$$

Relating the natural frequency to the rocket design parameters would appear straightforward. The natural frequency increases with an increasing normal force coefficient and increasing distance between the center of pressure and the center of gravity and decreases with increasing moment of inertia. But all the parameters, area of the rocket, the normal force coefficient, the moment of inertia, and the distance between the center of pressure and center of gravity, are interactive. Changing any one of these changes the others; they cannot be changed independently in an actual rocket design. A set of sensitivity analyses will be used in section 2.8 to show more clearly how the natural frequency and other rotational dynamics parameters are affected by changes to key rocket design parameters.

Knowing that $C_1' \simeq C_1$ from (2.5-2), the equation for the coupled damping ratio can be simplified

$$\zeta' = \sqrt{\frac{C_2'^2}{4 \cdot C'_1 \cdot I_L}} \simeq \sqrt{\frac{C_2'^2}{4 \cdot C_1 \cdot I_L}} = \sqrt{\frac{\rho \cdot A_r \cdot C_{N\alpha}}{8} \cdot \frac{(L_{CP} - L_{CG})^3}{I_L}} + \sqrt{\frac{\rho \cdot A_r \cdot C_{N\alpha}}{8} \cdot \frac{I_L}{m_o^2 \cdot (L_{CP} - L_{CG})}} \qquad (2.5\text{-}3)$$

and since

$$\zeta = \sqrt{\frac{\rho \cdot A_r \cdot C_{N\alpha} \cdot (L_{CP} - L_{CG})^3}{8 \cdot I_L}}$$

then

$$\zeta' = \zeta + \sqrt{\frac{\rho \cdot A_r \cdot C_{N\alpha}}{8} \cdot \frac{I_L}{m_o^2 \cdot (L_{CP} - L_{CG})}} \qquad (2.5\text{-}4)$$

In the coupled damping ratio equation (2.5-4), the first term is the component contributed by the uncoupled rotational damping, and the second term is the component contributed by the side-to-side X-axis motion of the rocket . The uncoupled damping ratio increases with increasing normal force coefficient and increasing distance between the center pressure and the center of gravity. It decreases with increasing moment of inertia. The term added by the X-axis motion increases with increasing normal force coefficient and moment of inertia. It decreases with increasing mass and increasing distance between the center of pressure and the center of gravity.

The second term added by the X-axis motion is the larger contributor to the overall damping ratio, and it is comprised of only six parameters. But, like the natural frequency, the parameters are all interactive, and they cannot be changed independently in an actual rocket design. The sensitivity analyses in section 2.8 will be used to show how the coupled damping ratio is affected by changes to key rocket design parameters.

2.6 Linearized Coupled X-Axis Motion Equation

In the same way a linearized equation can be derived just in terms of the y-axis rotation angle, α_y, that includes the effects of the X-axis side-to-side motion, a linearized equation can also be derived just in terms the X-axis velocity, v_X, that includes the effects of the rocket's rotation.

Before solving for the coupled X-axis equation of motion, the X-axis equation can be rearranged to show how the coupling term impacts the equation. The X-axis equation of motion (2.4-13) is

$$m_o \cdot s \cdot v_X + \frac{C_3}{v_T} \cdot v_X - C_3 \cdot \alpha_y = C_3 \cdot \frac{v_w}{v_T} \tag{2.6-1}$$

Rearranging the terms of equation (2.3-9) for the linearized distance the rocket swings at the center of pressure due to its rotation

$$\alpha_y = -\frac{d_{\alpha y}}{L_{CP} - L_{CG}} \tag{2.6-2}$$

and substituting equation (2.6-2) into equation (2.6-1) and rearranging the terms

$$m_o \cdot \frac{d}{dt} v_X + \frac{C_3}{v_T} \cdot v_X + \frac{C_3}{L_{CP} - L_{CG}} \cdot d_{\alpha y} = C_3 \cdot \frac{v_w}{v_T} \tag{2.6-3}$$

This form of the X-axis equation of motion is the counterpart to the equation of rotation (2.3-5) where the term due to the side-to-side velocity was grouped with the linearized rotational velocity damping term to show the two components of the coupled damping equation. In this case, the term that comes from the coupling with the rotational equation provides a first order driving term to X-axis equation of motion that is proportional to the tangential displacement of the rocket's rotation. This term is the driver of the side-to-side motion along the X-axis, so equation (2.6-3) shows how the coupling with the rotational equation impacts the X-axis motion.

Next, the X-axis equation of motion will be solved in terms of v_X. Solving the coupled rotational dynamics equation (2.4-22) for α_y in terms of v_X

$$\alpha_y = \frac{C_1 \cdot \left[-\frac{v_w}{v_T} + \frac{v_X}{v_T} \right]}{I_L \cdot s^2 + C_2 \cdot s + C_1} \tag{2.6-4}$$

The frequency domain version of the X-axis equation of motion (2.4-20) is

$$m_o \cdot s \cdot v_X + \frac{C_3}{v_T} \cdot v_X = C_3 \cdot \frac{v_w}{v_T} + C_3 \cdot \alpha_y \tag{2.6-5}$$

Substituting equation (2.6-4) into equation (2.6-5) and rearranging terms

$$I_L \cdot s^2 \cdot v_X + \left(C_2 + \frac{C_3 \cdot I_L}{v_T \cdot m_o} \right) \cdot s \cdot v_X + \left(C_1 + \frac{C_2 \cdot C_3}{v_T \cdot m_o} \right) \cdot v_X = \frac{C_2 \cdot C_3}{m_o} \cdot \left[\frac{I_L}{C_2} \cdot s + 1 \right] \cdot \frac{v_w}{v_T} \tag{2.6-6}$$

which has a form similar to the rotational equation (2.4-24). Using equations (2.4-25) and (2.4-26) for C_1' and C_2', equation (2.6-5) becomes

$$I_L \cdot s^2 \cdot v_X + C_2' \cdot s \cdot v_X + C'_1 \cdot v_X = \frac{C_2 \cdot C_3}{m_o} \cdot \left[\frac{I_L}{C_2} \cdot s + 1 \right] \cdot \frac{v_w}{v_T} \tag{2.6-7}$$

Regrouping the terms of equation (2.6-7) to ratio the output variable to the input variable creates a frequency gain function

$$\frac{v_X}{v_w} = \frac{\frac{1}{v_T} \cdot \frac{C_2 \cdot C_3}{m_o \cdot C_1'} \cdot \left[\frac{I_L}{C_2} \cdot s + 1 \right]}{\frac{I_L \cdot s^2}{C_1'} + \frac{C_2'}{C_1'} \cdot s + 1} \tag{2.6-8}$$

Again, because the coefficient C_3 from equation (2.4-11) is a function of the total airstream velocity, this model applies only incrementally about a fixed operating point of v_T. The general from of the equation with second order poles in the denominator and a first order zero in the numerator is

$$\frac{v_X}{v_w} = K_{vx} \cdot \frac{\frac{s}{\omega_z} + 1}{\frac{s^2}{(\omega_n')^2} + \frac{2 \cdot \zeta' \cdot s}{\omega_n'} + 1} \tag{2.6-9}$$

where ω_n' and ζ' are the same as the values for the linearized coupled rotational equation (2.4-32) and are given by equations (2.4-36) and (2.4-37). The zero (root of the numerator) frequency is

$$\omega_z' = \frac{C_2}{I_L} = \frac{\rho}{2} \cdot \frac{A_r \cdot C_{N\alpha} \cdot v_T \cdot (L_{CP} - L_{CG})^2}{I_L} \tag{2.6-10}$$

and, assuming $C_1' \simeq C_1$ as shown in Equation (2.5-1) the gain is given by

$$K_{vx} = \frac{1}{v_T} \cdot \frac{C_2 \cdot C_3}{m_o \cdot C_1'} = \frac{\rho}{2} \cdot \frac{A_r \cdot C_{L\alpha} \cdot (L_{CP} - L_{CG})}{m_o} \tag{2.6-11}$$

The denominator of the linearized gain equation for the X-axis side-to-side motion, (2.6-9), is the same as the denominator of the gain equation for the y-axis rotation, (2.4-32), so both have the same natural frequency and damping ratio. The zero in the numerator of the v_X gain equation is at a frequency, 0.049 Hz for TR-1, much lower

than the frequency of the poles of the denominator, 2.33 Hz. Unlike the rotational equation, the gain in this equation is not a function of the velocity of the total oncoming airstream, v_T .

The step response can be found by taking the inverse Laplace transform of equation (2.6-9). Multiplying the step response equation of a second order system with a zero from equation (8.6-2) by the gain of equation (2.6-11) results in

$$v_X{}'|_{step} = v_w \cdot K_{vx} \cdot \left(\frac{\omega_n{}'^2 - \zeta' \cdot \omega_n' \cdot \omega_z'}{\omega_z' \cdot \sqrt{(-\zeta'^2 + 1) \cdot \omega_n{}'^2}} \cdot e^{-(\zeta' \cdot \omega_n' \cdot t)} \cdot \sin\left(t \cdot \sqrt{(-\zeta'^2 + 1) \cdot \omega_n{}'^2} \right) - e^{-(\zeta' \cdot \omega_n' \cdot t)} \cdot \cos\left(t \cdot \sqrt{(-\zeta'^2 + 1) \cdot \omega_n{}'^2} \right) + 1 \right) \tag{2.6-12}$$

Figure 2-18 shows the complete model simulation (red trace) and linearized equation step response (black trace), equation (2.6-12), for the side-to-side velocity of the rocket, v_X . The magnitude and the decay envelope match very closely. The frequency matches best around the burnout velocity at 1.3 seconds, which is the velocity used in the linearized equation. The full simulation starts at a lower frequency and then ends at a lower frequency because of the actual velocity trajectory of the rocket. The low frequency zero in the gain function means the final value of the step response is small compared to the magnitude of the oscillation envelope. The magnitude of the oscillations is proportional to the wind velocity, v_w , but is not a function of the velocity of the oncoming airstream, v_T . This is not surprising because the side-to-side velocity of the rocket provides the increased damping in the rotational equation, and the damping ratio is not a function of the rocket's velocity.

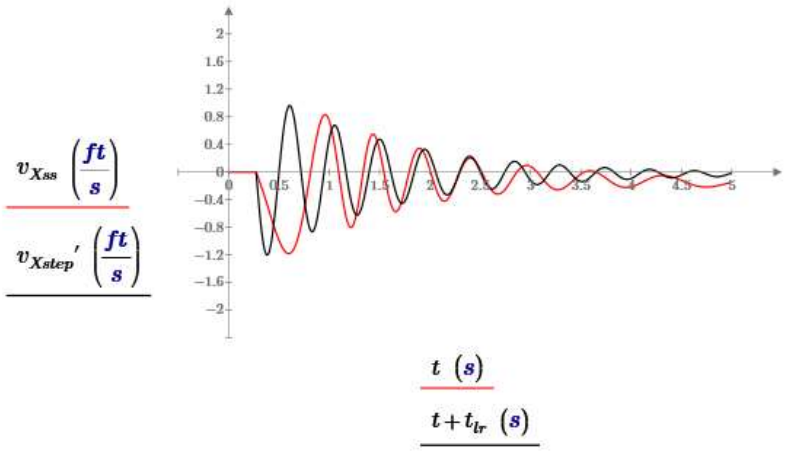

Figure 2-18 Complete model simulation for test rocket TR-1 (red) and linearized equation step response (black) for the v_X side-to-side velocity of the rocket for a 10 mph step in the wind velocity

The side-to-side distance the rocket travels along the X-axis is easier to visualize than the velocity. The distance is determined by integrating the velocity equation by multiplying the frequency domain equation (2.6-9) by $1/s$. The step response is then found by taking the inverse Laplace transform. Multiplying the step response equation of the integrated second order system with a zero from (8.6-2), by the gain of equation (2.6-11) results in

$$d_X'|_{step} = w \cdot K_{vx} \cdot \left(\begin{array}{l} \frac{\left(2 \cdot \zeta^2 - 1\right) \cdot \omega_n \cdot \omega_z - \zeta \cdot \omega_n^2}{\omega_n \cdot \omega_z \cdot \sqrt{(-\zeta^2 + 1) \cdot \omega_n^2}} \cdot e^{-(\zeta \cdot \omega_n \cdot t)} \cdot \sin\left(t \cdot \sqrt{(-\zeta^2 + 1) \cdot \omega_n^2}\right) + \\ + \frac{2 \cdot \zeta \cdot \omega_z - \omega_n}{\omega_n \cdot \omega_z} \cdot e^{-(\zeta \cdot \omega_n \cdot t)} \cdot \cos\left(t \cdot \sqrt{(-\zeta^2 + 1) \cdot \omega_n^2}\right) + \frac{\omega_n \cdot \omega_z \cdot t + \left(\omega_n - 2 \cdot \zeta \cdot \omega_z\right)}{\omega_n \cdot \omega_z} \end{array} \right) \quad (2.6\text{-}13)$$

Figure 2-19 shows the complete model simulation (red trace) and linearized equation (2.6-13) step response (black trace) for the side-to-side distance of the rocket, d_X. The initial step of the linearized equation is lower since the velocity term in the full simulation spends more time during its first negative half cycle than it does during its first positive half cycle because of the increasing frequency of the sinusoid due to the increasing velocity, and that difference is integrated in the distance term, but the envelope and frequency of the oscillations match very closely.

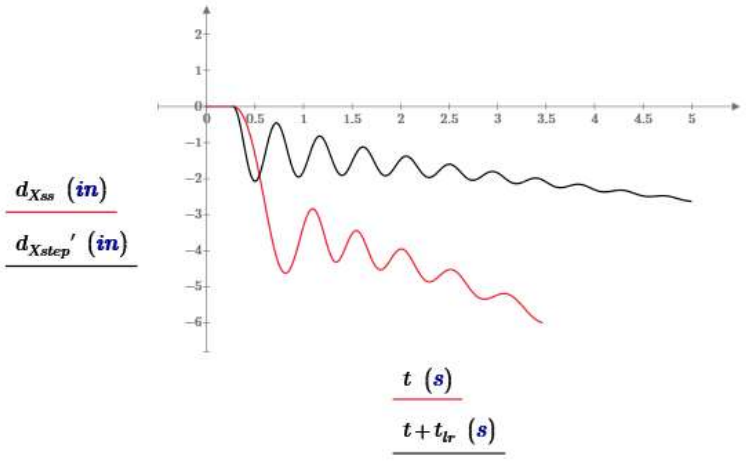

Figure 2-19 Complete model simulation for test rocket TR-1 (red) and linearized equation step response (black) for the d_X side-to-side velocity of the rocket for a 10 mph step in the wind velocity

Figure 2-20 and Figure 2-21 show the rotational step response and the side-to-side X-axis velocity step responses for TR-1 for two different nose weight masses. In Figure 2-20, the less stable system, the nose weight mass is +4 oz and the coupled damping ratio is $\zeta' = 0.052$. For Figure 2-21, the more stable system, the nose weight mass is -12

oz, and the coupled damping ratio is $\zeta' = 0.12$. The X-axis side-to-side velocity provides the largest portion of the damping term in the coupled rotational equation. In the more stable system in Figure 2-21, the magnitude of the X-axis velocity is greater, even though the oscillations decay faster. The larger magnitude of the side-to-side motion causes the system to be more stable, but because both the rotational response and the side-to-side response have the same natural frequency and damping ratio, the side-to-side motion also decays faster than it does for the less stable system in Figure 2-20.

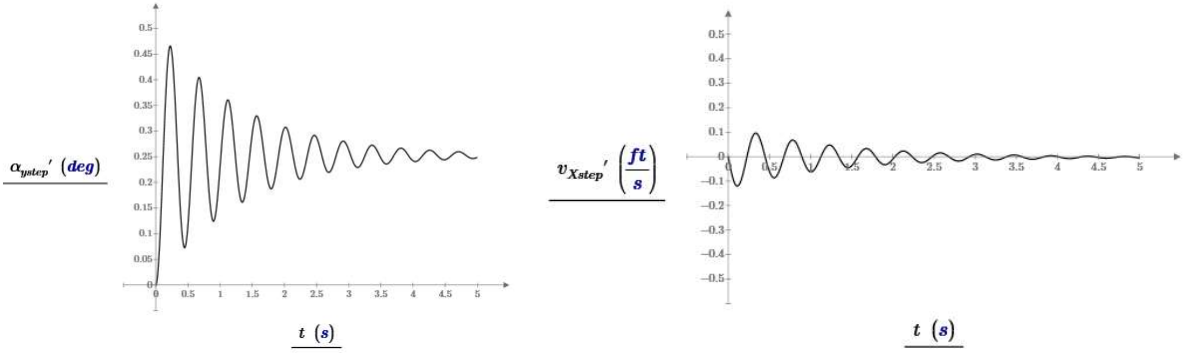

Figure 2-20 Linearized model of the rotational step and the X-axis side-to-side step for a nosecone weight mass of +4 oz and a 1 mph step in the wind velocity

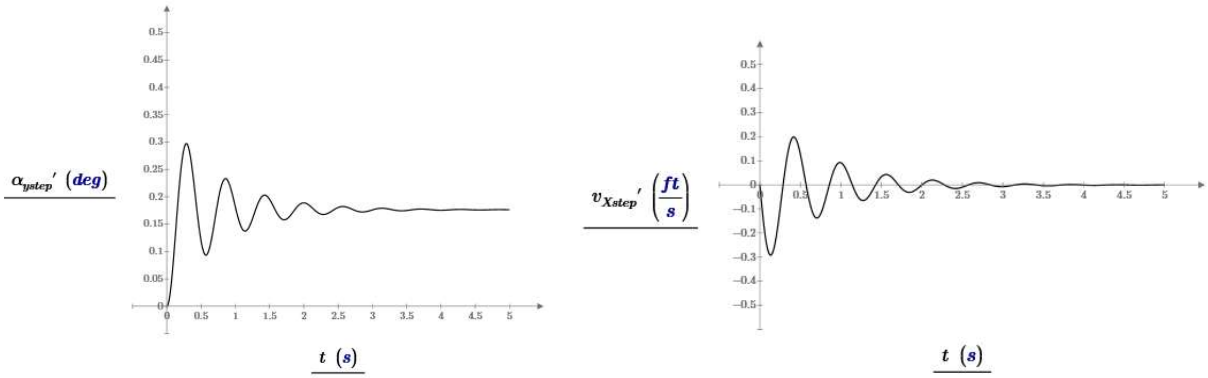

Figure 2-21 Linearized model of the rotational step and the X-axis side-to-side step for a nosecone weight mass of –12 oz and a 1 mph step in the wind velocity

2.7 Frequency Response of a Rocket's Rotational Dynamics

So far, the rotational dynamics of a rocket has been analyzed as the time domain response to a step in the wind velocity. There is also value analyzing the dynamic stability in the frequency domain. For example, the rocket's rotational dynamics frequency domain gain function is needed when designing the control loop for a vertical trajectory system or a thrust vector stabilization system. The rocket dynamics gain function is a part of the control loop and is needed to ensure an effective and stable control loop design.

Figure 2-22 shows a Bode plot, log magnitude versus log frequency, of the frequency domain coupled rotational dynamics equation (2.4-32) for test rocket TR-1. It shows the magnitude of the gain is 0.24 deg/mph when the rocket is traveling at its motor burn-out velocity of 235 mph. That is, the rocket rotates -0.24 degrees for every 1 mph in lateral wind velocity. The rocket will respond to a wind perturbation rate up to the 3 dB bandwidth, f_{3dB}, of the rocket's rotational dynamics, where $\omega_{3dB} = 3.6Hz$, calculated using the second order 3 dB bandwidth equation[24]

$$\omega_{3dB} = \omega_n \cdot \sqrt{1 - 2 \cdot \zeta^2 + \sqrt{2 - 4 \cdot \zeta^2 + 4 \cdot \zeta^4}} \tag{2.7-1}$$

and the values $\omega_n = 2.3Hz$ and $\zeta' = 0.054$. Above that frequency, the response falls off rapidly. The rocket will respond to bursts in the wind velocity that have a duration that is longer than $1/f_{3dB}$, or 0.28 seconds, but not respond to bursts in the wind velocity that are much shorter in duration than that (most wind bursts are probably longer than 0.28 seconds). There is a large peak in gain at the natural frequency of the system, but it is much smaller than the uncoupled system predicts due to the smaller uncoupled damping ratio. The peak occurs at the frequency of the oscillation seen in the step response. That peak can impact the stability of a control loop that includes the rockets rotational dynamics, so knowing the actual coupled value of the damping ratio is important for control loop designs.

[24] (Roberge, 1975, p. 95)

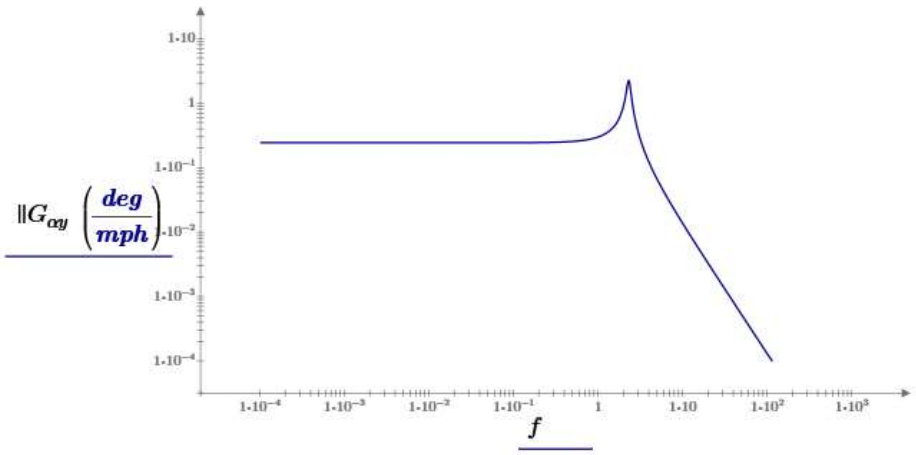

Figure 2-22 Frequency response of the rotational dynamics system for test rocket TR-1 at $v_t = 235 mph$

As can be seen from the equations (2.4-36) and (2.4-38), both the rotational gain constant, $K_{\alpha y}$, and the natural frequency, ω_n', are a function of the total velocity of the oncoming airstream. Figure 2-23 shows a plot of the rotational gain constant versus the velocity of the total oncoming airstream. The gain falls off very rapidly with increasing velocity above a corner velocity of around 40 mph. This shows why it is important to have a minimum velocity for the rocket as it leaves the launch guide, as the susceptibility of the rocket to the lateral wind is greatly reduced above that velocity. This shows a minimum safe launch velocity of around 40 mph as the rocket leaves the launch guide. At 40 mph a rocket would rotate at most 15 degrees into a 10 mile per hour wind. Although this is a plot of the complete gain expression, equation (2.4-38), it is nearly identical to $1/v_T$. Test rocket TR-1 leaves the launch guide at 49.9 mph and reaches 235 mph at motor burnout so the rotational gain constant ranges from $-1.15\,\mathrm{deg/mph}$ to $-0.24\,\mathrm{deg/mph}$. Because the rocket's velocity continues to increase as it leaves the launch guide and the step response does not fully respond to the initial step, the actual turn would be less than this.

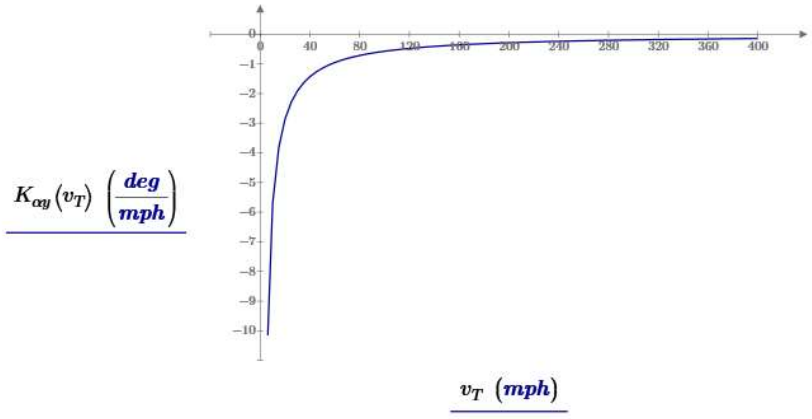

Figure 2-23 Rotational gain constant versus the total velocity of the oncoming airstream for test rocket TR-1

Figure 2-24 shows the natural frequency and 3 dB bandwidth of the rocket versus the total velocity of the oncoming airstream. Figure 2-25 shows the minimum duration of the wind events that the rocket will respond to, $1/f_{3dB}$. As seen above, that duration is 0.28 seconds at motor burnout velocity. But the minimum duration is 1.3 seconds as the rocket leaves the launch guide, so the rocket is less sensitive to shorter bursts in wind as it leaves the launch guide. If the velocity of the wind changes slowly compared to the minimum response duration, the rocket will respond. But if the burst is short compared to the minimum response duration for the velocity of the rocket at the time the burst occurs, then the rocket's response will be greatly attenuated.

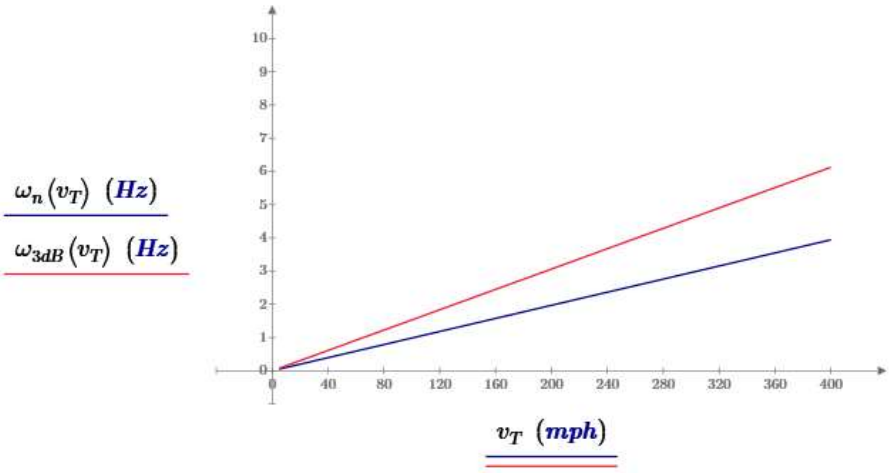

Figure 2-24 Natural frequency, ω_n , and 3 dB bandwidth, ω_h ,versus the total velocity of the oncoming airstream for test rocket TR-1

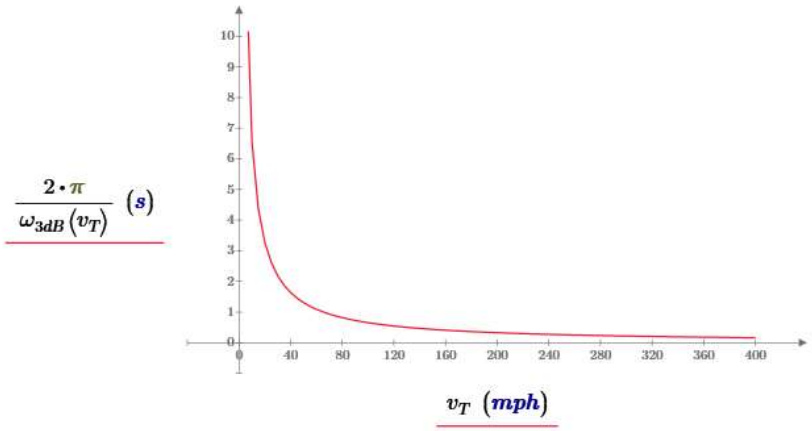

Figure 2-25 Minimum duration of wind bursts the rocket will respond to versus the total velocity of the oncoming airstream for test rocket TR-1

The bandwidth of the rotational dynamics increases with increasing velocity of the oncoming airstream, increasing the sensitivity to fast bursts of wind, but, at the same time, the gain of the rotational dynamics decreases with increasing velocity. Figure 2-26 shows the rotational dynamics frequency response at two different airstream velocities, the velocity at which the rocket leaves the launch guide (blue trace), and the velocity at motor burnout (red trace). It shows that even though the rocket has a higher bandwidth at higher velocities, the reduction in gain is enough that, overall, the rocket will be less susceptible to most changes in the wind the higher the rocket's velocity.

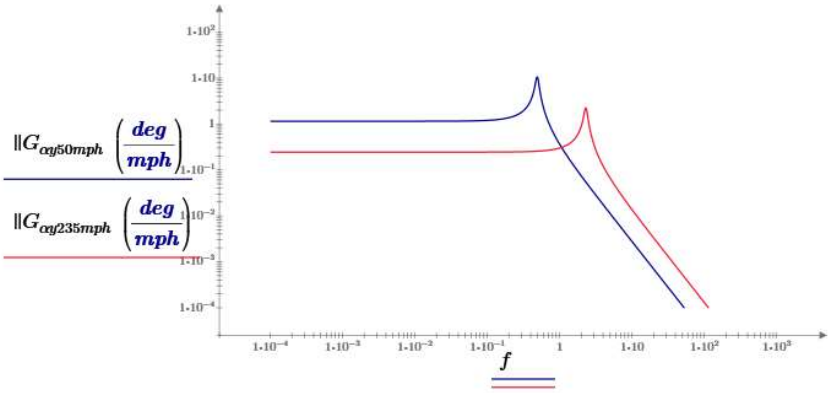

Figure 2-26 Rotational gain versus frequency at a total velocity of the oncoming airstream of 50 mph and 235 mph for test rocket TR-1

2.8 Rotational Dynamics Stability Sensitivities

The equations for the natural frequency and coupled damping ratio are complex functions of the model parameters, C_A, m_o, I_L, $C_{N\alpha}$, and $(L_{CP} - L_{CG})$. It is difficult to see intuitively the impact a change in the parameters has on the natural frequency or damping ratio. Sensitivity analyses, where the expressions are evaluated numerically, will be used to show how the natural frequency and coupled damping ratio are affected by changes to the model parameters.

In addition, the model parameters cannot be changed individually in an actual rocket design. The fin size, body tube length, nose weight mass, and the density of the construction material are the key parameters that are available to the designer. Table 2-1 shows the how these design parameters impact the model parameters. Most of the design parameters affect the model parameters in only one direction. But the fin size may increase or decrease the stability margin (distance between the center of pressure and center of gravity). Increasing the fin size moves the center of pressure rearward, but it also moves the center of gravity rearward due to the increase in the mass of the larger fins. Depending upon which increases at a faster rate, the stability margin can either increase or decrease.

	Model Parameters			
Design Parameters	m_o	I_L	$C_{N\alpha}$	$L_{CP} - L_{CG}\ (SM)$
Increase Nosecone Mass	$\Uparrow$	$\Uparrow$	$\Leftrightarrow$	$\Uparrow$
Increase Body Tube Length	$\Uparrow$	$\Uparrow$	$\Leftrightarrow$	$\Uparrow$
Increase Fin Size	$\Uparrow$	$\Uparrow$	$\Uparrow$	$\Uparrow$ or $\Downarrow$
Material Density	$\Uparrow$	$\Uparrow$	$\Leftrightarrow$	$\Downarrow$

Table 2-1 Interaction between key rocket design parameters and the parameters that drive dynamic stability

Figure 2-27 to Figure 2-30, show the stability parameter sensitivities to the mass of the nose cone weight, the body tube length, the fin size, and the material density, all of which change the stability margin of the rocket. The graphs show the stability margin, *SM* (distance between the center of gravity an center of pressure), the coupled and uncoupled damping ratios, ζ and ζ', and the coupled and uncoupled natural frequencies ω_n and ω_n'. All the parameters for the graphs come from the closed form linearized model evaluated at the burnout mass and velocity of the rocket. All the graphs are calculated using the component parameters from test rocket TR-1 except for the one parameter that is being varied about its nominal value from TR-1. Each graph indicates the nominal parameter value for TR-1 which has a 2.6 caliber stability margin at motor burnout. Each graph also indicates the value of the

parameter for 1 caliber of stability margin, which is normally considered to be the minimum stability margin for a rocket.

Since TR-1 starts with a 2.6 caliber stability margin, a negative value of nose weight mass, which is possible in a simulation, is used to give a sensitivity range that covers lower values of stability margin. The fin scaling sensitivity, k, is a linear scaling factor for the size of the fin, with a value of 1 being the nominal size of TR-1's fins. The material density sensitivity assumes all the rocket is constructed from material of the same density. The range of densities includes the density of paper and balsa up through epoxy/fiberglass. For the TR-1 design, it is not possible to get to 1 caliber of stability margin by just varying the material density, using a reasonable range of material densities.

Traditionally, increasing the stability margin of a rocket, the distance the center of pressure is ahead of the center of gravity, is expected to increase the rocket's stability[25]. The key indicator of stability is the damping ratio, ζ. The sensitivity plots show that the coupled and uncoupled damping ratios behave very differently. The coupled damping ratio is always larger than the uncoupled. The uncoupled damping ratio always moves in the same direction as the stability margin, being directly proportion to the stability margin. But the coupled damping ratio often moves in the direction opposite the uncoupled damping ratio and stability margin, which indicates the traditional stability margin, or distance between the center of gravity and the center of pressure, is not a good indicator of the rotational stability of a rocket. For TR-1, the coupled damping ratio increases significantly below 1 caliber of stability margin as the center of gravity approaches the center of pressure, for all the stability sensitivities except material density.

The plots of the natural frequency, ω_n, show that there is no discernible difference between the coupled and uncoupled values over the full range of rocket design parameters as expected from section 2.5. The natural frequency changes the most for the material density, decreasing with increasing density.

These sensitivities are centered about the nominal design of test rocket TR-1 which is a typical design for a small fiberglass high power rocket. A rocket with a significantly different set of initial design parameters such as a smaller model rocket built from lighter materials or a much larger high-power rocket, would have different sensitivities.

The value of the damping ratio shown on the sensitivity graphs applies to the entire flight of the rocket because the damping ratio is not a function of the rocket's velocity. This says that the stability of the rocket does not change during the flight even though the natural frequency, which is proportional to the velocity, does change.

---

[25] (Barrowman J. , 1968, p. 5)

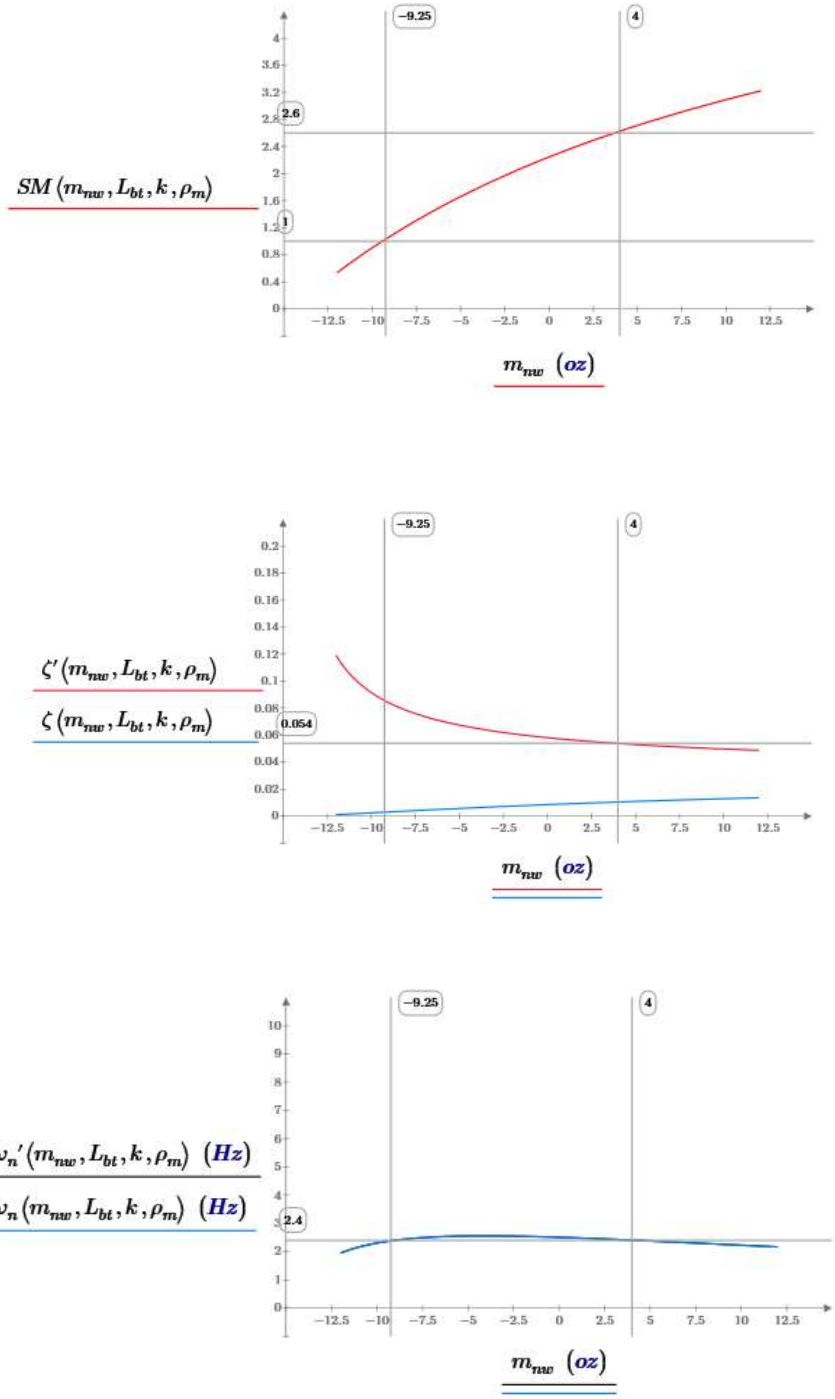

Figure 2-27 Stability parameter sensitivities to nosecone weight mass - the nominal nosecone mass for TR-1 is 4 oz

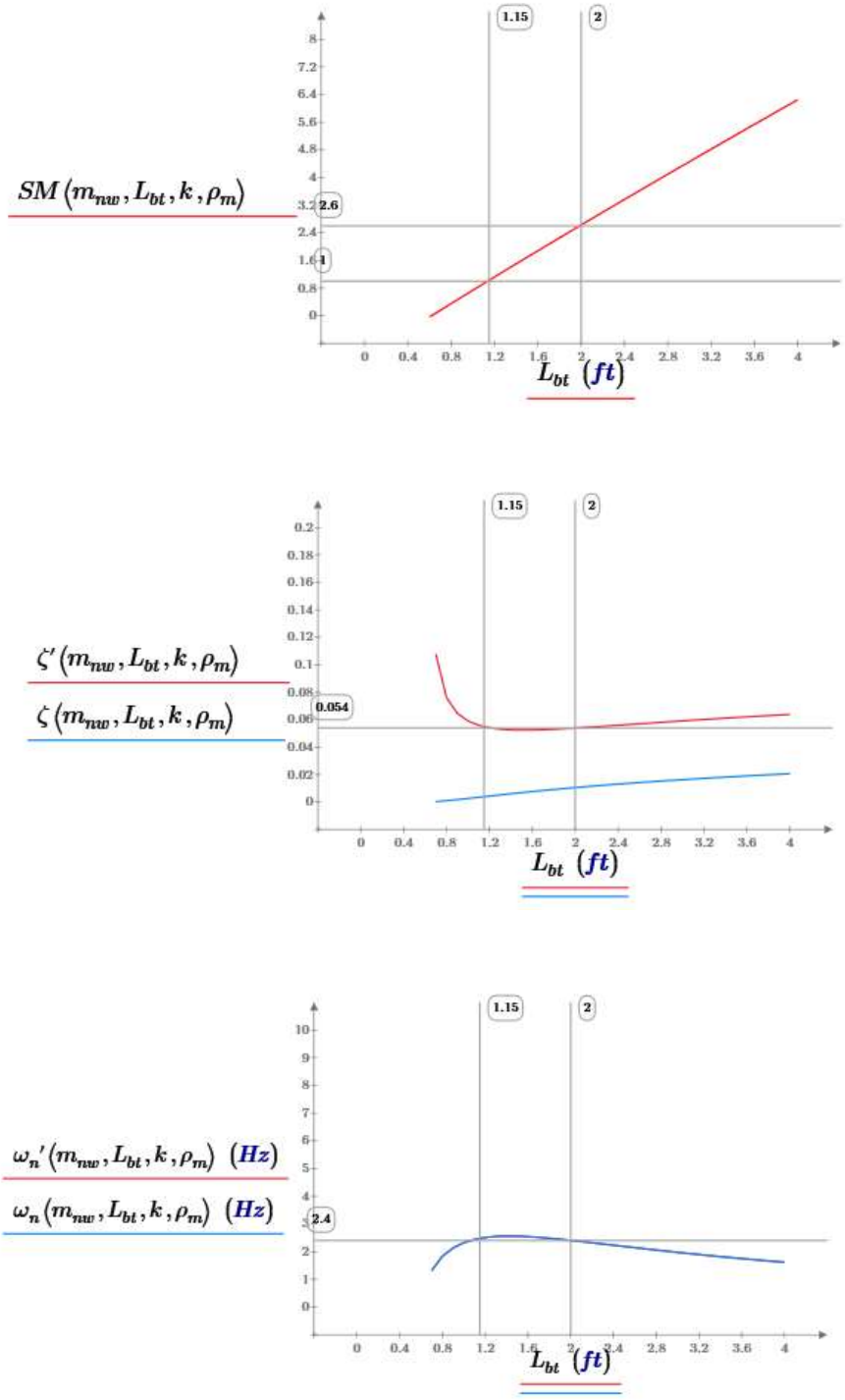

Figure 2-28 Stability parameter sensitivities to body tube length - the nominal body tube length for TR-1 is 2 ft

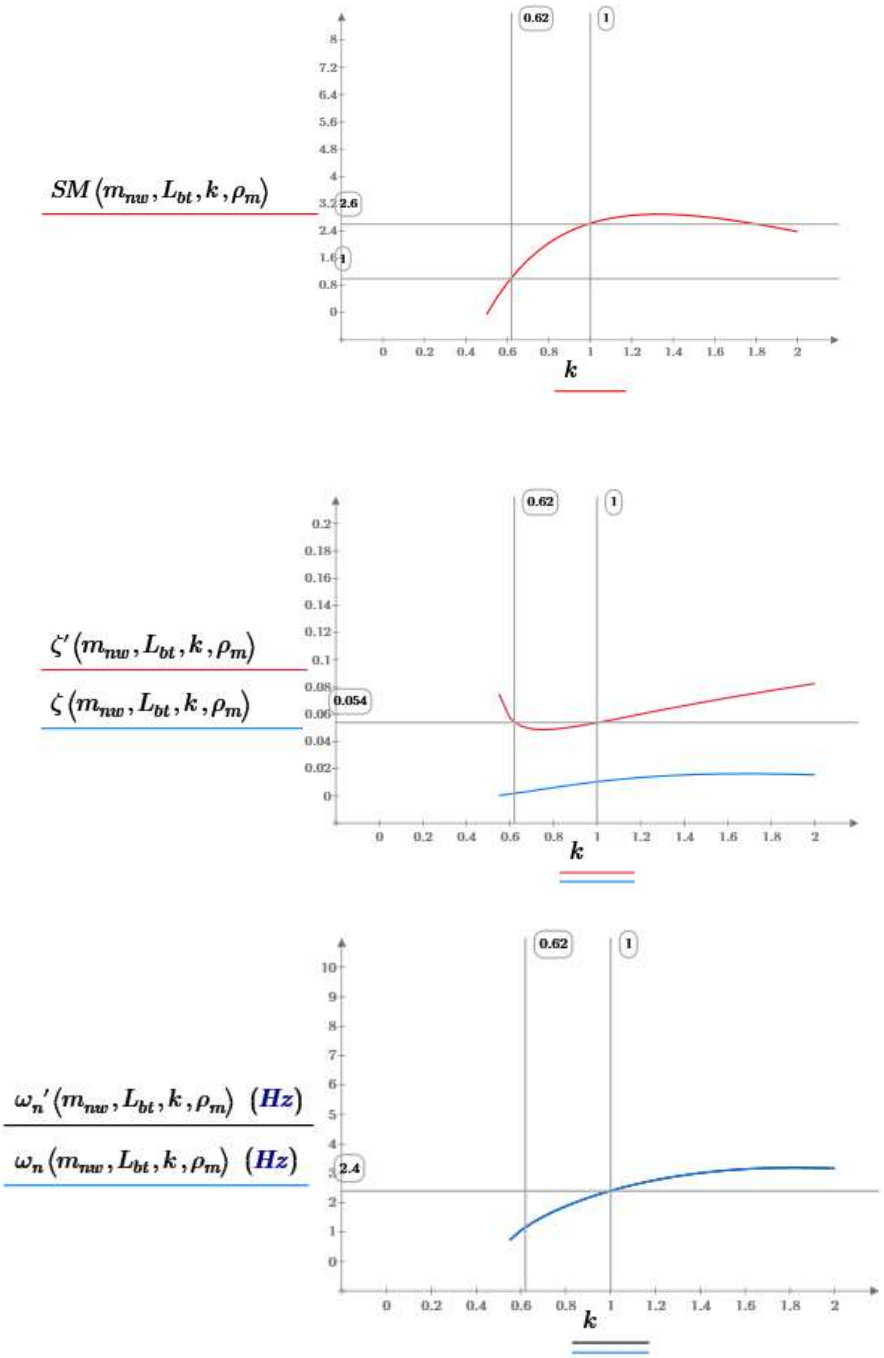

Figure 2-29 Stability parameter sensitivities to fin scaling factor - the nominal scaling factor for TR-1 is 1

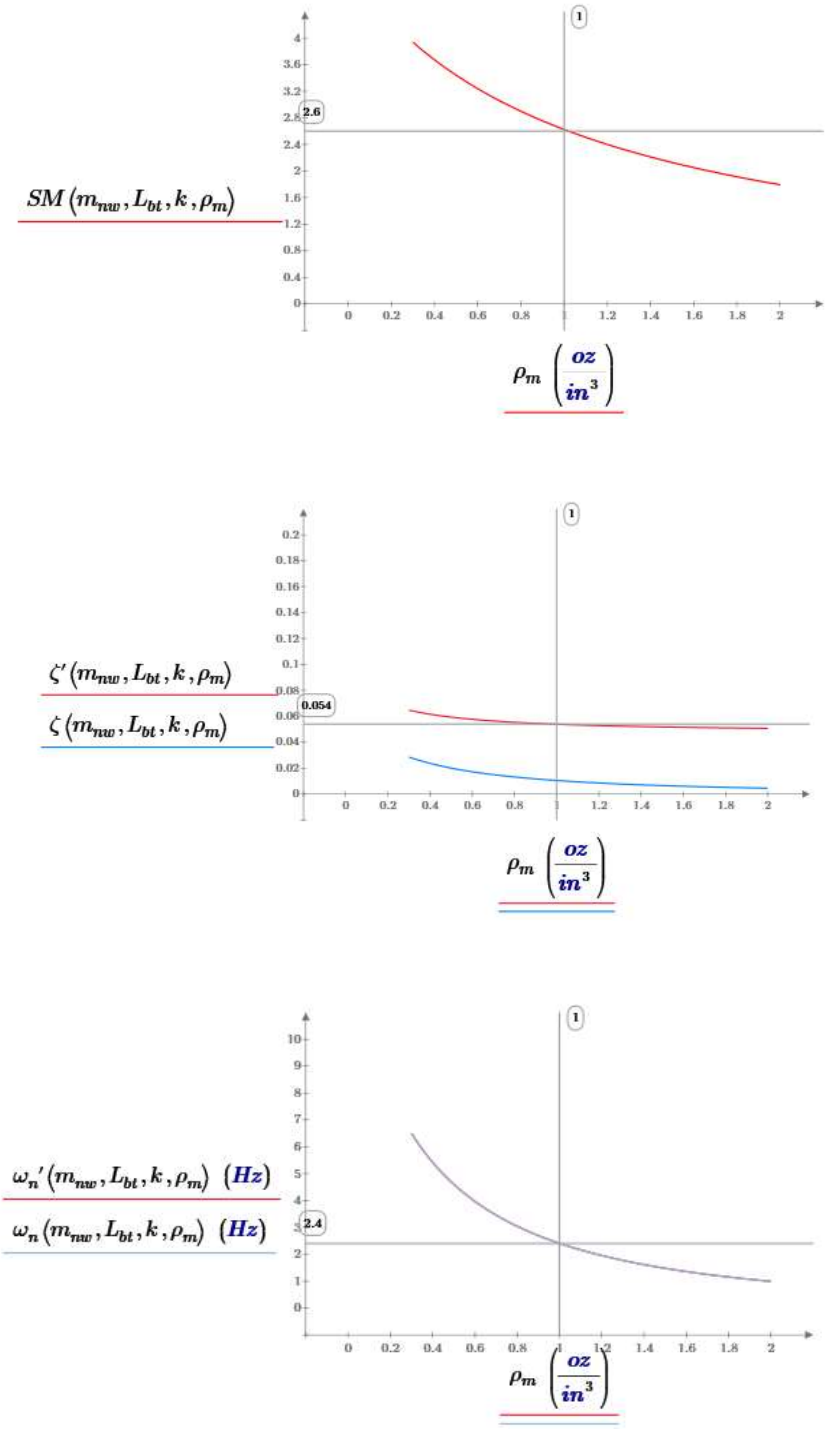

Figure 2-30 Stability parameter sensitivities to construction material density - the nominal material density for TR-1 is $1 \cdot oz / in^3$ (fiberglass)

Figure 2-20 showed that a system with greater rotational stability has a larger X-axis sided-to-side velocity, which provides the greater damping. From equation (2.5-3) and (2.5-4), it was shown that the coupled damping ratio is the sum of the uncoupled damping ratio plus a second term that includes the effects of the damping due to the X-axis side-to-side velocity of the rocket

$$\zeta' = \zeta + \zeta_{vxss} \tag{2.8-1}$$

where the uncoupled damping ratio is

$$\zeta = \sqrt{\frac{\rho \cdot A_r \cdot C_{N\alpha} \cdot (L_{CP} - L_{CG})^3}{8 \cdot I_L}} \tag{2.8-2}$$

and the term due to the X-axis side-to-side motion is

$$\zeta_{vxss} = \sqrt{\frac{\rho \cdot A_r \cdot C_{N\alpha}}{8} \cdot \frac{I_L}{m_o^2 \cdot (L_{CP} - L_{CG})}} \tag{2.8-3}$$

The total mass, m_o, the moment of inertia, I_L, and the distance between the center of gravity and the center of pressure, $(L_{CP} - L_{CG})$, all increase with increasing nose wait mass, which affects the damping ratios. Figure 2-31 shows how the term due to the X-axis side-to-side motion decreases faster than the uncoupled damping term as the nose cone weight mas increases, causing a net decrease in the total coupled damping ratio. The decrease in the term due to the X-axis side-to-side motion means that the rocket's ability to move side-to-side must decrease with increasing nose weight mass, resulting in the overall decrease in the coupled damping ratio.

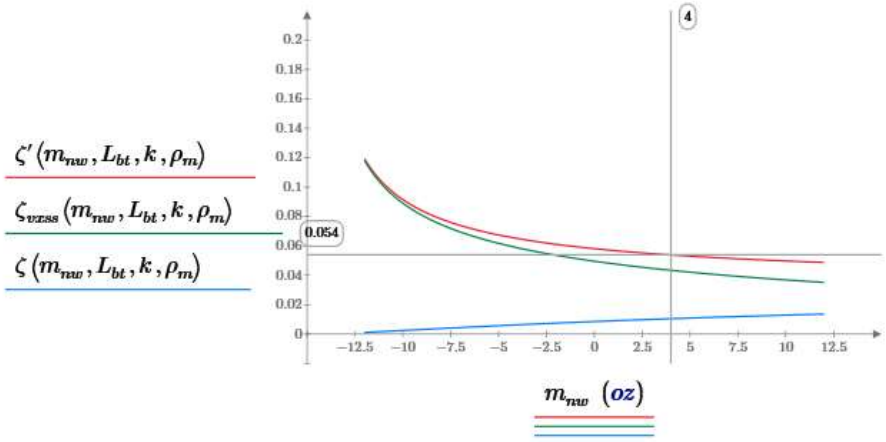

Figure 2-31 Component parts of the coupled damping ratio

Because the coupled rotational dynamics equation shows the rocket is more stable with a smaller distance between the center of gravity and the center of pressure, would it make sense to design the rocket with a minimum distance between the center of gravity and center of pressure? The center of gravity must still be ahead of the center of pressure throughout the flight. Once the center of gravity is behind the center of pressure, the rocket will be unstable, with a right half plane pole, and will attempt to rotate 180 degrees to an orientation where the center of gravity is once again ahead of the center of pressure. If this happens while the motor is still thrusting, the rocket will spin about its center of gravity. In an article in Sport Rocketry, "What Barrowman Left Out"[26], Robert Galejs showed that the center of pressure of a rocket moves forward with increasing angle of attack if the effect of the body tube lift is included in the center of pressure calculation. The center of pressure of a cylinder is the middle of the length of the cylinder. At 0 degrees angle of attack, the lift force is small compared to the lift of the fins and nosecone. But, as the angle of attack increases, the body tube lift force increases. The net force moves the center of pressure of the rocket forward. This effect is more pronounced the longer the rocket, as the center of pressure of the tube is farther forward. Galejs showed that the center of pressure can move forward up to 1 caliber at 20 degrees angle of attack for a typical model rocket configuration. Having a minimum margin of 1 caliber is still a good design target for most rockets, and even more for higher aspect ratio rockets, to ensure the center of pressure does not move ahead of the center of gravity with increasing angle of attack due to a large gust in wind velocity. But having a margin beyond what is necessary to ensure the center of pressure does not move ahead of the center of gravity does not lead to greater dynamic stability.

2.9 Rotational Dynamics Root Locus

The stability of the rotational system can be determined by the location of the roots of the denominator, or the poles, of the frequency domain gain equation (2.4-32), in the s-plane (see Sections 8.2, 8.4, and 8.5) . The s-plane is a plot of the imaginary portion of each pole on the y-axis versus the real portion of each pole on the x-axis. The length of the vector from the origin to the pole is the natural frequency, ω_n, of the system, and the cosine of the angle between the real axis and the pole is the damping ratio, ζ (see Figure 8-10). If the poles are plotted as a function of one of the rocket design parameters that affects the rocket's stability, such as the nosecone weight mass, the trajectory of the poles shows the impact of varying that parameter on the rotational stability. The trajectory of the poles as a function of a design parameter is called the root locus.

The sensitivity analyses in Section 2.8 does not show what happens to the rotational stability when the center of gravity moves behind the center of pressure. The root locus shows clearly what happens in this case as one of the poles moves into the right half of the s-plane (see Section 8). Any system with one or more poles that fall in the

[26] (Galejs, 1999)

right half plane will be unstable, meaning the output response to an impulse or step input will increase exponentially over time, whereas a system with just left half plane poles will be stable, meaning the output response to an impulse input will decrease over time. For a stable system, a system that takes longer to settle to zero is less stable than a system that takes shorter to settle to zero. The root locus method also clearly shows the difference in the behavior of the coupled and uncoupled rotational dynamics equations.

For the second order rotational equation (2.4-32)

.

$$\frac{\alpha_y}{v_w} = K_{\alpha y} \cdot \frac{1}{\frac{s^2}{(\omega_n')^2} + \frac{2 \cdot \zeta' \cdot s}{\omega_n'} + 1}$$

the roots, or poles of the equation are given by

$$p_1' = -\zeta \cdot \omega_n + \sqrt{\left(\zeta^2 - 1\right) \cdot \omega_n^{\,2}} \tag{2.9-1}$$

$$p_2' = -\zeta \cdot \omega_n - \sqrt{\left(\zeta^2 - 1\right) \cdot \omega_n^{\,2}} \tag{2.9-2}$$

Figure 2-32 shows a plot of the root locus of the coupled and uncoupled system for test rocket TR-1 as the nosecone weight is varied from -16 oz to 16 oz. The x-axis scale is $1/10^{th}$ the y-axis scale for both plots to show more clearly the changes in distance of the poles from the $j\omega$ axis. At the smallest value of nose weight mass, the poles start out on the real axis, one in the left half plane, and one in the right half plane, so the system is unstable. A real-axis pole pair with one in the right half plane has the same dynamics as an inverted pendulum where the system wants to rotate 180 degrees into a stable position. As the nose weight mass increases, the right half plane pole crosses into the left half plane for both systems, just as the stability margin equals zero at $m_{nw} = -14.5oz$, as shown in Figure 2-33. As the nose weight mass continues to increase, the poles meet and split into a complex conjugate pair and leave the real axis. The transition from a real axis pole pair, with one pole in the right half plane, to a complex pair in the left half plane occurs very rapidly with changing nose weight mass, occurring over a change of less than 0.1 oz. The further the poles are from the transition point, the slower they move with a change in the nose weight mass.

The root locus shows how the roots of the rotational equation go from being very stable to unstable with a very small change in a design parameter such as the nose weight mass. Because the transition from stable to unstable occurs very rapidly, the stability margin should never be allowed to approach zero.

In the coupled system, the poles meet at a larger initial negative real offset from the $j\omega$ axis, which makes the coupled system more stable than the uncoupled system with a very small margin between the center of pressure and canter of gravity. The poles then arc closer to the imaginary axis with increasing nose weight mass, which decreases

the damping ratio and the system stability as shown in Figure 2-27. In the uncoupled system, the poles start closer to the imaginary axis, then arc away from the imaginary axis with increasing nose wight mass, which increases the damping ratio and system stability. This agrees with the behavior of the sensitivity analysis shown in Figure 2-27.

Figure 2-34 shows the root locus as a function of varying the body tube length. Again, the roots start on the real axis, one in the left half plane and one in the right half plane. As the body tube length is increased, the poles move toward each other. The right half plane pole crosses the imaginary axis as the center of gravity moves ahead of the center of pressure and the poles meet and split to become a complex conjugate pair. For the uncoupled equation, the conjugate poles start out close to the imaginary axis and slowly arch away from the axis, and the system becomes more stable. For the coupled equation, the poles meet and leave the real axis further from the imaginary axis, making the system more stable than the uncoupled system. The poles then move toward the imaginary axis, so increasing body tube length further decreases the stability of the system.

Figure 2-35 shows the root locus as a function of varying the fin scaling factor. For both the coupled and uncoupled equations, the poles move further from the $j\omega$ axis with increasing fin size making both systems more stable.

Figure 2-36 shows the route locus as a function of varying the material density. Both the coupled and uncoupled equation roots start further from the $j\omega$ axis and move closer to it as the material density increases, and both systems become less stable with the increasing material density.

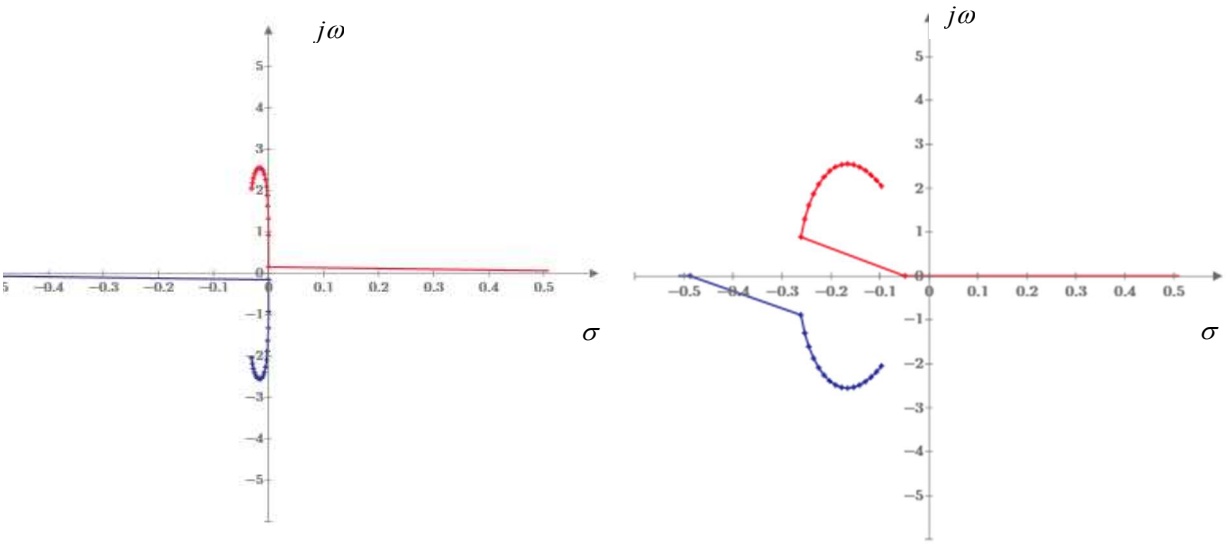

Uncoupled Equation Roots

Coupled Equation Roots

Figure 2-32 Root locus vs nose wight mass for $-16oz \le m_{nw} \le 16oz$

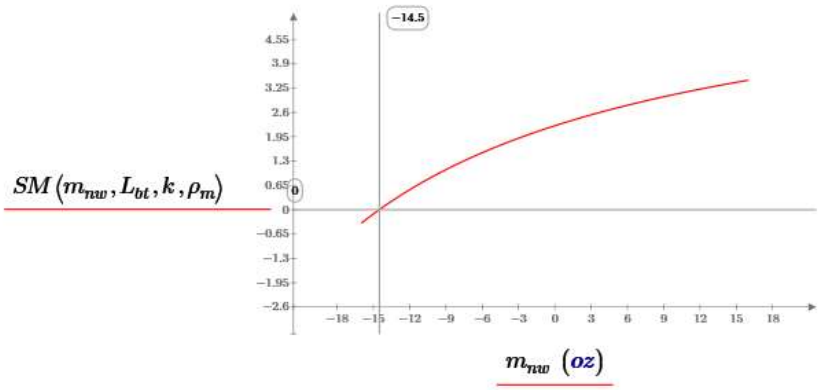

Figure 2-33 Stability margin vs. nose weight mass for TR-1

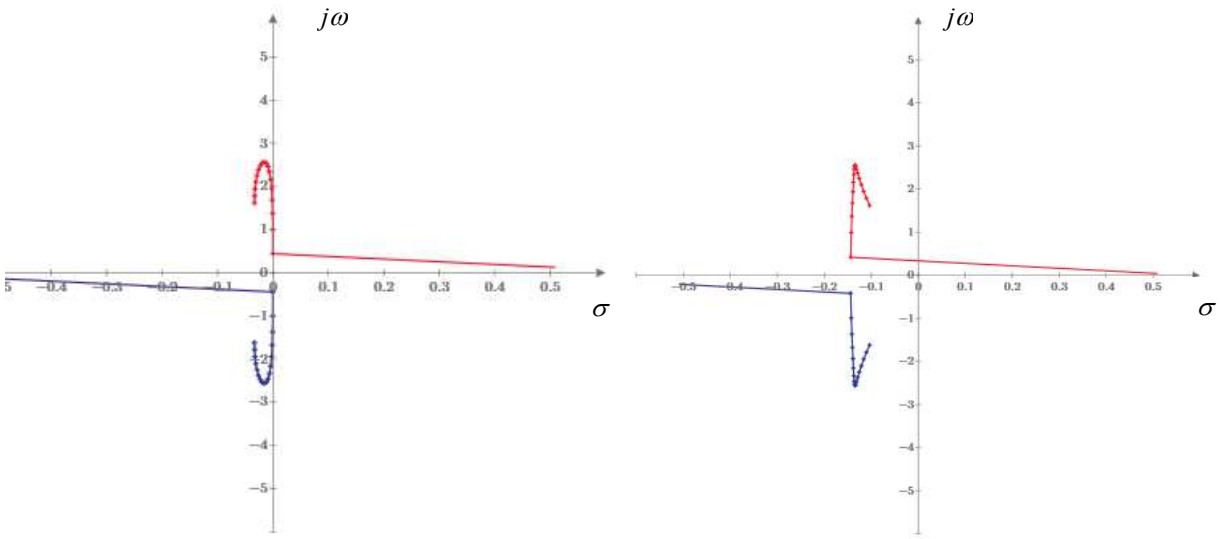

Uncoupled Equation Roots

Coupled Equation Roots

Figure 2-34 Root locus vs. body tube length for $0.5\,ft \le L_{bt} \le 4\,ft$

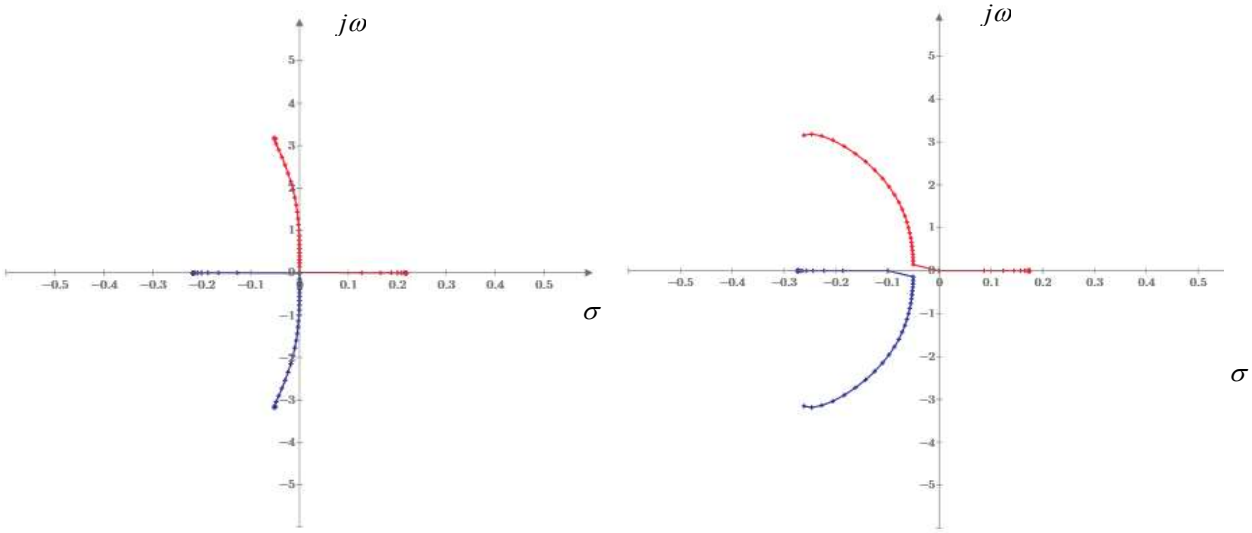

Uncoupled Equation Roots

Coupled Equation Roots

Figure 2-35 Root locus vs fin scaling factor for $0.5 \le k \le 2$

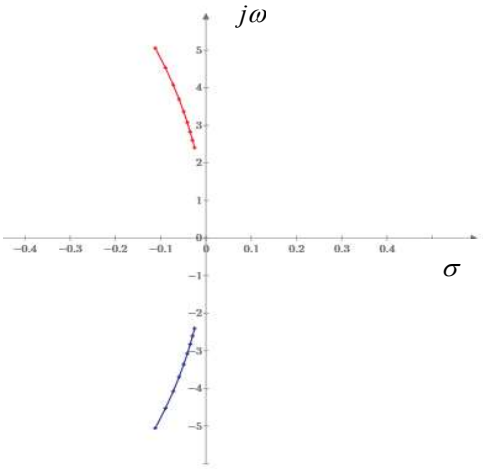

Coupled Equation Roots

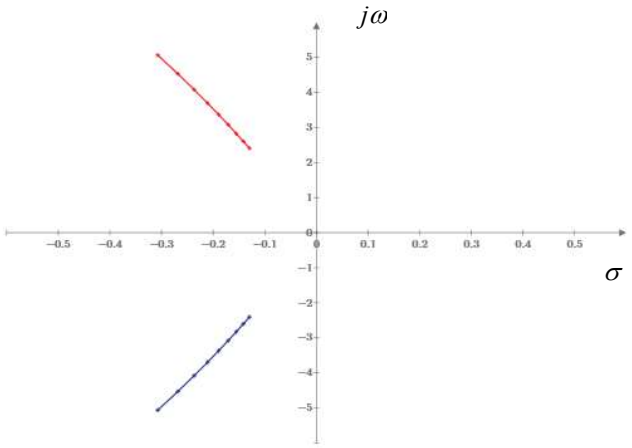

coupled Equation Roots

Figure 2-36 Root locus vs. material density for $1 \cdot oz/in^3 \geq \rho_m \geq 0.3 \cdot oz/in^3$ - note that the poles move toward the origin of the s-plane for increasing material density, opposite the direction of the other root locus plots for an increasing design parameter value

3 Flight Data

3.1 Test Rocket TR-1

Test rocket TR-1 was designed and built with the purpose of gathering flight data to test the models presented in this paper. The TR-1 design parameters needed for the flight model are given in Table 3-1.

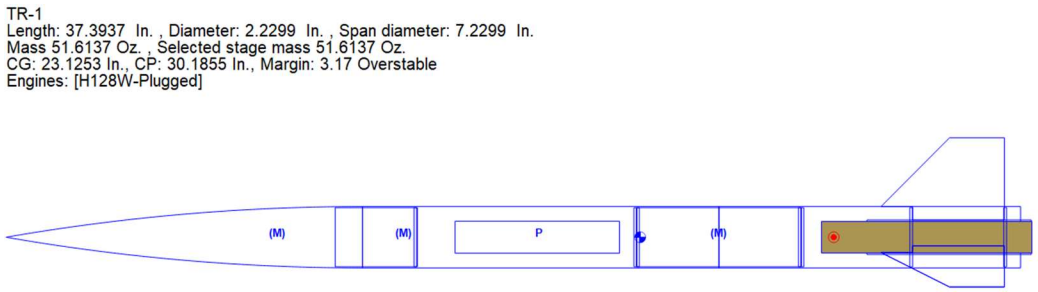

Figure 3-1 TR-1 test rocket

Rocket diameter	D_r = 2.27 in	Motor	AT-H128W
Nosecone length	L_{nc} = 13 in	Motor length	L_m = 7.25 in
Nosecone thickness	T_{nc} = .125 in	Motor mass	m_m = .454 lb.
Nosecone density	ρ_{nc} = 1.0 oz/in^3	Motor propellant mass	m_p = .207 lb.
Nose weight	m_{nw} = 4 oz	Motor burn time	t_b = 1.3 sec
Body tube length	L_{bt} = 24 in	Motor total impulse	I_t = 172.9 N sec
Fin root edge length	c_r = 4.5 in	Launch guide length	l_{lr} = 10 ft
Fin tip edge length	c_t = 2 in	Rocket total length	L_{ne} = 37 in
Fin span from body	s = 2.5 in	Rocket total mass	m_o = 3.21 lb.
Fin mid cord sweep ang	Γ_c = 26.6 deg	Center of gravity	L_{CG} = 22.89 in
Fin thickness	T_f = .15 in	Center of pressure	L_{CP} = 28.4 in
Fin density	ρ_f = 1.0 oz/in^3	Stability Margin	SM = 2.42

Number of fins	$N = 3$	Rocket moment of inertia	$I_L = 3.071$ lb ft^2
Motor tube length	$L_{mt} = 6$ in	Rocket drag coefficient	$C_D = .8$
Motor tube diameter	$D_{mt} = 1.269$ in	Normal force coefficient	$C_{N\alpha} = 10.2$
Motor tube thickness	$T_{mt} = .062$ in	Rocket lift coefficient	$C_{L\alpha} = 10.2$
Motor tube density	$\rho_{mt} = 1.0$ oz/in^3	Natural frequency	$\omega_n = 0.49$ Hz @ 50.9 mph
Motor mount length	$L_{mm} = 0.188$ in	Natural frequency	$\omega_n = 1.05$ Hz @ 110 mph
MM density	$\rho_{pw} = 1.0$ oz/in^3	Natural frequency	$\omega_n = 2.24$ Hz @ 227 mph
Parachute/ebay mass	$m_{par} = 16.7$ oz	Uncoupled damping ratio	$\zeta = 0.0105$
Parachute length	$L_{par} = 4$ in	Coupled damping ratio	$\zeta' = 0.0539$

Table 3-1 TR-1 model parameters

The purpose of the flight instrumentation was to measure the rocket's rotation about its three axes and its side-to-side motion to validate the rotational dynamic stability model. The rotation rate and acceleration of the rocket was measured using an RAF Datalogger[27]. The Datalogger has two 3-axis accelerometers and one 3-axis rate gyroscope. The Datalogger logs the data to an onboard micro-SD card which is downloaded into a Mathcad worksheet or an Excel spreadsheet where it is analyzed, and the flight graphs are generated. The data sample rate for the Datalogger is 0.75 ms, but the data is decimated to a 7.5 ms sample rate using a Python script to reduce computation times before loading into a Mathcad worksheet for analysis.

Figure 3-2 RAF Datalogger

[27] (Feretich, 2015-2018)

Since the Datalogger measures the rotational rate of the rocket's three axes in the rocket frame of reference, the orientation of the rocket in the ground-based frame of reference must be determined by doing a frame of reference axis translation using Euler's angles, as covered in Section 9. This is done as a part of the post flight data analysis.

The TR-1 electronics bay, which contains an Altus Metrum Easy Mini barometric deployment altimeter and the RAF Datalogger, is located rearward in the rocket, just ahead of the motor, to locate the accelerometers as close to the rocket's center of gravity as possible.

A Beeline GPS is flown in the nosecone compartment.

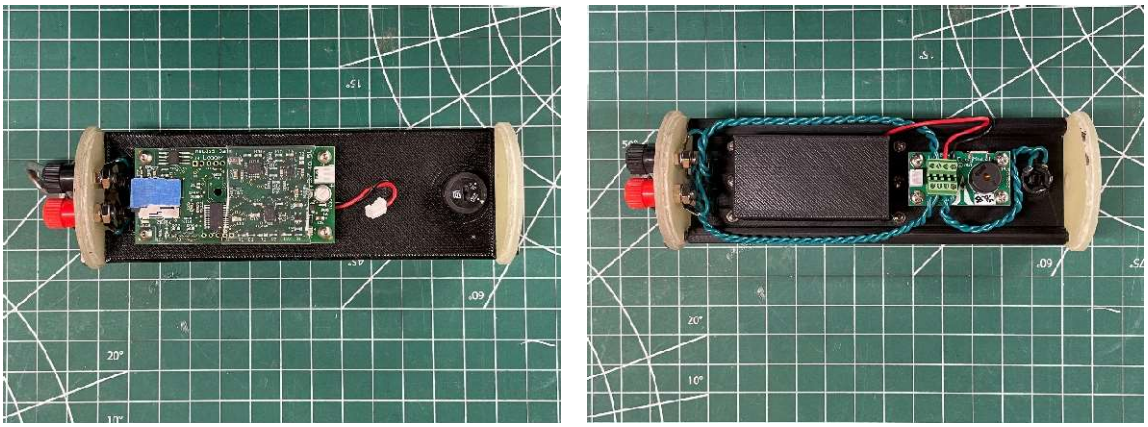

Figure 3-3 TR-1 electronics bay with RAF Datalogger (left) and Altus Metrum EasyMini (left)

The rate gyroscope will see the same angular rotation about each of its axes no matter where it is located along the rocket's length. But the acceleration the accelerometer sees is impacted by its location along the length of the rocket. The accelerometer will measure the acceleration due to thrust, gravity, drag, and any side-to-side motion of the rocket. The side-to-side motion will be a combination of any side-to-side motion of the center of gravity of the rocket plus the side-to-side motion due to the rocket's rotation about its x or y-axes if the accelerometer is located some distance from the center of gravity rotation point. To measure just the side-to-side motion of the center of gravity, any acceleration component due to the rotational arc must be subtracted from the total acceleration. This is possible by using the rate gyroscope to determine the rocket's rotation, along with knowing the distance between center of gravity and the accelerometer's location. But there is always a potential source of error in making the measurements for the correction, so it is better to minimize the rotational motion by placing the accelerometer as close as possible to the center of gravity to eliminate rotational arc acceleration component. In TR-1, the accelerometer is close enough to the center of gravity that the rotational component of the lateral acceleration can be neglected.

3.2 TR-1 Flight Data

The flight of TR-1 that will be analyzed in detail below occurred on October 15, 2022, at Tripoli Central's October Skies launch at the Maddox Dairy in Helm, California.

Figure 3-4 October 15, 2022, flight of TR-1 at October Skies

The flight data consists of the Altus Metrum barometric altitude data and the RAF Datalogger accelerometer and rate gyroscope data. The Beeline GPS was not flown on this flight.

Figure 3-5 shows the altitude profile for the flight from the Altus Metrum altimeter data. The winds were relatively calm at 5 mph with gusts to 10 mph at ground level, and the rocket went nearly vertically, although the slight turn into the wind was noticeable as the rocket left the launch rail. Apogee is 1,606 feet at 9.38 seconds.

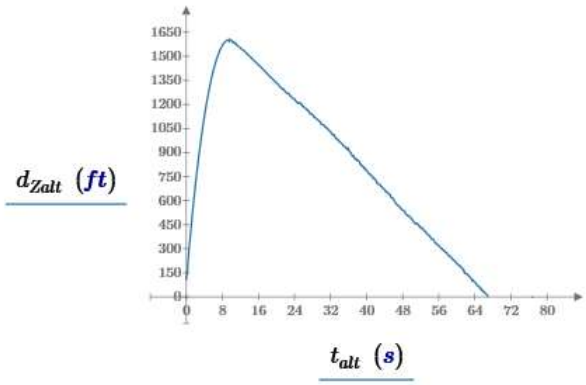

Figure 3-5 Altus Metrum barometric altitude profile

Figure 3-6 shows the raw rotational rate and acceleration data from the RAF Datalogger. The following analyses are all based on this data.

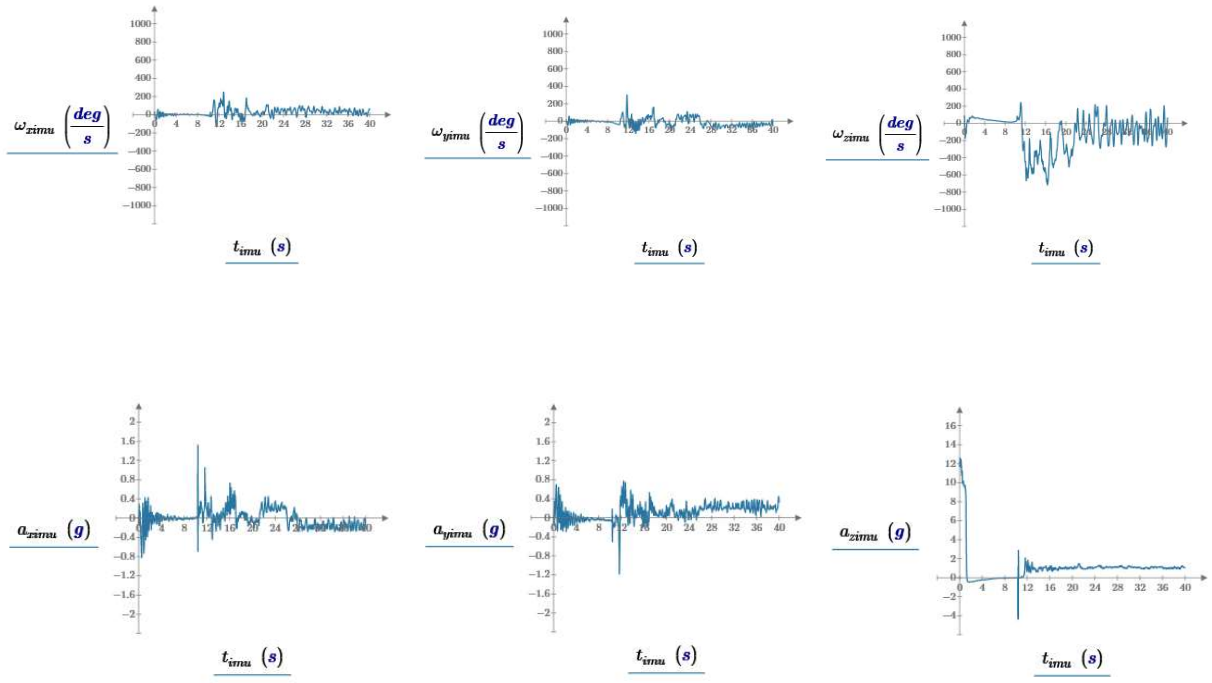

Figure 3-6 Raw rotational rate and acceleration data for the rocket's x, y, and z-axes

Although Euler's angles by themselves do not provide useful information about the rotational dynamics, they allow for mapping parameters between the rocket x-y-z frame of reference and the ground X-Y-Z inertial frame of reference. They are calculated from the x-y-z rotation rate data using equations (9.1-5) and are shown in Figure 3-7.

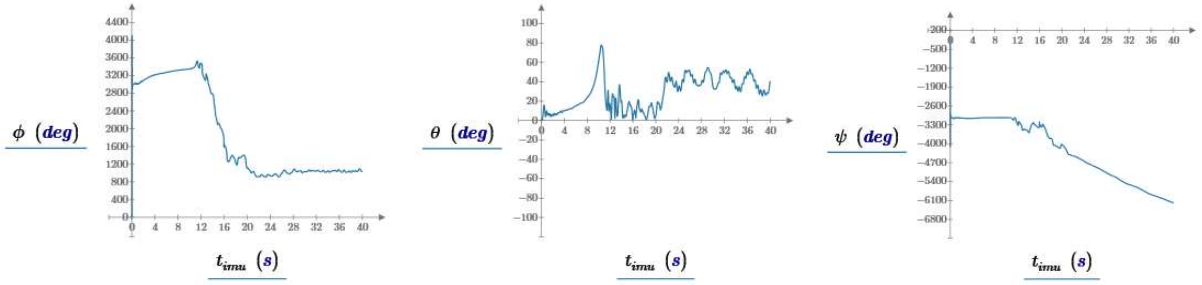

Figure 3-7 Euler's angles calculated form the rate gyroscope data

To find the acceleration of the rocket along its z-axis, the raw z-axis acceleration data must be corrected for the constant 1 g field due to gravity. Gravity is aligned with the ground frame-of-reference Z-axis, so the z component of the Z-axis unit vector is the portion of 1 g to subtract from the z-axis acceleration measured data. The Z-axis unit vector, shown in Figure 3-8, is calculated from (3.2-1) and Euler's angles equation. The notation U_{Zz} means the component of the Z-axis unit vector aligned in the direction of the z-axis. The z-axis of the rocket starts out aligned with the Z-axis but moves away from alignment as the rocket tilts into the wind. The rocket continues to rotate as it approaches apogee. The parachute deploys from the front end of the rocket which orients the accelerometer in the same direction it was oriented during the upward portion of the flight. 20 seconds into the flight, the rocket starts swinging under the parachute at a slight angle from vertical.

$$U_{Zz} = z_{Euler}(0,0,1) = \cos\theta \tag{3.2-1}$$

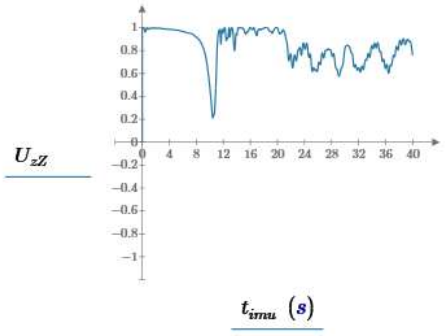

Figure 3-8 z component of the Z-axis unit vector

The gravitationally corrected z-axis acceleration and velocity are calculated by

$$a_{zcimu} = a_{zimu} - g \cdot U_{Zz} \tag{3.2-2}$$

$$v_{zcimu} = v_{zcimu} + a_{zcimu} \cdot \Delta t_{imu} \tag{3.2-3}$$

and shown in Figure 3-9. Once corrected for the gravitational field, the graph shows the acceleration ranged from 11.5 g's to 8.5 g's during thrust, then the rocket deaccelerated at a little more than -1 g due to a combination of gravity and drag during coast, approaching -1 g as the rocket slowed. Once the parachute deploys, the rocket has a constant velocity, so the acceleration stays at an average of 0 g's. At 20 seconds, the acceleration starts to show a net positive value due to the rocket's swinging under the parachute, producing a slight centrifugal acceleration. During recovery, the Datalogger faces forward, the same orientation as it is in flight, so the acceleration due to swinging is in a positive direction.

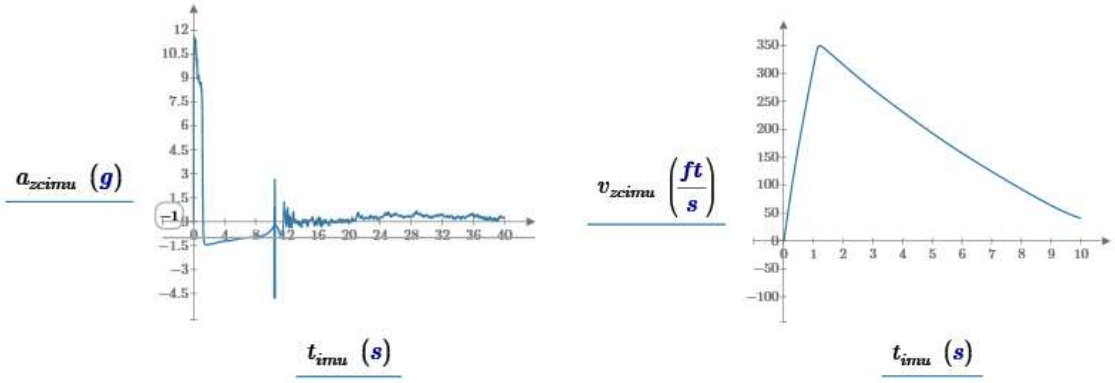

Figure 3-9 z-axis acceleration and velocity corrected for 1 g gravitational field

The polar angles are calculated from the z-axis unit vectors and shown in Figure 3-10. Θ, the polar angle from vertical, is the three-dimensional proxy for α_y, the orientation angle of the rocket from vertical in the 2-dimensional model. For this flight, the rocket rotated approximately 8 degrees as it left the launch rail, with a large initial overshoot in the step response, and the step response oscillations dampened over the next several seconds. The oscillation frequency starts around 3 Hz and slows as the rocket slows. Γ, the polar projection of the rocket's z-axis onto the XY plane, shows the rotation of the rocket's flight path projected onto the ground is constant at around 105 degrees. This indicates that the rocket flew in a 2-dimensional plane.

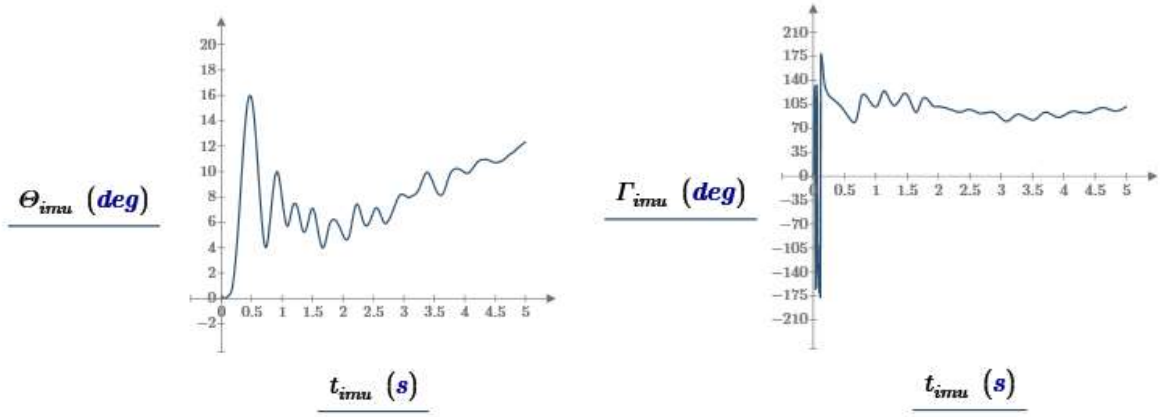

Figure 3-10 Polar angle s for the z-axis of the rocket in the ground (X-Y-Z) frame of reference

Figure 3-11 shows the spin rate and total angle of rotation about the rocket's z-axis. This shows that over the entire 10 seconds of the upward fight, the rocket rotates just one revolution. With minimal z-axis spin and the rocket's flight path falling along a two-dimensional plane, the two-dimensional model is valid for this fight.

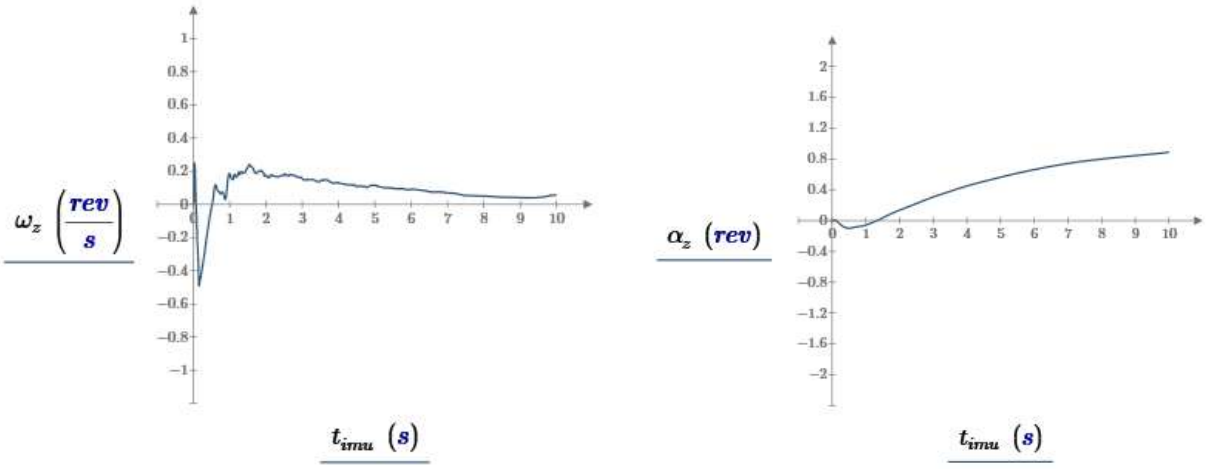

Figure 3-11 z-axis spin rate and rotational angle

The location of the tip of the nose cone in the ground-based frame of reference shows the rockets attitude, and is given by the z- axis unit vector from equations (9.1-6). Plotting U_{zY} vs. U_{zX} in Figure 3-12 shows the trajectory of the tip of the nose cone in three dimensions projected onto the XY plane and viewed from above. On this graph, negative Y, north, is up and negative X, east, is to the right. After the initial turn into the wind toward the southeast, the rocket tip travels several times in a tight circle before starting to arc over at the end of the coast phase.

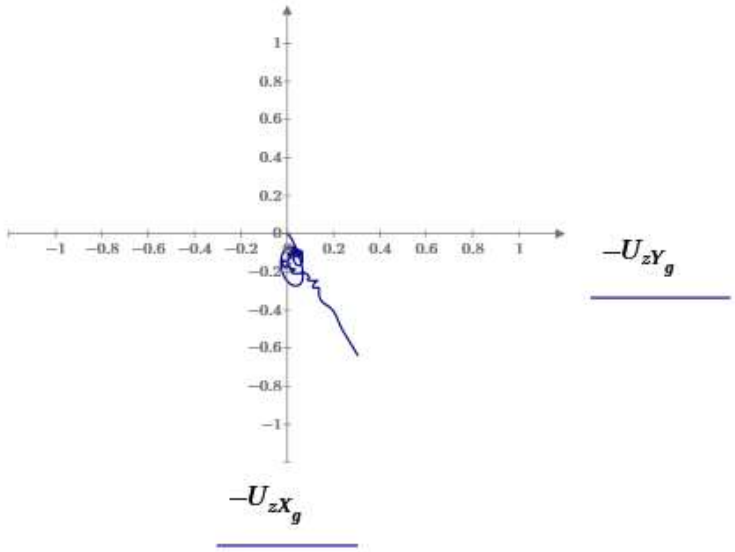

Figure 3-12 The projection of the motion of the tip of the nose cone onto the XY plane

The two key flight parameters needed to verify the model are the angle of the rocket from vertical and the side-to-side motion of the rocket along the ground-based frame of reference XY-axes plane. Figure 3-13 shows the measured rocket rotation angle, Θ, from Figure 3-10 (blue trace), and the rocket rotation angle, α_y, from the complete model, that was shown in Figure 2-2 (red trace). The modeled wind velocity is 10 mph which leads to an 8-degree rotational step. The initial overshoot of the measured response is larger than the modeled response and the ringing is a little higher in frequency, but the magnitude of the subsequent ringing and the decay time is similar for both. Overall, there is a close match between the modeled and measured response to the step in the wind velocity as the rocket leaves the launch guide. Also note that there is not a significant decrease in the damping after motor burnout at 1.3 seconds. This confirms that jet damping is not a significant contributor to the overall rotational damping.

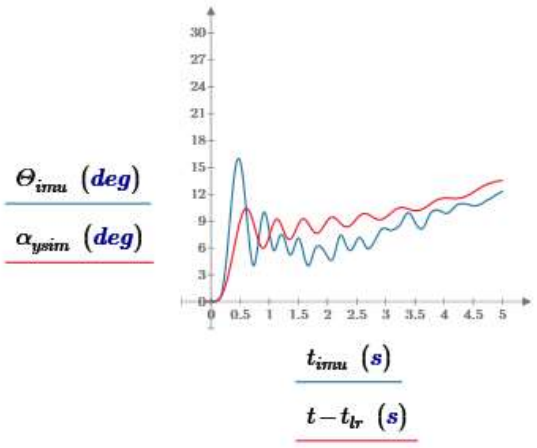

Figure 3-13 Measured (blue trace) and modeled (red trace) rocket rotation angles

3.3 Analysis of the Side-to-Side Motion of the Rocket

The first step to calculating the side-to-side motion of the rocket is to translate the accelerometer measurements along the rocket's x, y, and z-axes to the X and Y-axes of the ground-based frame of reference using Euler's equations (9.1-1).

$$a_{Ximu} = X_{Euler}(a_x, a_y, a_z) \tag{3.3-1}$$

$$a_{Yimu} = Y_{Euler}(a_x, a_y, a_z) \tag{3.3-2}$$

The velocities along the X and Y-axes are then found by doing a discrete time integration of the acceleration data. The result is shown in Figure 3-14.

$$v_{Ximu} = v_{Ximu} + a_{Ximu} \cdot \Delta t_{imu} \tag{3.3-3}$$

$$v_{Yimu} = v_{Yimu} + a_{Yimu} \cdot \Delta t_{imu} \tag{3.3-4}$$

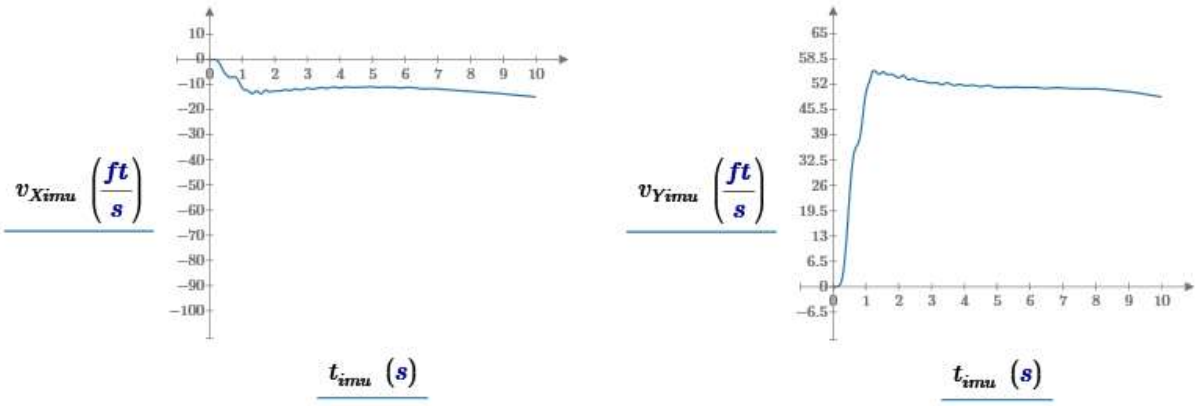

Figure 3-14 The velocity of the rocket along the ground-based frame of reference X and Y-axes

From Figure 3-10 and Figure 3-12, the rocket moves in a south-southeasterly direction at a polar angle of 105 degrees roughly along a straight line. That is the plane that will be used for the 2-D analysis of the side-to-side motion of the rocket. The velocities along the X and the Y-axes are combined to form the total velocity of the rocket along the XY plane. The result is shown in Figure 3-15. The result looks similar to the modeled X-axis velocity shown in Figure 2-7.

$$v_{XYimu} = \sqrt{v_{Ximu}{}^2 + v_{Yimu}{}^2} \tag{3.3-5}$$

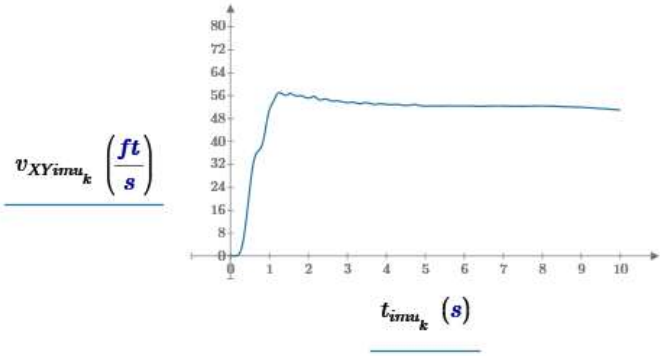

Figure 3-15 Total velocity of the rocket along the XY plane

To determine the small side-to-side motion of the rocket along the X-axis in the model, the X-axis equation of motion with just the lift force, equation (2.3-1), was solved simultaneously with the other flight model equations. It is not possible to use that method for the measured data, so a polynomial curve fit is used instead to establish the general trend of the velocity, which is then subtracted from the data, leaving just the small side-to-side velocity component. The polyfitc function in Mathcad was used to create a 6th order polynomial for the boost phase, and a

separate polynomial for the coast phase. The higher the order of the polynomial, the higher the frequency of the data the polynomial will fit. 6th order appears to be a good compromise between fitting the general trend of the X-axis motion, while not tracking the magnitude of the small side-to-side oscillation. Figure 3-16 shows the 6th order polynomial curve fit. Figure 3-17 shows the result of subtracting the polynomials from the velocity data. The discontinuity at motor burnout is due to the use of two separate curve fits that meet at that location.

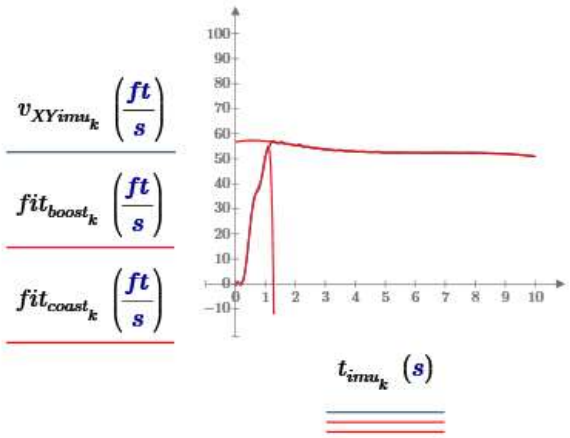

Figure 3-16 6th order polynomial curve fit to v_{XY} boost anc coast phase data

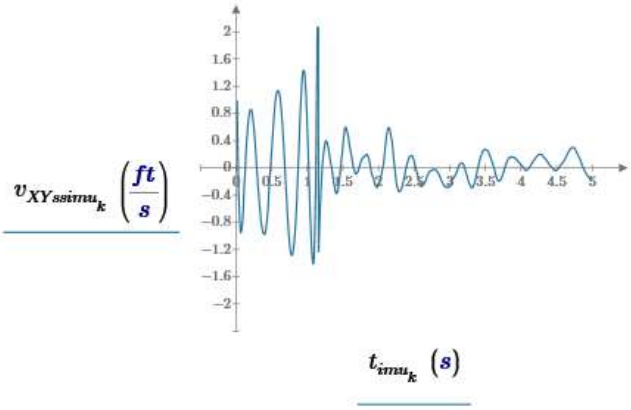

Figure 3-17 Side-to-side motion of the rocket in the XY plane

The side-to-side distance the rocket travels is calculated by integrating the side-to-side velocity, v_{XY}. The distance the center of pressure the rocket travels as it rotates is calculated by multiplying the polar angle of rotation by the distance from the center of gravity to the center of pressure of the rocket.

$$d_{XYssimu} = d_{XYssimu} + v_{XYssimu} \cdot \Delta t_{imu} \tag{3.3-6}$$

$$d_{\Theta imu} = -(L_{CP} - L_{CG}) \cdot \Theta_{imu} \tag{3.3-7}$$

Figure 3-18 shows the measured values of the side-to-side motion (red traces) and the motion due to the rotation (blue traces) on the left and the output from the model on the right. The measured values are in phase as are the modeled values. The step in the measured d_{XY} data was removed by the curve fit, leaving just the sinusoidal component. Except for the slightly higher frequency of oscillation in the measured data, the modeled and measured results are similar, validating the model's prediction of the side-to-side motion of the rocket that contributes to the rocket's overall rotational stability.

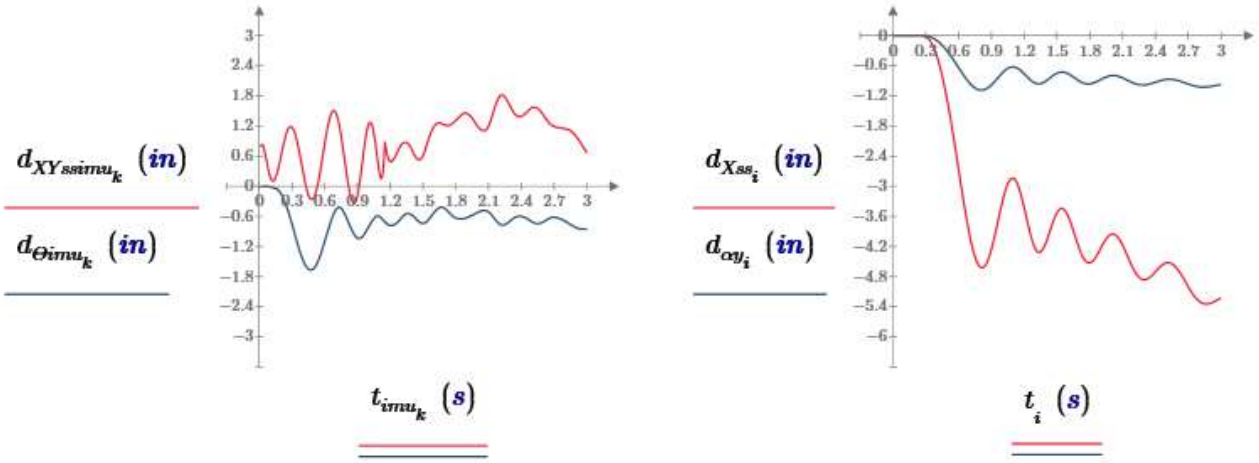

Figure 3-18 Measured and modeled results for the side-to-side motion of the rocket - The red trace is the X-axis side-to-side motion and blue trace is the tangential rotational motion

4 Results, Conclusions, and Next Steps

4.1 Results Summary

Sections 2.1 - 2.3

- The complete flight model predicts that the rocket is much more stable than the rotational equation alone predicts
- It is the lift force and resulting X-axis side-to-side motion that couples to the rotational equation through that equation's driving function, α_T and provides the increased rotational stability
- The X-axis side-to-side motion was isolated from the overall X-axis motion using a separate X-axis equation with just the X-axis lift force solved simultaneously with the rest of the equations in the model
- The phase of the side-to-side velocity, v_{Xss}, aligns with the phase of the tangential rotational velocity and its magnitude is greater than the magnitude of the tangential rotational velocity, leading to the greater rotational stability
- The gain seen by the side-to-side velocity is the same as the gain seen by the tangential rotational velocity when referenced to the center of pressure,
- The side-to-side velocity adds to the damping term of the rotational dynamic equation by increasing the effective angle of attack of the damping term
- The X-axis side-to-side motion continues after motor burnout because the motion is due to the lift force, so the enhanced damping also continues after motor burnout
- The side-to-side motion is caused by the X-axis lift due to the rotational angle of attack

Section 2.4 - 2.5

- A linearized second order rotational dynamic stability equation (coupled equation) that includes the effects of the X-axis side-to-side motion was derived and shown to agree with the rotation predicted by the complete model
- The magnitude of the coupled natural frequency is nearly the same as the uncoupled natural frequency and both are a function of the velocity of the rocket
- The coupled damping ratio is much larger than the uncoupled damping ratio and indicates stability that agrees with the stability predicted by the full simulation, and like the uncoupled damping ratio, is independent of the rocket velocity

Section 2.6

- A linearized coupled second order differential equation for the X-axis side-to-side motion was derived and shown to agree with the motion predicted by the complete model

- The magnitude of the peak side-to-side velocity was shown to increase with increasing rotational stability, but the natural frequency and damping ratio are the same as the coupled rotational parameters

Section 2.7

- It was shown that the gain of the rotational frequency response decreases with increasing rocket velocity, while the bandwidth increases with increasing velocity - overall, the sensitivity to wind perturbations decreases with increasing velocity

Section 2.8

- Sensitivity analyses showed the dependence of rotational stability parameters on key rocket design parameters
- The coupled damping ratio is always larger than the uncoupled damping ratio and moves in the opposite direction for many rocket design parameters.
- An increasing stability margin (distance between the center of pressure and center of gravity) does not always correlate to an increasing coupled damping ratio and rotational stability
- A rocket can become less stable with increasing stability margin (the distance between the center of pressure and the center of gravity) if the parameter that causes the increase in the stability margin also reduces the ability of the rocket to move side-to-side along the X-axis

Section 2.9

- Root locus was shown to be another technique for visualizing the rotational stability's dependence on key design parameters and clearly shows how the rotational dynamics change rapidly as the center of pressure crosses through the center of gravity

Section 3.2-3.3

- The rotational dynamics predicted by the complete flight model agrees with measured flight data
- The x-axis side-to-side motion was found in the accelerometer flight data and matched the model's predictions – finding the side-to-side motion in the measured accelerometer data was key to validating the coupled stability model

4.2 Conclusions

A rocket is more stable than predicted by Mandell's rotational equation alone because of the side-to-side motion of the rocket. That motion is due to the cross coupling between the rotational equation and the X-axis equation of motion through the lift force term. The lift causes the side-to-side motion in the rocket's flight path that has the effect of increasing the angle of attack of the rotational damping term which increases the magnitude of the damping of the rocket's rotation. The side-to-side motion is larger (4 times in the case of TR-1) than the tangential rotational motion, leading to greater stability. If the rocket's side-to-side motion is constrained, for example by a gimbal that just allows the rocket to rotate, then the uncoupled rotational dynamics equation alone would describe the rocket's

rotational dynamics. The coupled damping ratio is not directly proportional to the difference between the center of pressure and center of gravity, so the traditional stability margin is not a good indicator of a rocket's rotational dynamic stability.

4.3 Next Steps

- Further validate the coupled rotational dynamics model by collecting flight data from a wider variety of rocket configurations

- Look for a new "rule-of-thumb" guideline for the stability margin that takes into consideration both the movement in the center of pressure with angle of attack and the coupled damping ratio. Currently, the guideline is based on the distance between the center of pressure and the center of gravity in body tube diameters. Is there a better parameter to use for the guideline that ensures the center of pressure always remains behind the center of gravity for longer aspect ratio rockets at higher angles of attack but does not give a value larger than required for shorter aspect ratio rockets?

- Extend the dynamic stability model to three dimensions. Many of the rotational measurements made on flights of rockets larger than test rocket TR-1 (not presented here) show a rapid spin-up of the rocket, up to 4 revolution per second, lasting for 1-2 seconds near motor burnout, probably due to off-axis thrust near motor burn-out. This rapid spin results in a rotational oscillation in the rocket's two lateral axes called coning. To analyze the cause of the sustained spin-coupled oscillations, the dynamic stability model would need to be extended from 2 to 3-dimensions and include the cross-axis coupling terms. Mandell's work covered spin induced instability, but without the benefit of actual flight data.

5 Tools, Equipment, Facilities, & Budget

Software

- Mathcad was the main tool used on this project for modeling, numerical analysis, symbolic analyses, measurement data analysis, and data graphing.
- RockSim was used to validate the parameters calculated by the model such as moment of inertia and center of pressure.
- Microsoft Office Word was used to write this paper
- MathType embedded app for Office was used to create the equations in MS Word
- TurboCAD was used to create most of the figures other than graphs and create the test rocket eBay sled design
- PowerPoint was used to create some figures
- Python and the VPython graphics library were used to create the rotational and side-to-side motion flight graphic using data from the Mathcad simulation. A real time flight animation was also created in Python.

Hardware

- The RAF Data Logger was used to measure the rocket's 3-D acceleration and axis rotations
- A Beeline GPS was used to get flight path data and validate the wind speed at the flight time for comparing the model simulation to the measured rotational response
- Test rocket TR-1 was built from standard off-the-shelf fiberglass parts from Mad Cow Rocketry
- A Dremel 3D45 3D printer was used to print the test rocket ebay sled

Facilities

- All computer work was done in the authors home office
- Test rocket TR-1 was built in the author's home woodworking and miscellaneous projects shop
- All test flights were done at Tripoli Central's launch site at the Maddox Dairy in Helm California

Expenses for Test Rocket TR-1

Description	Vendor	Total
2.2” Nose Cone	Mad Cow Rocketry	40.00
2.2” Body tube – 48”	Mad Cow Rocketry	72.00
Three Fins	Mad Cow Rocketry	15.00
1.1” Motor Tube	Mad Cow Rocketry	11.00
eBay Coupler Tube	Mad Cow Rocketry	17.00
29 mm Motor Retainer	Mad Cow Rocketry	23.00
Four 2.2” Bulk Plates	Mad Cow Rocketry	28.00
Two 29 mm to 54 mm Centering Rings	Mad Cow Rocketry	18.00
Misc Hardware	McMaster-Carr	10.00
Altus Metrum EasyMini Altimeter	Altus Metrum	80.00
RAF Data Logger	RAF Systems	120.00
Three AT H128W motors	Aerotech	105.00
Total		**539.00**

6 Appendix 1 – 3-D Flight Model

This is the set of equations that is the starting point for a 3-dimensional flight trajectory and rotational dynamics model. The 2-dimensional model is a subset of this model. Newton's law for the position of the CG in the inertial (ground) frame of reference

$$m_o \frac{d^2 d_X}{dt^2} = F_{TX} + F_{DX} + F_{LX} \tag{6.1-1}$$

$$m_o \frac{d^2 d_Y}{dt} = F_{TY} + F_{DY} + F_{LY} \tag{6.1-2}$$

$$m_o \frac{d^2 d_Z}{dt^2} = F_{TZ} + F_{DZ} + F_{LZ} - m_o g \tag{6.1-3}$$

Euler's dynamic equations for the rotation about the CG in the rocket frame of reference. Symmetry eliminates the z-axis coupling with the x and y-axes ($\left(I_L - I_L\right) = 0$

$$I_L \frac{d^2 \alpha_x}{dt^2} = M_{2x} + M_{2Rx} + M_{1x} + (I_L - I_R) \cdot \frac{d\alpha_y}{dt} \cdot \frac{d\alpha_z}{dt} \tag{6.1-4}$$

$$I_L \frac{d^2 \alpha_y}{dt^2} = M_{2y} + M_{2Ry} + M_{1y} + (I_R - I_L) \cdot \frac{d\alpha_x}{dt} \cdot \frac{d\alpha_z}{dt} \tag{6.1-5}$$

$$I_R \frac{d^2 \alpha_z}{dt^2} = M_{2z} + M_{1z} \tag{6.1-6}$$

Euler's angles for translation from the rocket frame of reference to the inertial (ground) frame of reference. These angel rate equations were derived using the method shown in Thomson[28] , but using the order of rotation convention from Sidi[29]

$$\frac{d\phi}{dt} = \omega_x + \frac{\sin\theta \sin\phi}{\cos\theta} \cdot \omega_y + \frac{\cos\phi \sin\theta}{\cos\theta} \cdot \omega_z \tag{6.1-7}$$

$$\frac{d\theta}{dt} = \cos\phi \cdot \omega_y - \sin\phi \cdot \omega_z \tag{6.1-8}$$

$$\frac{d\psi}{dt} = \frac{\sin\phi}{\cos\theta} \cdot \omega_y + \frac{\cos\phi}{\cos\theta} \cdot \omega_z \tag{6.1-9}$$

[28] (Thomson, 1986, p. 38)

[29] (Sidi, 2002, p. Appendix A)

7 Appendix 2 – 2-D Flight Model

Figure 7-1 shows the 2-dimensional, 3 degree-of-freedom model. X and Z are used to denote the fixed ground frame axes, rather than X and Y, to be consistent with the conventions that are used in the 6 degree-of-freedom model where Z is the vertical axis. In this system, the Y axis is coming out of the plane of the figure. An angle of rotation is denoted by the axis about which the object rotates. Since the rocket frame of reference axes, x, y, and z, start out aligned with the ground-based frame of reference axes, X, Y, and Z, in the three-dimensional model, the rocket, in the two-dimensional model, rotates about its y-axis. In the two-dimensional model, the rocket's y-axis always remains orthogonal to the plane of the ground XZ-axes and aligned with the Y-axis. To be consistent with the 6 degree-of-freedom model, the y-axis will be used as the axis of rotation of the rocket, even though the y-axis is not shown explicitly in the 2-dimensional drawings. The direction of rotation about the y-axis shown in Figure 7-1 indicates the positive direction for a right-handed coordinate system where the positive y-axis comes out of the drawing.

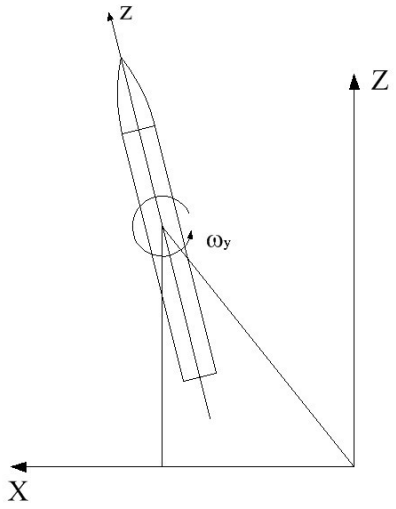

Figure 7-1 Model for 3-degrees of freedom

There are three second order differential equations of motion that must be solved simultaneously to determine the trajectory and orientation of a rocket in flight in the 2-dimensional model. The first two equations describe the motion of the center of gravity of the rocket along the X and Z-axes in the ground-based frame of reference and the last one describes the rotation about the y-axis in the rocket frame of reference. In the 2-dimensional system, the translation from the rocket frame of reference to the inertial ground frame of reference is just the rotational angle of the rocket, α_y, so no additional axis translation equations are required.

$$m_o \frac{d^2 d_X}{dt^2} = F_{TX} + F_{DX} + F_{LX} \tag{7.1-1}$$

$$m_o \frac{d^2 d_Z}{dt^2} = F_{TZ} + F_{DZ} + F_{LZ} - m_o g \tag{7.1-2}$$

$$I_L \frac{d^2 \alpha_y}{dt^2} = M_{2y} + M_{2R} + M_{1y} \tag{7.1-3}$$

Each second order differential equation can be written in terms of two first order differential equations. This is the convention used by a state variable system which defines the state variables in terms of first order differential equations. The state variable convention is used here to be consistent with the form used by Mathcad for solving nonlinear simultaneous differential equations numerically.

$$\frac{dd_X}{dt} = v_X \tag{7.1-4}$$

$$m_o \frac{dv_X}{dt} = F_{TX} + F_{DX} + F_{LX} \tag{7.1-5}$$

$$\frac{dd_Z}{dt} = v_Z \tag{7.1-6}$$

$$m_o \frac{dv_Z}{dt} = F_{TZ} + F_{DZ} + F_{LZ} - m_o g \tag{7.1-7}$$

$$\frac{d\alpha_y}{dt} = \omega_y \tag{7.1-8}$$

$$I_L \frac{d\omega_y}{dt} = M_{2y} + M_{2R} + M_{1y} \tag{7.1-9}$$

These six differential equations will be used to solve for the six state variables as a function of time. The six variables are $d_X, v_X, d_Z, v_Z, \alpha_y,$ and ω_y. They describe the rocket's location and rotational angle in 2-dimensional space, as well as its velocity and rate of angular rotation. These six variables are referred to as the state variables of the system because they are the minimum number of variables needed to completely describe the state of the system at any instant in time. Once the state variables are determined, all other parameters of interest can be found from the state variables using algebraic equations that are functions of the state variables. All parameters in the model are written as functions of these six variables, plus the two inputs to the model, the motor thrust and the wind velocity.

Because the state variables are all functions of time or frequency, it is common, to use the nomenclature $\alpha_y(t)$ in the time domain equations, and $\alpha_y(s)$ in the frequency domain equations when writing the state variable α_y. This paper will simply use the nomenclature α_y to keep the equations simpler and easier to read, and the context of the equation to determine whether the variable is a time or frequency domain variable.

The key velocity vectors and angles used by the model are shown in Figure 7-2. Figure 7-3 shows the velocity relationships in more detail. The model assumes that the wind that causes the rocket to rotate is approaching from the -X (westerly) direction. The rocket rotates into the upper left-hand quadrant as a result. v_T is the velocity of the total oncoming airstream.

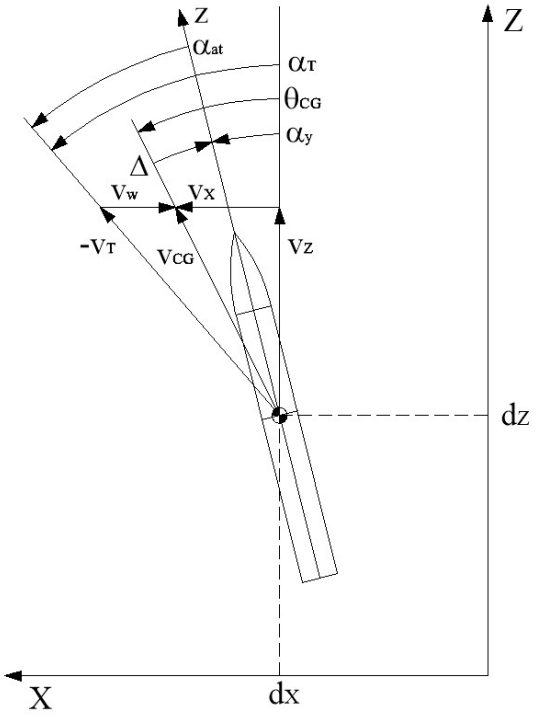

Figure 7-2 Key rotational angles

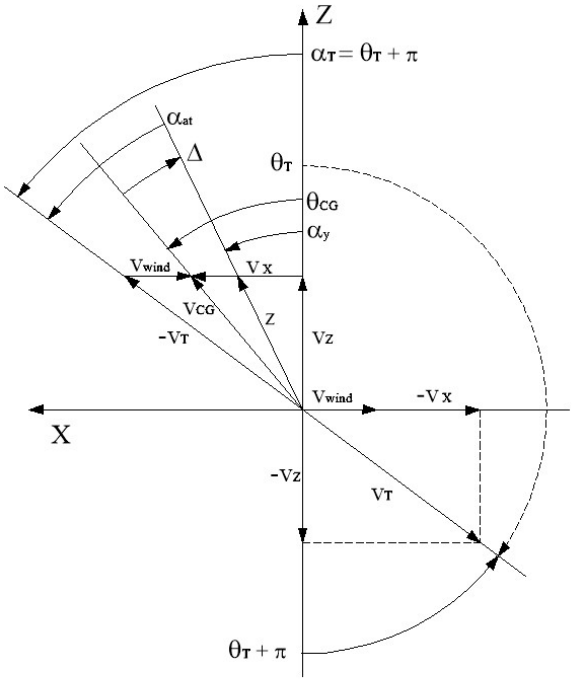

Figure 7-3 Key velocity vectors and angles

Rather than stating equations (7.1-4) to (7.1-9) directly in terms of the state variables, which makes the equations very long, intermediate functions are used. The intermediate variables also provide insight into the behavior of the model. The following equations define the intermediate variables in terms of the state variables of the system.

θ_{CG} is the angle of the velocity vector, v_{CG} , of the center of gravity of the rocket, which is not necessarily the same direction as the rocket is pointed. It is defined by the X and Z-axis velocities.

$$\theta_{CG} = \arctan\frac{v_X}{v_Z} \tag{7.1-10}$$

Δ is the difference between the direction the rocket traveling and the rocket is pointed

$$\Delta = \theta_{CG} - \alpha_y \tag{7.1-11}$$

The Z-axis component of the oncoming airstream is the negative of the Z component of the rocket's velocity. The X -axis component of the oncoming airstream is the negative of the X-axis component of the rocket's velocity plus the velocity of the wind. The total oncoming airstream velocities are

$$v_{TX} = v_w - v_X \tag{7.1-12}$$

$$v_{TZ} = -v_Z \tag{7.1-13}$$

$$v_T = \sqrt{{v_{TX}}^2 + {v_{TZ}}^2} = \sqrt{(v_w - v_X)^2 + {v_Z}^2} \tag{7.1-14}$$

θ_T is the angle of the total oncoming airstream. Since the airstream is opposite the direction of the rocket's velocity, the angle is in the quadrant opposite the rocket's direction of travel. α_T is the angle of the oncoming airstream reflected back into the quadrant of the rocket's travel.

$$\theta_T = -\arcsin\frac{v_{TX}}{v_T} + \pi = -\arcsin\frac{v_w - v_X}{v_T} + \pi \tag{7.1-15}$$

$$\alpha_T = \theta_T - \pi = -\arcsin\frac{v_w - v_X}{v_T} \tag{7.1-16}$$

The angle of attack is the difference between the angle of the negative of the oncoming airstream and the rotation angle of the rocket's rotation

$$\alpha_{at} = \alpha_T - \alpha_y \tag{7.1-17}$$

The trajectory force equations are[30]

$$F_{DX} = \frac{\rho}{2} \cdot A_r \cdot C_D \cdot {v_T}^2 \cdot \sin\theta_T \tag{7.1-18}$$

$$F_{DZ} = \frac{\rho}{2} \cdot A_r \cdot C_D \cdot {v_T}^2 \cdot \cos\theta_T \tag{7.1-19}$$

$$F_{LX} = \frac{\rho}{2} \cdot A_r \cdot C_{L\alpha} \cdot \alpha_{at} \cdot {v_T}^2 \cdot \cos\theta_T \tag{7.1-20}$$

$$F_{LZ} = -\frac{\rho}{2} \cdot A_r \cdot C_{L\alpha} \cdot \alpha_{at} \cdot {v_T}^2 \cdot \sin\theta_T \tag{7.1-21}$$

[30] (Mandell, Caporaso, & Bengen, 1973)

$$F_{TX} = F_T \cdot \sin \alpha_y \tag{7.1-22}$$

$$F_{TZ} = F_T \cdot \cos \alpha_y \tag{7.1-23}$$

and the rotational force and moment equations are

$$F_{N1y} = -\frac{\rho}{2} \cdot A_r \cdot C_{N\alpha} \cdot v_T{}^2 \cdot \alpha_{at} \tag{7.1-24}$$

$$F_{N2y} = +\frac{\rho}{2} \cdot A_r \cdot C_{N\alpha} \cdot v_T \cdot \omega_y \cdot (L_{CP} - L_{CG}) \tag{7.1-25}$$

$$M_{1y} = -F_{N1y} \cdot (L_{CP} - L_{CG}) \tag{7.1-26}$$

$$M_{2y} = -F_{N2y} \cdot (L_{CP} - L_{CG}) \tag{7.1-27}$$

$$M_{2R} = -\frac{L_m \cdot m_p}{6 \cdot t_b} \cdot (3 \cdot L_{ne} - 3 \cdot L_{CG} - L_m) \cdot \omega_y \tag{7.1-28}$$

Equations (7.1-4) to (7.1-28) are the complete model of a rocket in flight needed to describe its location and orientation in 2-dimensional space. The 6 first order differential equations (7.1-4) to (7.1-9) that solve for the 6 state variables are nonlinear, so they cannot be solved in closed form, but they can be solved numerically using the rkfixed function in Mathcad.

Figure 7-4 shows examples of the output of the complete Mathcad flight model using the parameters for the test rocket TR-1. The physical parameters for TR-1 are given in Section 3. Most of the graphs in this paper are based on the output of the model using the TR-1 parameters.

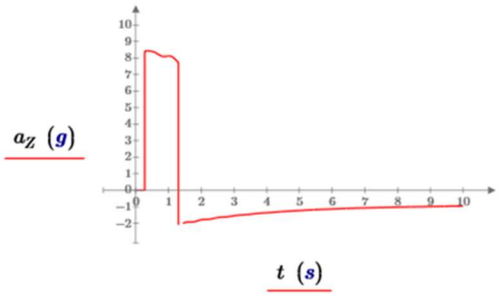

Z-axis acceleration

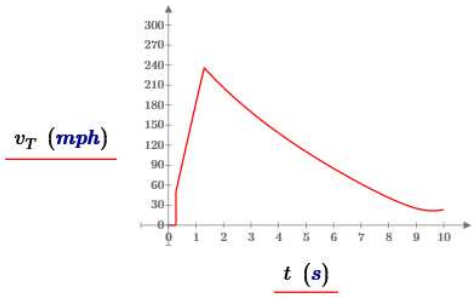

Total incident airstream velocity

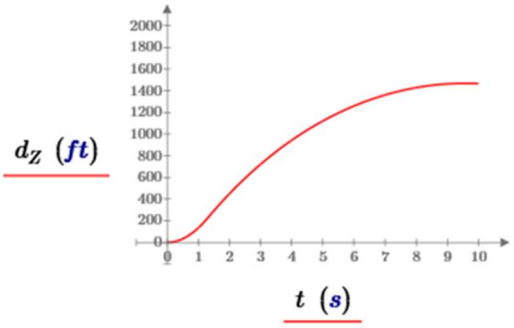

Z-axis distance (altitude)

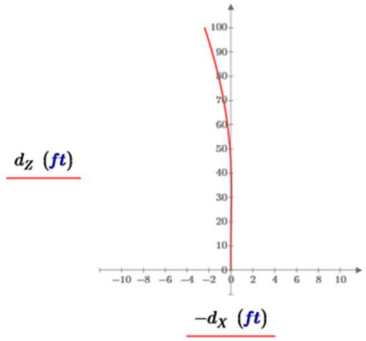

Trajectory

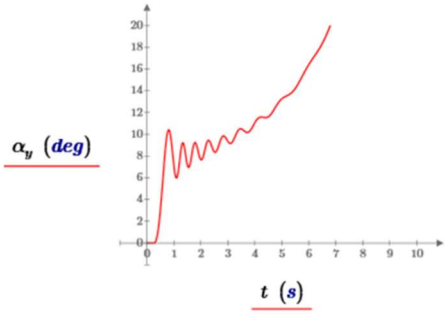

Rotation angle of the rocket

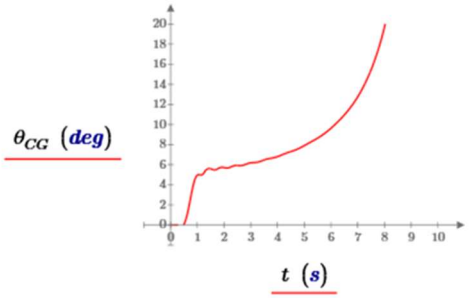

Flight path trajectory angle

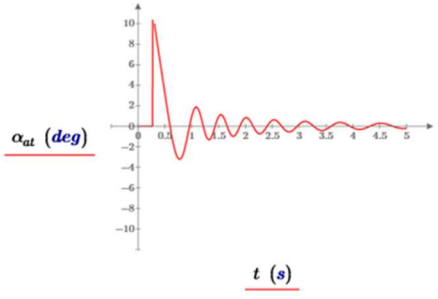

Angle of attack

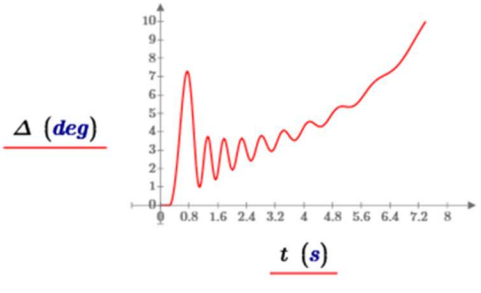

Difference between the rocket rotation angle and the flight path angle

Figure 7-4 Example of the output of the complete trajectory and rotational stability model using the parameters for test rocket TR-1 flying on an AT H128W motor and a 10 mph step in wind velocity as the rocket leaves the launch guide

Figure 7-5 shows a comparison between the flight model (red trace) and flight data (blue trace) from test rocket TR-1. The altitude prediction matches very closely, and the rotation angles match very closely over the first three seconds assuming an initial 10 mph step in wind velocity.

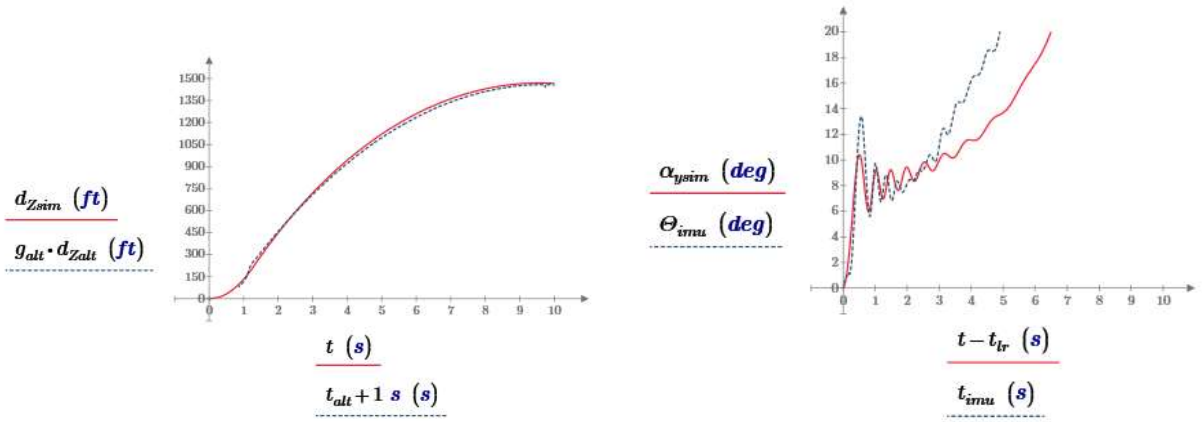

Figure 7-5 Comparing the model to flight data from 5/19/23 flight of TR-1 assuming a 10 mph wind

Figure 7-6 shows a comparison of the forcing moment, the top graph, the rotational rate damping moment, the left graph, and the jet damping moment, the right graph for TR-1. The jet damping aligns in phase with the rotational rate damping, so it adds to the overall damping of the system, as expected. For the AT-H128W motor used in test rocket TR-1, the magnitude of the jet damping calculated using the core burning motor equation is less than one tenth the rotational damping magnitude, so the jet damping would add very little to the rocket's rotational stability. The core burner model was used for all the simulation results presented in this paper as it matches the geometry of the motor used. Also note that the jet damping only contributes for the length of the motor burn.

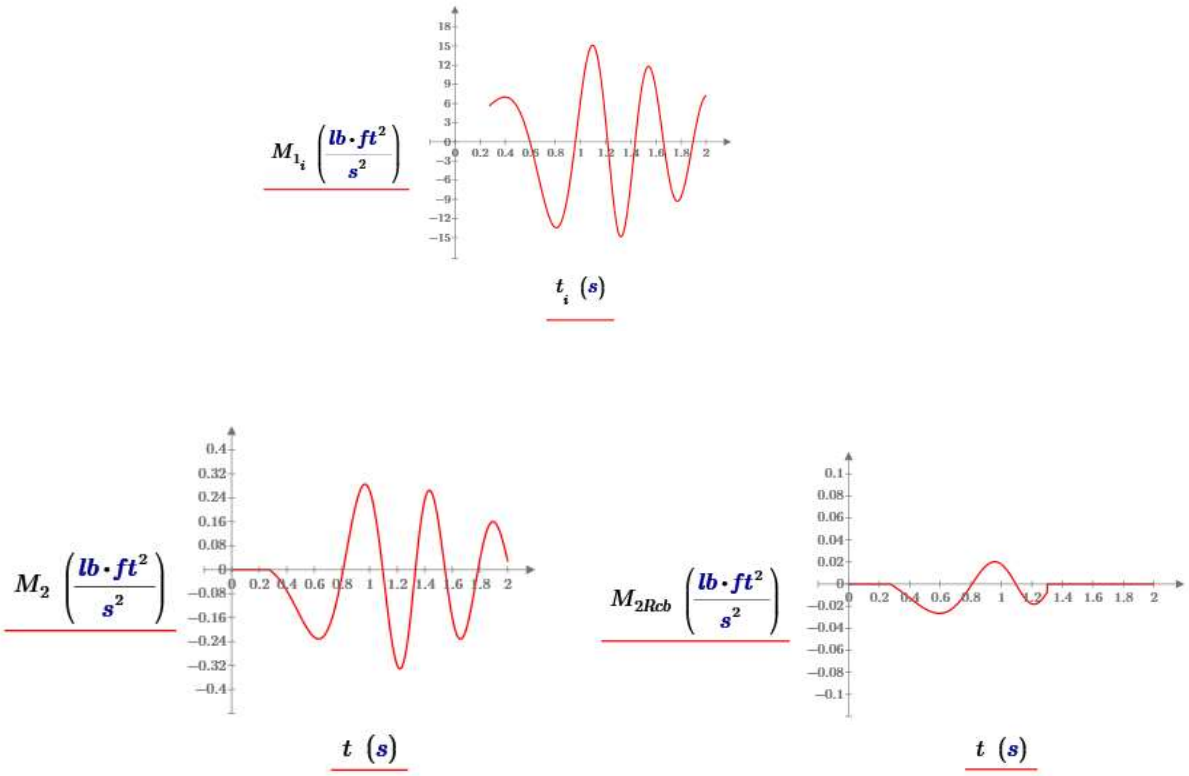

Figure 7-6 Comparing the forcing moment, M_1, rotational rate damping moment, M_2, and the jet damping moment calculated for a core burning motor, M_{2Rcb}, for test rocket TR-1 flying on an AT H128W motor and a 10 mph step in wind velocity

8 Appendix 3 – Second Order Systems & Root Locus

8.1 Second Order System Response

A second order system has both a first order and second order derivative. Starting with the general form of the second order differential equation

$$C_3 \cdot \frac{d^2\alpha_{out}(t)}{dt^2} + C_2 \cdot \frac{d\alpha_{out}(t)}{dt} + C_1 \cdot \alpha_{out}(t) = C_0 \cdot \alpha_{in}(t) \tag{8.1-1}$$

then, taking the Laplace transform, the frequency domain gain equation is

$$C_3 \cdot s^2 \cdot \alpha_{out}(s) + C_2 \cdot s \cdot \alpha_{out}(s) + C_1 \cdot \alpha_{out}(t) = C_0 \cdot \alpha_{in}(t) \tag{8.1-2}$$

In this equation C_0 and C_1 are the forcing coefficients, as the 0th order terms of the equation drive the system response, and C_2 is the damping coefficient, as the 1st order term dampens the system response.

Rearranging terms

$$\frac{\alpha_{out}(s)}{\alpha_{in}(s)} = G(s) = \frac{C_0}{C_1} \cdot \frac{1}{\frac{C_3}{C_1} \cdot s^2 + \frac{C_2}{C_1} \cdot s + 1} \tag{8.1-3}$$

Equation (8.1-3) can be also be written in terms of two constants, the natural frequency ω_n and the damping ratio, ζ

$$\frac{\alpha_{out}(s)}{\alpha_{in}(s)} = G(s) = \frac{C_0}{C_1} \cdot \frac{1}{\frac{s^2}{{\omega_n}^2} + \frac{2 \cdot \zeta \cdot s}{\omega_n} + 1} \tag{8.1-4}$$

where:

$$\omega_n = \sqrt{\frac{C_1}{C_3}} \tag{8.1-5}$$

and

$$\zeta = \sqrt{\frac{C_2{}^2}{4 \cdot C_1 \cdot C_3}} \tag{8.1-6}$$

The time domain equation in terms of the natural frequency ω_n and the damping ratio ζ is

$$\frac{1}{\omega_n{}^2} \cdot \frac{d^2 \alpha_{out}}{dt^2} + \frac{2 \cdot \zeta}{\omega_n} \cdot \frac{d \alpha_{out}}{dt} + \alpha_{out} = \frac{C_0}{C_1} \cdot \alpha_{in} \tag{8.1-7}$$

Equation (8.1-6) shows that the damping ratio, ζ, is proportional to the damping coefficient, C_2, and inversely proportional to the square root of the driving coefficient, C_1, and C_3. If the damping coefficient increases while C_1, and C_3 remain constant, the damping ratio will increase by the same factor as the damping coefficient.

The frequency domain gain is function of the complex frequency $s = j\omega$, so the gain has both a magnitude and a phase, which is the physical meaning of the mathematical notation of complex frequency. The magnitude of the gain function is the ratio of the amplitude of the sinusoidal output signal to the amplitude of a sinusoidal input signal at each frequency, and the phase is the phase shift between the input and output sinusoid at each frequency.

The magnitude and phase are found from the real and imaginary parts of the complex function by

$$\text{Mag}\left[G(s)\right] = \sqrt{\text{Re}\left[G(s)\right]^2 + \text{Im}\left[G(s)\right]^2} \tag{8.1-8}$$

$$\text{Phase}\left[G(s)\right] = \text{atan}\left(\frac{\text{Im}\left[G(s)\right]}{\text{Re}\left[G(s)\right]}\right) \tag{8.1-9}$$

where the phase is in radians. When the log of the magnitude is plotted against the log of the frequency and linear phase is plotted against the log of the frequency, this is called a Bode plot.

The coefficients of the equation are grouped in terms of ω_n and ζ because these two parameters independently describe the shape of both the frequency and time domain responses of the second order system. Figure 8-1 shows plots of the magnitude and phase (Bode plot) for two values of ω_n, $1Hz$ and $2Hz$. This is a low-pass filter response where ω_n is the asymptotic corner frequency.

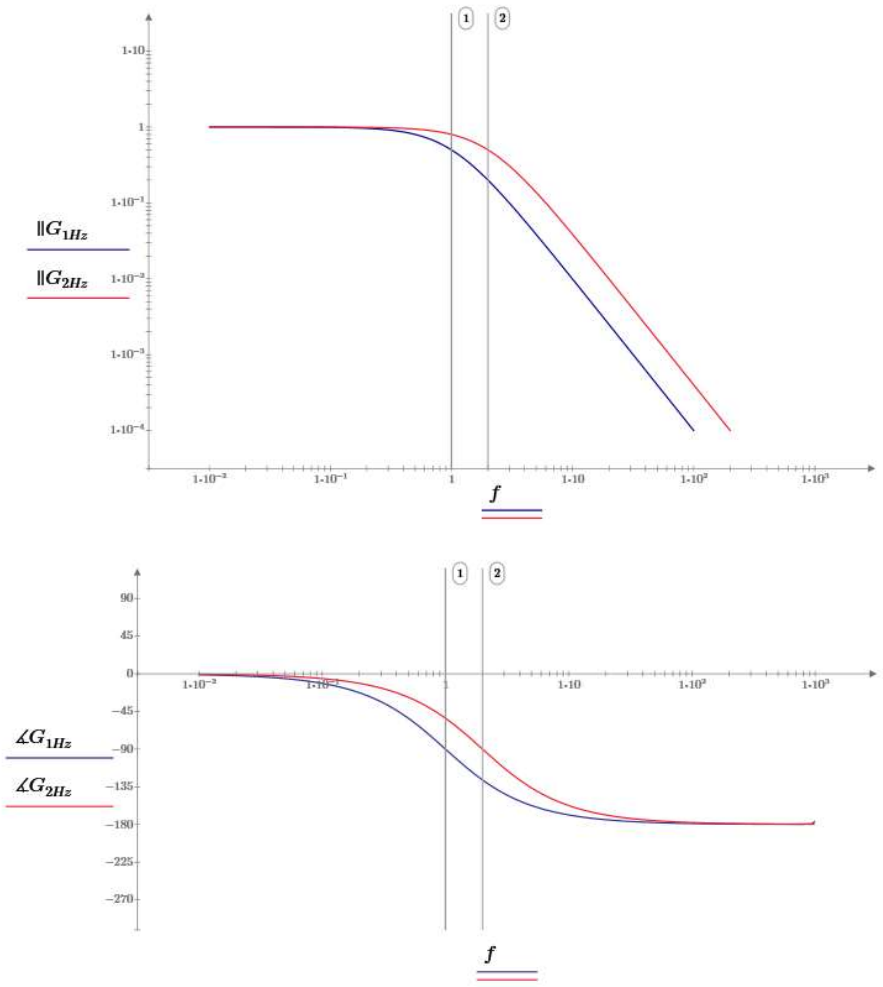

Figure 8-1 Magnitude and phase of the frequency response of a second order system for $\omega_n = 1Hz \,\&\, 2Hz$ and $\zeta = 1$

Figure 8-2 shows the frequency response of the second order equation for ζ equal to 3, 1, 0.3, and 0.03. As the value of ζ is decreased below a value of 1, the gain of the function increases above a gain of 1 at the equation's resonant, or natural frequency ω_n. This is the frequency at which the second order system oscillates in the time domain in response to a perturbation such as an impulse or step function.

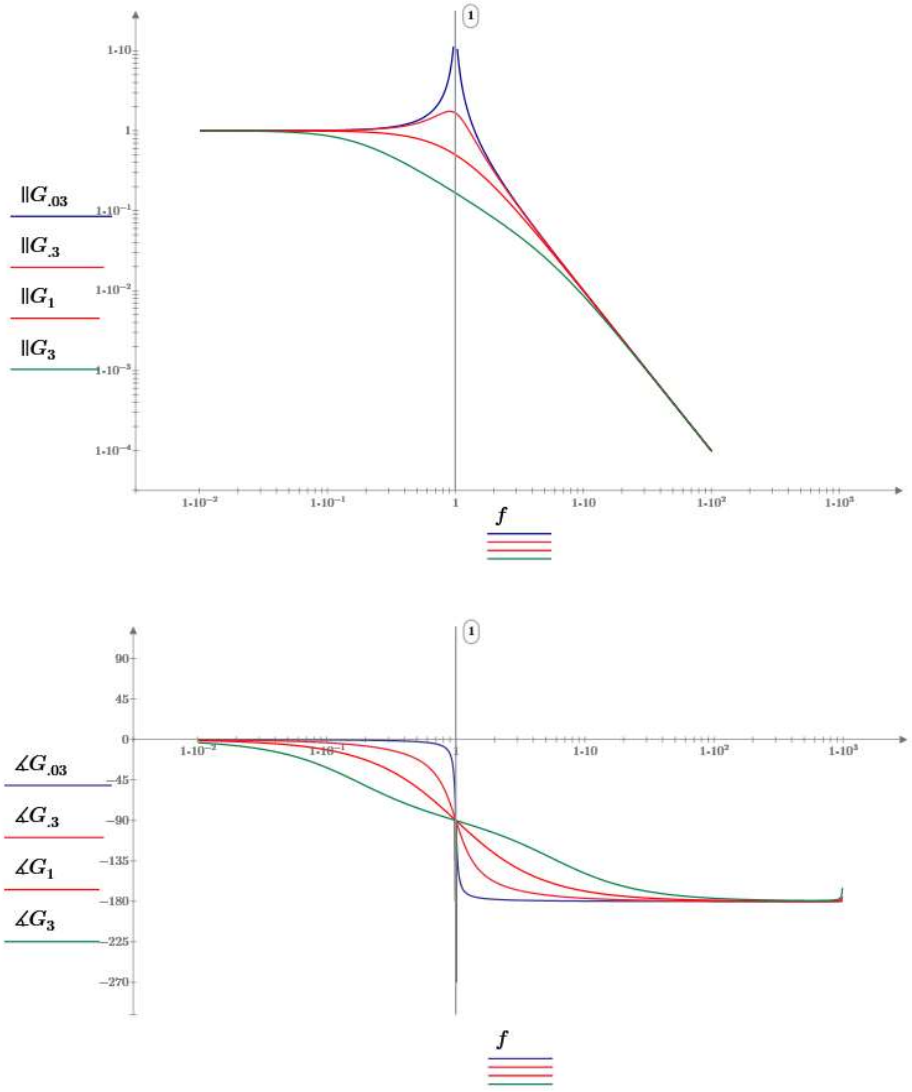

Figure 8-2 Magnitude and phase response of the second order system for $\omega_n = 1Hz$ and $\zeta = .03,.3,1,3$

The gain peaking causes the 3 dB bandwidth of the system to increase with decreasing ζ, even though the asymptotic corner frequency, ω_n remains constant. The 3 dB bandwidth can be calculated from the natural frequency and the damping ratio by[31]

$$\omega_{3dB} = \omega_n \cdot \sqrt{1 - 2 \cdot \zeta^2 + \sqrt{2 - 4 \cdot \zeta^2 + 4 \cdot \zeta^4}} \tag{8.1-10}$$

[31] (Roberge, 1975, p. 95)

Figure 8-3 shows the 3 dB bandwidth of a second order system, for $\omega_n = 1 \cdot 2\pi$ and $\zeta = 0.3$, equals 1.45 Hz

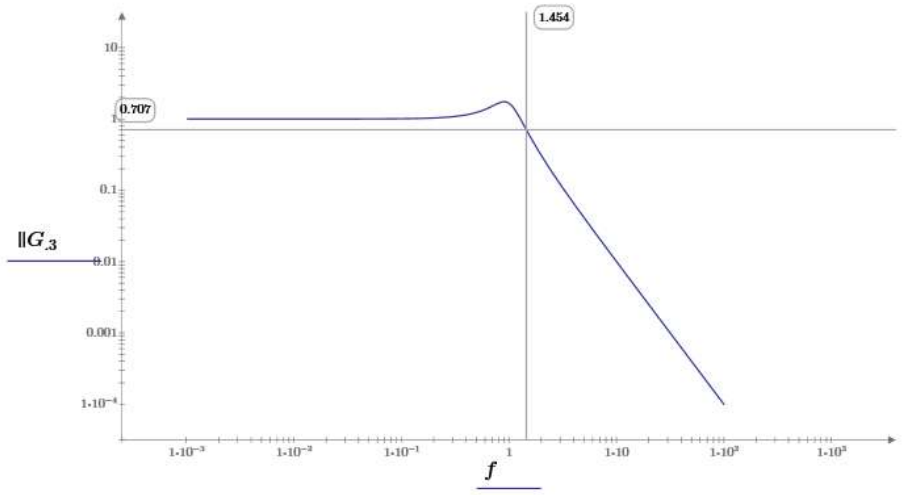

Figure 8-3 3 dB bandwidth of a second order system for $\omega_n = 1 \cdot 2\pi$ and $\zeta = 0.3$

Multiplying the gain function by the frequency domain step, $1/s$, and taking the inverse Laplace transform gives the time domain step response of the system

$$\mathcal{L}^{-1}\left(\frac{1}{s}\cdot G(s)\cdot\right) = \alpha_{out}(t)\Big|_{step} \tag{8.1-11}$$

The step response for the second order equation (8.1-4), assuming the gain $C_0/C_1 = 1$, is

$$\mathcal{L}^{-1}\left(\frac{1}{s}\cdot G(s)\right) = \mathcal{L}^{-1}\left(\frac{1}{s}\cdot\frac{1}{\left(\frac{s^2}{{\omega_n}^2}+\frac{2\cdot\zeta\cdot s}{\omega_n}+1\right)}\right) =$$

$$\alpha_{out}(t)\Big|_{step} = \left(-\frac{\zeta\cdot\omega_n}{\sqrt{(-\zeta^2+1)\cdot{\omega_n}^2}}\cdot e^{-(\zeta\cdot\omega_n\cdot t)}\cdot\sin\left(t\cdot\sqrt{(-\zeta^2+1)\cdot{\omega_n}^2}\right) - e^{-(\zeta\cdot\omega_n\cdot t)}\cdot\cos\left(t\cdot\sqrt{(-\zeta^2+1)\cdot{\omega_n}^2}\right)+1\right)$$

(8.1-12)

Figure 8-4 shows the second order system step response for equation (8.1-12) for ζ equals 3, 1 (critically damped), 0.3, and 0.03. The step response with the largest sinusoidal ringing is for a ζ value of .03, while the slowest response with the no ringing is for a ζ value of 3. The amplitude of the decaying oscillations follows an inverse exponential envelope that can be seen in equation (8.1-12). The response of critically damped the system with a ζ value of 1 has the fastest rise time response, for the given value of ω_n, with no overshoot or ringing.

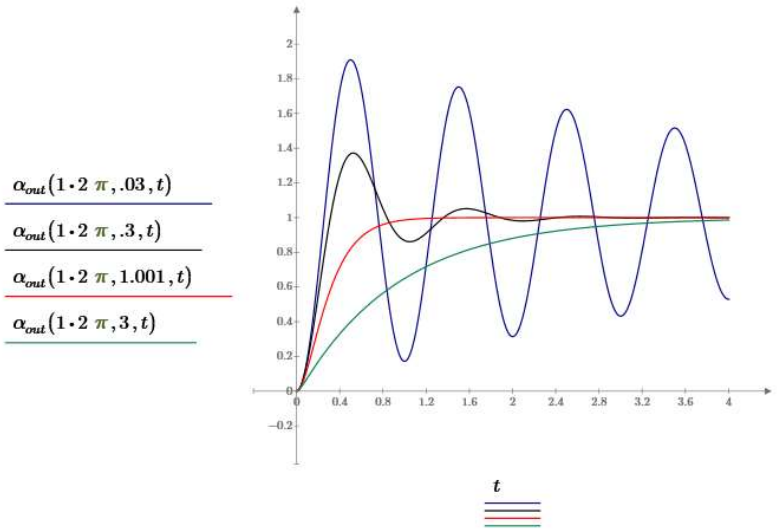

Figure 8-4 Second order system step response for $\omega_n = 1Hz$ and $\zeta = .03, .3, 1, 3$

Increasing the resonant frequency, ω_n, while holding ζ constant, decreases the rise time and increases the frequency of the ringing, but does not impact the overshoot or number of cycles of oscillation in the decay envelop, as shown in Figure 8-5. The slower step response is for $\omega_0 = 2\pi \cdot 1Hz$, while the faster response is for $\omega_n = 2\pi \cdot 2Hz$. In both cases, $\zeta = 0.3$.

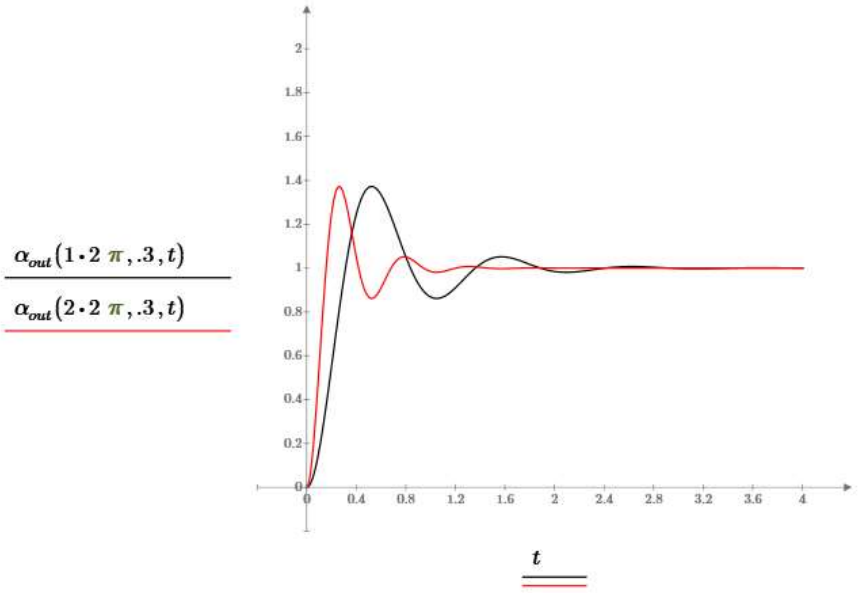

Figure 8-5 Second order system for $\omega_n = 1Hz \,\&\, 2Hz$ and $\zeta = .3$

The rise time of a second order system is defined as the time between the step response reaching 10% and 90% of the final value, and is approximated by[32]

$$t_{rise} \simeq \frac{2.2}{\omega_{3dB}} = \frac{2.2}{\omega_n \cdot \sqrt{1 - 2 \cdot \zeta^2 + \sqrt{2 - 4 \cdot \zeta^2 + 4 \cdot \zeta^4}}} \tag{8.1-13}$$

Figure 8-6 shows the 10-90% rise time of a second order system for $\omega_n = 1 \cdot 2\pi$ and $\zeta = 0.3$ is approximately 0.24 seconds as calculated by equation (8.1-13).

[32] (Roberge, 1975, p. 95)

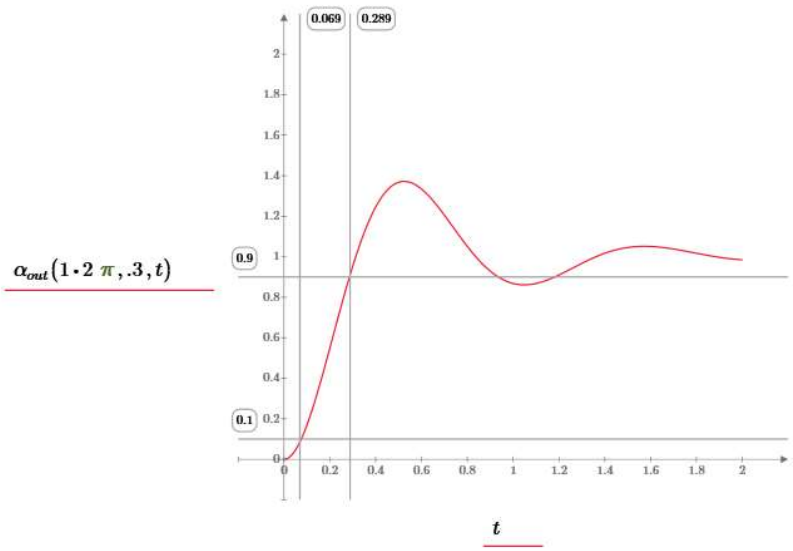

Figure 8-6 10% to 90% rise time of a second order system for $\omega_n = 1 \cdot 2\pi$ and $\zeta = 0.3$

Figure 8-7 shows each of the terms of the second order differential equation (8.1-7) for two different values of the damping ratio, $\zeta = 0.03$, and $\zeta = 0.3$, where the input, α_{in}, is a unit step at $t = 0$. The first order damping term leads the forcing term by 90 degrees because α'_{out} is the derivative, or slope of α_{out}. The second order term, in turn, leads the first order term by another 90 degrees, because α''_{out} is the derivative, or slope of the first order term α'_{out}. Comparing the two graphs, the ringing in the step response decays faster when the first order damping term, (red trace), is initially larger compared to the other terms, due to the larger damping ratio. This effect will be seen when analyzing the rotational dynamic stability of a rocket.

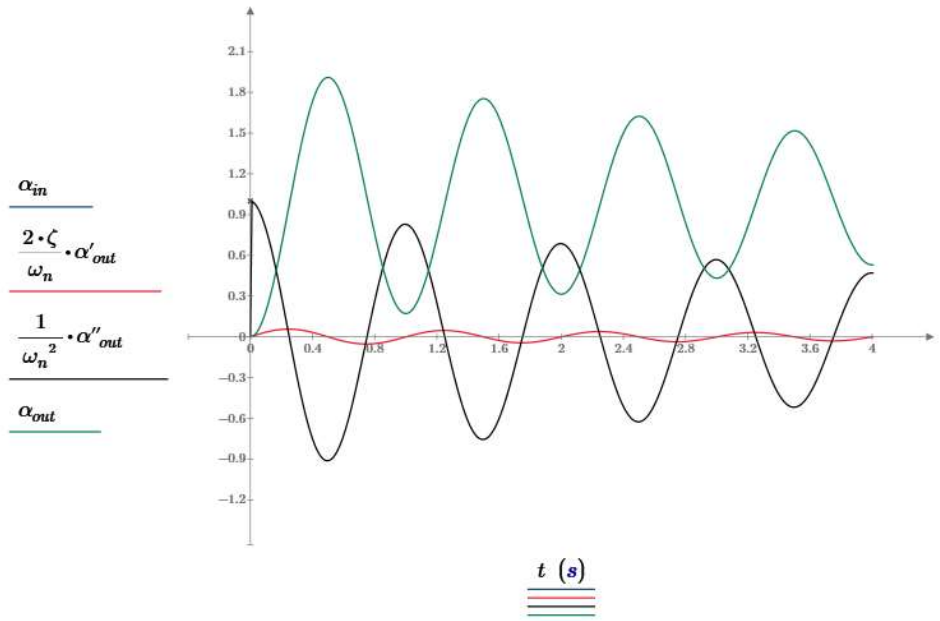

$\omega_n = 1 \cdot 2\pi$, $\zeta = 0.03$

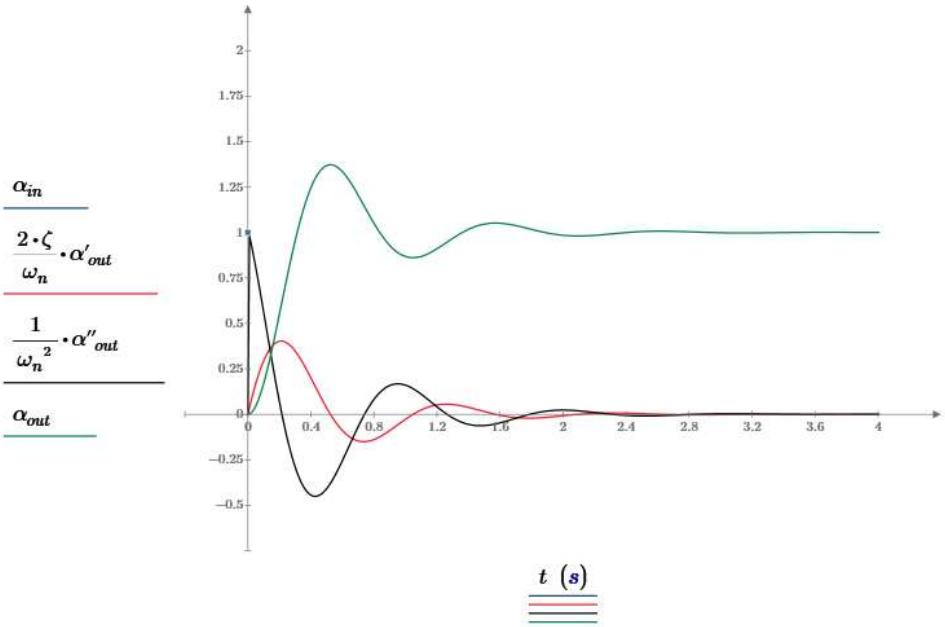

$\omega_n = 1 \cdot 2\pi$, $\zeta = 0.3$

Figure 8-7 Plotting the terms of the second-order equation for two different damping ratios

Note: $d\alpha_{out}/dt = \alpha'_{out}$ and $d^2\alpha_{out}/dt^2 = \alpha''_{out}$ in this graph

8.2 Roots of the Frequency Domain Equation

The roots of a differential equation in the frequency domain characterize the behavior of the system. The generalized form of the frequency domain gain equation is a ratio of algebraic polynomials of order m and n

$$G(s) = \frac{K_m \cdot s^m + K_{m-1} \cdot s^{m-1} + ... + K_0}{C_n \cdot s^n + C_{n-1} \cdot s^{n-1} + ... + C_0} \tag{8.2-1}$$

The roots are the solution of the equation with the input set to zero. This is called the homogeneous form of the equation. An n^{th} order polynomial can be solved numerically by Mathcad or other analysis tools to find the roots, but it is more informative if the solution can be solved symbolically to show the effect each of the parameters has on the solution. Solving the polynomial symbolically involves factoring the polynomial. Many physical systems can be modeled as first or second order systems, so the system equation typically starts out in factored form, made up of first and second order polynomials. If the design process starts out in the frequency domain, the system can be constructed from a series of lower order blocks that are already in factored form. The roots of the polynomial are the roots of each of the polynomial's factors which are found by setting each first or second order factor to zero and solving for *s*.

The roots of the numerator of the system gain equation (8.2-1) are called zeros because the overall gain of the equation goes to zero when the frequency is equal to that root. The roots of the denominator of equation (8.2-1) are called poles. Since the root goes to zero when the frequency is equal to that root, the overall gain of the system goes to infinity at the frequency of a pole. Because the solution to the system equation goes to infinity at its poles, the poles are also called singularities.

For a first order gain equation,

$$\frac{\alpha_{out}(s)}{\alpha_{in}(s)} = G(s) = \frac{C_0}{C_1} \cdot \frac{1}{\left(\frac{C_2}{C_1} \cdot s + 1\right)} = \frac{C_0}{C_1} \cdot \frac{1}{\left(\frac{s}{\omega_c} + 1\right)} \tag{8.2-2}$$

the root of the denominator is found by setting it equal to zero and solving for s

$$\frac{C_2}{C_1} \cdot s + 1 = 0 \tag{8.2-3}$$

the root, or pole is

$$s = -\frac{C_1}{C_2} = -\omega_c \tag{8.2-4}$$

A useful tool in understanding the behavior of a system is a plot of the real and imaginary portions of the roots. This is called an s-plane plot. An s-plane plot is a plot of the real part of the complex number, σ , on the horizontal axis, and the imaginary part, $j\omega$, on the orthogonal vertical axis. The poles are represented by **x**'s, and the zeros by **o**'s.

Figure 8-8 shows an s-plane plot of the pole location for $\omega_c = 1 \cdot 2\pi$. For a physical system, the pole of a first order system is always real and will fall on the real axis of the s-plane. The distance along the real axis from the origin to the pole location is ω_c .

$$\sigma = -\omega_c = -6.283 \tag{8.2-5}$$

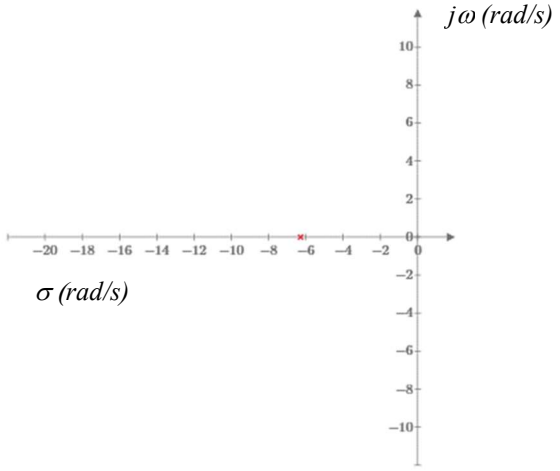

Figure 8-8 s-plane plot of the pole of the first order system for $\omega_c = 1 \cdot 2\pi$

For a second order gain equation,

$$\frac{\alpha_{out}(s)}{\alpha_{in}(s)} = G(s) = \frac{C_0}{C_1} \cdot \frac{1}{\frac{C_3}{C_1} \cdot s^2 + \frac{C_2}{C_1} \cdot s + 1} = \frac{C_0}{C_1} \cdot \frac{1}{\frac{s^2}{\omega_n^{\,2}} + \frac{2 \cdot \zeta \cdot s}{\omega_n} + 1} \tag{8.2-6}$$

the roots of the denominator are found by setting it equal to zero and solving for s

$$C_3 \cdot s^2 + C_2 \cdot s + C_1 = 0 \tag{8.2-7}$$

For a quadratic equation

$$a \cdot x^2 + b \cdot x + c = 0 \tag{8.2-8}$$

the solution for x, the roots are

$$x = \frac{-b \pm \sqrt{b^2 - 4 \cdot a \cdot c}}{2 \cdot a} \tag{8.2-9}$$

So, the roots or poles of the gain equation (8.2-6) are

$$s = \frac{-C_2 \pm \sqrt{-(4 \cdot C_3 \cdot C_1) + C_2{}^2}}{2 \cdot C_3} = -\zeta \cdot \omega_n \pm \sqrt{\left(\zeta^2 - 1\right) \cdot \omega_n{}^2} \tag{8.2-10}$$

The real and imaginary poles in terms of ω_n and ζ are

$$s = \sigma \pm \omega \cdot j = -\zeta \cdot \omega_n \pm \sqrt{\left(\zeta^2 - 1\right) \cdot \omega_n{}^2} \tag{8.2-11}$$

where the real portion, for $\omega_n = 1 \cdot 2\pi$ and $\zeta = 0.3$, is

$$\sigma = \mathrm{Re}\left(-\zeta \cdot \omega_n \pm \sqrt{\left(\zeta^2 - 1\right) \cdot \omega_n{}^2}\right) = -\zeta \cdot \omega_n = -1.885 \tag{8.2-12}$$

and the imaginary portion is

$$\begin{aligned} \omega &= \mathrm{Im}\left(-\zeta \cdot \omega_n \pm \sqrt{\left(\zeta^2 - 1\right) \cdot \omega_n{}^2}\right) \\ &= \mathrm{Im}\left(-\zeta \cdot \omega_n \pm \sqrt{-1 \cdot \left(1 - \zeta^2\right) \cdot \omega_n{}^2}\right) \\ &= \mathrm{Im}\left(-\zeta \cdot \omega_n \pm \sqrt{\left(1 - \zeta^2\right) \cdot \omega_n{}^2} \cdot j\right) \\ &= \pm\sqrt{\left(1 - \zeta^2\right) \cdot \omega_n{}^2} = \pm 5.994 \end{aligned} \tag{8.2-13}$$

The roots of equation (8.2-6) are real for $(4 \cdot C_3 \cdot C_1) \le C_2{}^2$ or $\zeta \ge 1$, and complex conjugates, meaning they both have the same real component, and complimentary imaginary components, for $(4 \cdot C_3 \cdot C_1) > C_2{}^2$ or $\zeta < 1$.

Figure 8-9 shows the s-plane plot of the complex conjugate pair of roots for $\omega_n = 1 \cdot 2\pi$ and $\zeta = 0.3$.

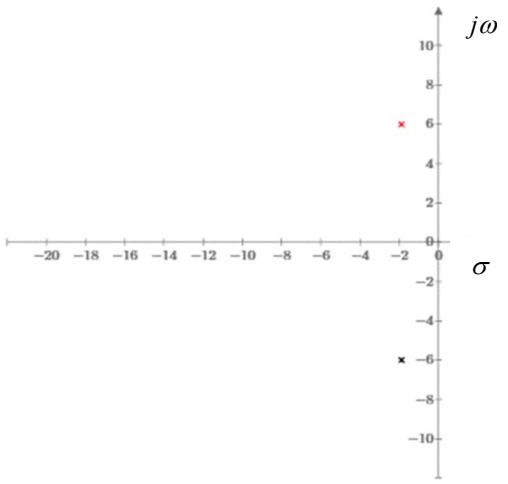

Figure 8-9 s-plane plot of a conjugate pair of roots for $\omega_n = 1 \cdot 2\pi$ and $\zeta = 0.3$

The location of the poles can also be expressed in terms of polar coordinates. Using the functions from equations (8.2-12) and (8.2-11) for $\mathrm{Re}(s)$ and $\mathrm{Im}(s)$, the distance from the origin to the pole location is ω_n, and the angle between the real axis and the pole is the arccosine of ζ as shown in Figure 8-10

$$\sqrt{\left(\mathrm{Re}(s)\right)^2 + \left(\mathrm{Im}(s)\right)^2} = \sqrt{\left(-\zeta \cdot \omega_n\right)^2 + \left(\sqrt{\left(1-\zeta^2\right) \cdot {\omega_n}^2}\right)^2} = \omega_n \tag{8.2-14}$$

and

$$\mathrm{Re}(s) = -\zeta \cdot \omega_n \Rightarrow -\frac{\mathrm{Re}(s)}{\omega_n} = \zeta \Rightarrow \arccos(\zeta) = \phi \tag{8.2-15}$$

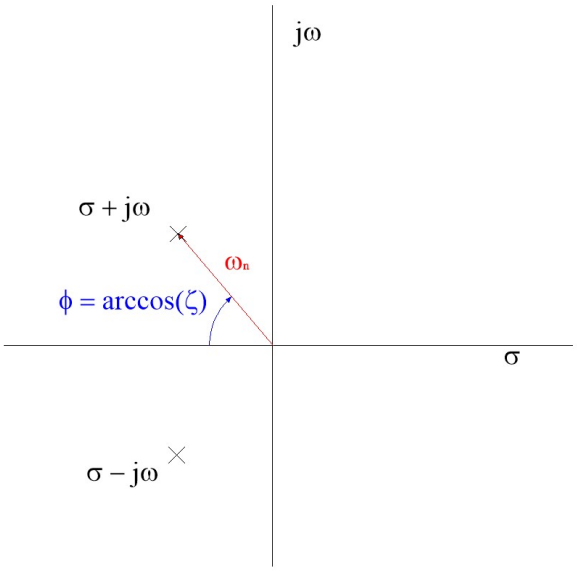

Figure 8-10 s-plane pole locations in terms of ω_n and ζ

The advantage of the polar coordinates is the magnitude is a function of just ω_n, and the angle is a function of just ζ, so it is easy to see the connection between the pole locations and ω_n and ζ. If the poles move radially away from the center of the s-plane, the natural frequency increases, but the damping ratio remains constant. If the poles move along a fixed radius arc, the natural frequency remains constant, but the damping ratio changes with the system becoming less stable as the poles move closer to the imaginary axis. Figure 8-11 shows a plot of the angle of the pole versus the damping ratio. As seen in Figure 8-4, damping ratios above 0.3 have a small amount of overshoot and a fast decay time. Figure 8-11 shows that for systems having damping ratios less than 0.3, the poles are within 17 degrees of the imaginary axis.

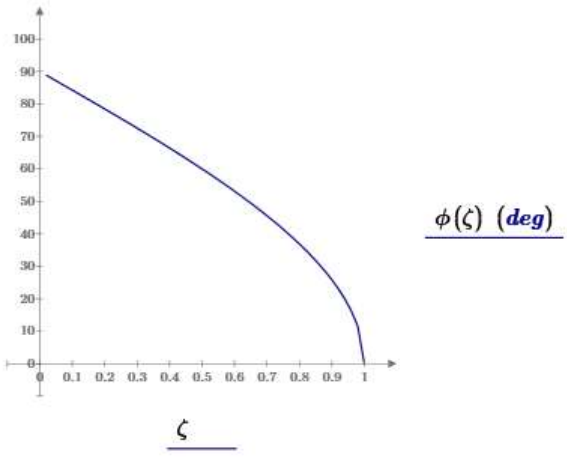

Figure 8-11 Angle of the s-plane pole location as a function of the damping ratio

For physical systems, complex roots will always be complex conjugate pairs. So, in factored form, a higher order system will be comprised of first and second order functions if the functions can be factored. The first order equations cover the real poles and zeros, and the second order equations cover the complex conjugate pair poles and zeros, or pairs of poles on the real axis.

8.3 Right Half vs Left Half Plane Poles

The poles of the system gain equation can fall on the left or right half of the s-plane. Any system with one or more poles that fall in the right half plane will be unstable, meaning the output response to an impulse input will increase exponentially over time, whereas a system with just left half plane poles will be stable, meaning the output response to an impulse input will decrease over time. For a stable system, a system the takes longer to settle to zero is less stable than a system that takes shorter to settle to zero.

For a second order system, if ζ goes negative, the poles are in the right half of the s-plane, and the system will produce an exponentially increasing oscillation envelope. Mathematically, this can happen, but in a real-world system, something would eventually limit the amplitude of the oscillations. If ζ is set equal to 0, the poles are on the imaginary axis of the s-plane, and the system will produce a stable oscillation of constant amplitude. For a system with a positive value of ζ, the poles are in the left half of the s-plane, and the system is stable. A system that has a smaller positive value of ζ and more overshoot is said to be less stable than a system with a larger value of ζ, less overshoot, and a faster decay envelope.

For the second order system of equation (8.1-4), the pole locations are

$$\left(\frac{s^2}{\omega_n^{\,2}}+\frac{2\cdot\zeta\cdot s}{\omega_n}+1\right)=0\Rightarrow s=-\zeta\cdot\omega_n\pm\sqrt{\left(\zeta^2-1\right)\cdot\omega_n^{\,2}} \tag{8.3-1}$$

Table 8-1 shows the location of the poles on the s-plane for all ranges of ζ. If $\zeta<0$, there will always be at least one right half plane pole.

Case	Criteria	Pole Location
1	$\zeta > 1$	Two negative real axis poles
2	$\zeta = +1$	Two negative real axis poles at the same frequency
3	$0 < \zeta < +1$	Two complex conjugate negative real poles
4	$\zeta = 0$	Two complex conjugate poles on the $j \cdot \omega$ axis
5	$0 > \zeta > -1$	Two complex conjugate positive real poles
6	$\zeta = -1$	Two positive real axis poles at the same frequency
7	$\zeta < -1$	Two positive real axis poles

Table 8-1 Location of the poles of equation (8.3-1) for all ranges of ζ

Figure 8-12 shows the second order step response, equation (8.1-12), for three values of ζ , +0.1, 0.001 (~0), and -0.1, cases 3, 4, and 5, in Table 8-1, producing a decreasing, constant, and increasing envelop, respectively.

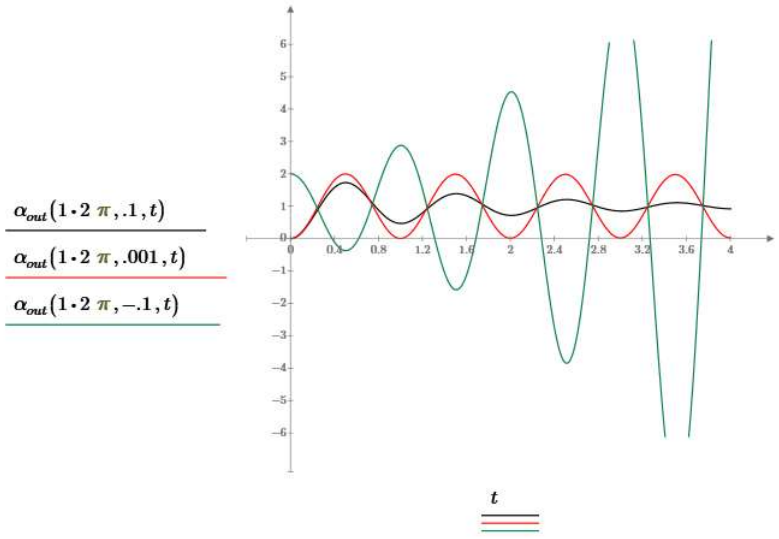

Figure 8-12 Second order step response for of ζ , +0.1, 0.001 (~0), and -0.1, with $\omega_n = 1 \cdot 2\pi$

If the second order system equation is written in the form of equation (8.1-3), then the roots are

$$\left(\frac{C_3}{C_1}\cdot s^2+\frac{C_2}{C_1}\cdot s+1\right)=0\Rightarrow s=\frac{-C_2\pm\sqrt{-4\cdot C_1\cdot C_3+C_2^{\,2}}}{2\cdot C_3} \tag{8.3-2}$$

Using the Mathcad symbolic capability, the step response for the second order system written in this form is

$$\alpha_{out}(t)\big|_{step}=-\left(\frac{C_2}{2\cdot C_3\cdot\sqrt{\frac{4\cdot C_1\cdot C_3-C_2^{\,2}}{4\cdot C_3^{\,2}}}}\right)\cdot e^{\frac{-C_2\cdot t}{2\cdot C_3}}\cdot\sin\left(t\cdot\sqrt{\frac{4\cdot C_1\cdot C_3-C_2^{\,2}}{4\cdot C_3^{\,2}}}\right)-e^{\frac{-C_2\cdot t}{2\cdot C_3}}\cdot\cos\left(t\cdot\sqrt{\frac{4\cdot C_1\cdot C_3-C_2^{\,2}}{4\cdot C_3^{\,2}}}\right)+1 \tag{8.3-3}$$

Table 8-2 shows the location of the poles on the s-plane for various ranges of the coefficients. If $C_2<0$, there will always be at least one right half plane pole. Written in this form as a function of C_1, C_2, and C_3, gives more latitude in the placement of the poles than the equation expressed in terms of just ω_n and ζ. The former allows for a pair of poles on the real axis, one negative and one positive.

Case	Criteria	Pole Location
1	$4\cdot C_1\cdot C_3<C_2^{\,2}$ & $C_2>0$	Two real axis poles with at least one negative
2	$4\cdot C_1\cdot C_3=C_2^{\,2}$ & $C_2>0$	Two negative real axis poles at the same frequency
3	$4\cdot C_1\cdot C_3>C_2^{\,2}$ & $C_2>0$	Two complex conjugate negative real poles
4	$C_2=0$	Two complex conjugate poles on the $j\cdot\omega$ axis
5	$4\cdot C_1\cdot C_3>C_2^{\,2}$ & $C_2<0$	Two complex conjugate positive real poles
6	$4\cdot C_1\cdot C_3=C_2^{\,2}$ & $C_2<0$	Two positive real axis poles at the same frequency
7	$4\cdot C_1\cdot C_3<C_2^{\,2}$ & $C_2<0$	Two real axis poles with at least one positive

Table 8-2 Location of the poles of equation (8.3-2) for all ranges of C_2

Figure 8-13 shows the step response for equation (8.3-3) for $C_3=2$, $C_2=0.5$, and $C_1=-20$. The pole locations are +3.04 and -3.29 radians/sec. Because the poles are on the real axis, there is no imaginary part that gives rise to a sinusoidal response, there is just an increasing exponential response.

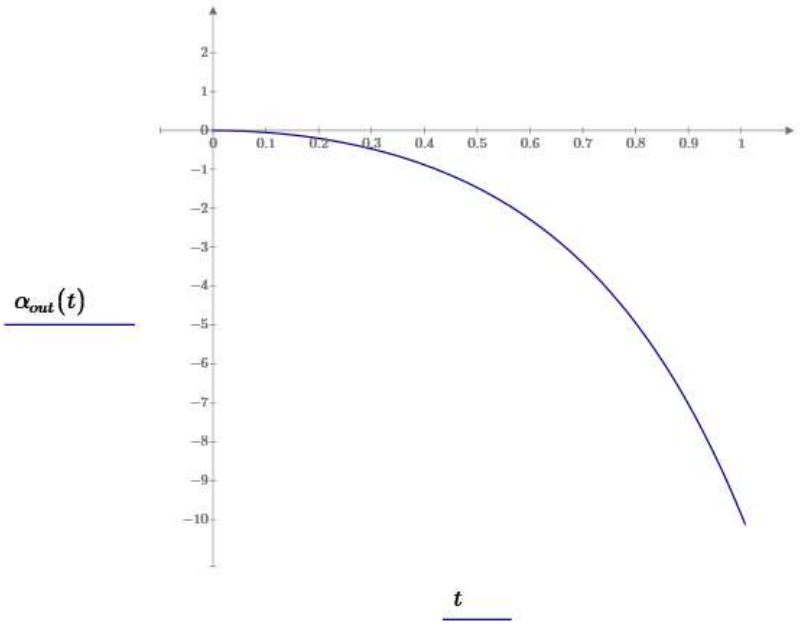

Figure 8-13 Step response of two real poles, one negative and one positive

For the case where there is one positive and one negative pole on the real axis, equation (8.3-1) or (8.3-2) can be simplified by knowing that the solution consists of two first order real poles as shown in equation (8.3-4).

$$G(s) = \frac{1}{\left(\frac{s}{\omega_1} + 1\right) \cdot \left(\frac{s}{\omega_2} + 1\right)} \tag{8.3-4}$$

The inverse Laplace transform of $G(s) \cdot \frac{1}{s}$ for the step response is

$$\alpha_{out}(t)\Big|_{step} = 1 + \frac{-\omega_2 \cdot e^{-\omega_1 \cdot t} + \omega_1 \cdot e^{-\omega_2 \cdot t}}{\omega_2 - \omega_1} \tag{8.3-5}$$

Even though there is both a positive and negative exponential, the magnitude of the positive exponential quickly exceeds the magnitude of the negative exponential, and the resulting sum grows exponentially as shown in Figure 8-14.

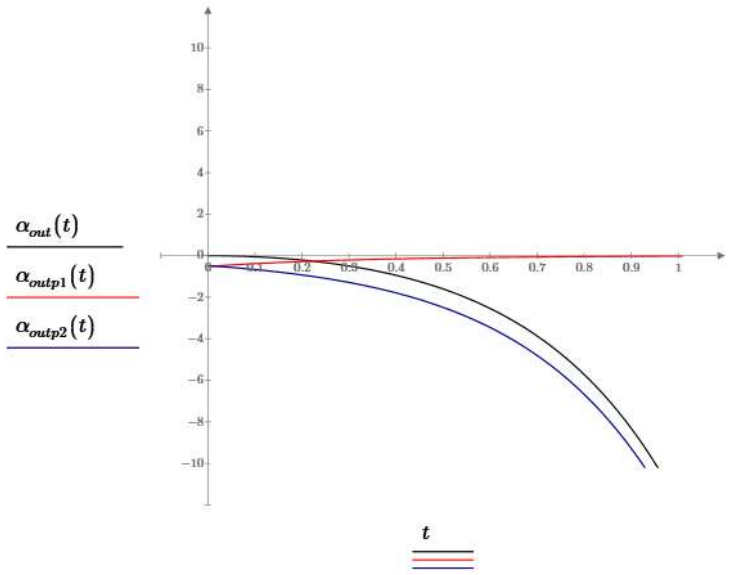

Figure 8-14 Plot of $\alpha_{out}(t)\Big|_{step}$, $\alpha_{outp1} = \frac{\omega_2}{\omega_1 - \omega_2} \cdot e^{-\omega_1 \cdot t}$, and $\alpha_{outp2} = \frac{\omega_1}{\omega_2 - \omega_1} \cdot e^{-\omega_2 \cdot t}$

In summary, any system with all left half s-plane poles will produce a response with an exponentially decaying envelope, which is a stable response. If there is a single pole on the left half real axis, the response is a simple decaying exponential. If there is a pair of left half complex conjugate poles, then the response will a decaying sinusoid. If there is a single pole on the right half real axis, the response is a simple increasing exponential. If there is a pair of right half complex conjugate poles, then the response will be an exponentially increasing sinusoid. Any order system with at least one right half plane pole will produce an exponentially increasing envelope, which is an unstable system. A system with a complex conjugate pole pair on the $j\omega$ axis will produce a stable, constant amplitude sinusoidal response.

8.4 Gain and Phase from Poles & Zeros

The magnitude and phase of the gain of a system can be determined directly from the location of its poles and zeros on the s-plane.

The magnitude of a gain function is the product of the lengths of each of the vectors that extend from all the zeros to a test frequency on the $j\omega$ axis divided by the product of the lengths of each of the vectors that extend from all the poles to that same test frequency on the $j\omega$ axis as shown in Figure 8-15. The phase is the sum the angles of each

of the vectors that extend from all the zeros to the test frequency on the $j\omega$ axis minus the sum of the angles of each of the vectors that extend from all the poles to that same test frequency on the $j\omega$ axis. The length of the vector from a pole of zero to the $j\omega$ axis approaches a factor of 10 for each factor of 10 in frequency well past the frequency of the pole or zero. The angles go from -90 deg to + 90 deg for each pole or zero. For frequencies less than the pole and zero frequencies, the ratio of the length of the vector from the zeros and the poles remains relatively constant, so the magnitude of the gain function remains relatively constant.

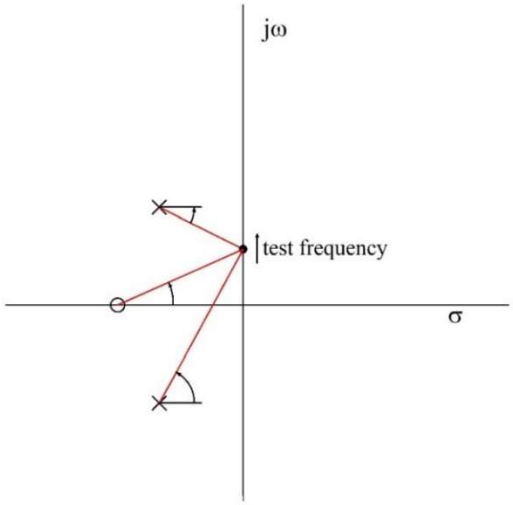

Figure 8-15 Magnitude and phase from s-plane poles and zeros

The Bode plot, then, can be constricted just knowing the locations of the poles and zeros on the s-plane. Each zero contributes +20 dB/decade in magnitude above its corner frequency and +90 deg in phase. Each pole contributes -20 dB/decade in magnitude and -90 deg in phase. Systems with just poles are low pass in nature as the gain decreases above the frequency of the poles. A system that has only zeros, or zeros at a lower frequency than poles, would be high pass in nature as the gain increases at a stimulus frequency higher than the frequency of the zeros.

Figure 2-22 shows the magnitude and phase of equation (8.4-1), a system consisting of a single pole, for $\omega_c = 1 \cdot 2\pi$. The magnitude decreases at 20 dB per decade above ω_c, and the phase increases to -90 deg.

$$G(s) = \frac{1}{\left(\frac{s}{\omega_c} + 1\right)} \tag{8.4-1}$$

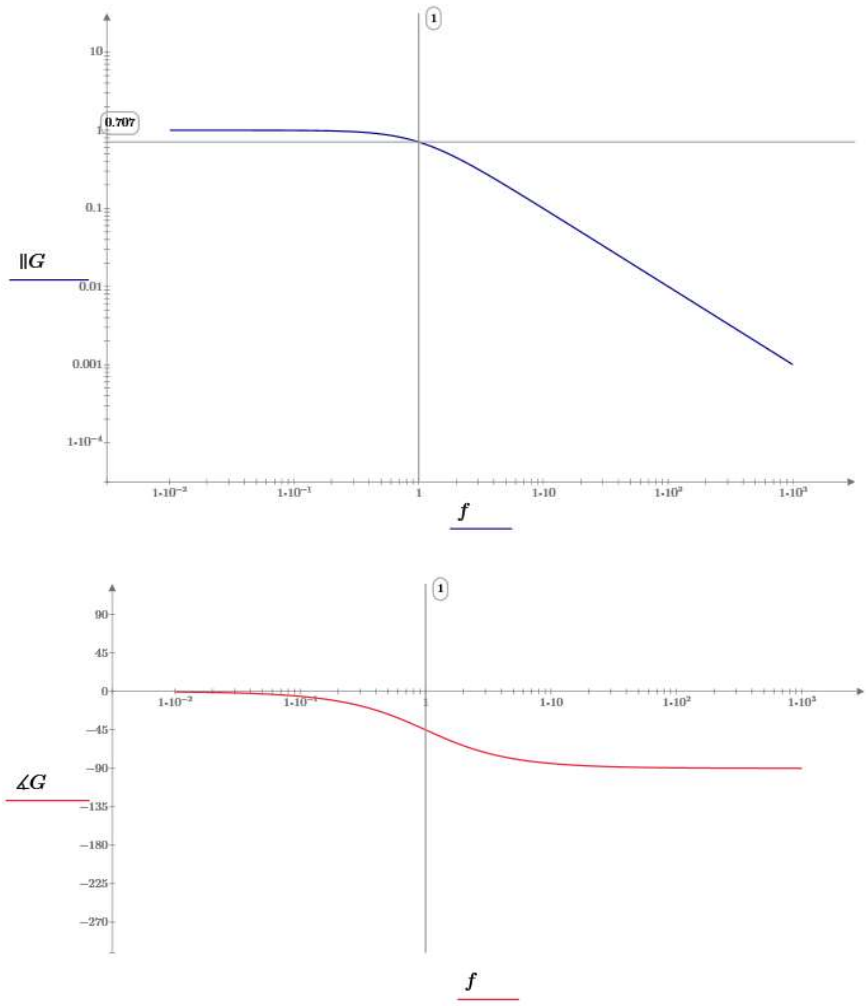

Figure 8-16 Magnitude and phase of the frequency response of a first order system for $C_1 = 1$ and $\omega_c = 1 \cdot 2\pi$

Figure 8-17 shows the magnitude and phase of equation (8.4-2), a system consisting of a single zero, for $\omega_c = 1 \cdot 2\pi$. The magnitude and phase of the gain is the inverse of the single pole function of equation (8.4-1). The magnitude increases at 20 dB per decade above ω_c, and the phase increases to +90 deg.

$$G(s) = \left(\frac{s}{\omega_c} + 1\right) \tag{8.4-2}$$

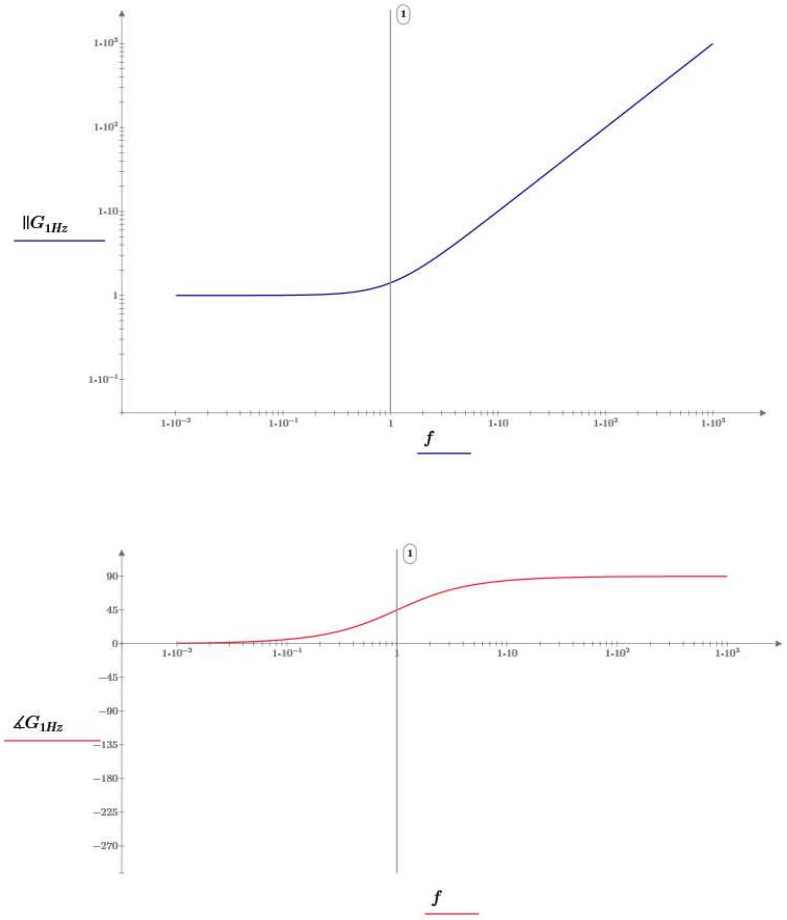

Figure 8-17 Magnitude and phase of equation (8.4-2) for $\omega_c = 1 \cdot 2\pi$

Equation (8.4-3) is a gain function with a real axis zero and a complex pole pair. Figure 8-18 shows a plot of the poles and zero for $\omega_z = 1 \cdot 2\pi$, $\omega_n = 1 \cdot 2\pi$, and $\zeta = 0.5$. The magnitude and phase of that gain function is shown in Figure 8-19. For the function, the net number of poles and zeros is one, that is, there is one more pole than zero, so the function will eventually roll off at 20 dB/decade, and the final phase is 90 deg. There is peaking in the gain as the test frequency passes closest to the complex pole because of the proximity of the pole pair to the $j\omega$ axis when ζ is less than 1. The closer the pole is to the $j\omega$ axis, the greater the peaking as shown Figure 8-2. Since the zero falls at the same frequency as the polls, it has the effect of negating the change in magnitude and phase from one of the poles, but the peaking in magnitude from the polls' proximity to the imaginary axis still occurs.

$$G(s) = \frac{\left(\frac{s}{\omega_z} + 1\right)}{\left(\frac{s^2}{\omega_n{}^2} + \frac{2 \cdot \zeta}{\omega_n} + 1\right)} \tag{8.4-3}$$

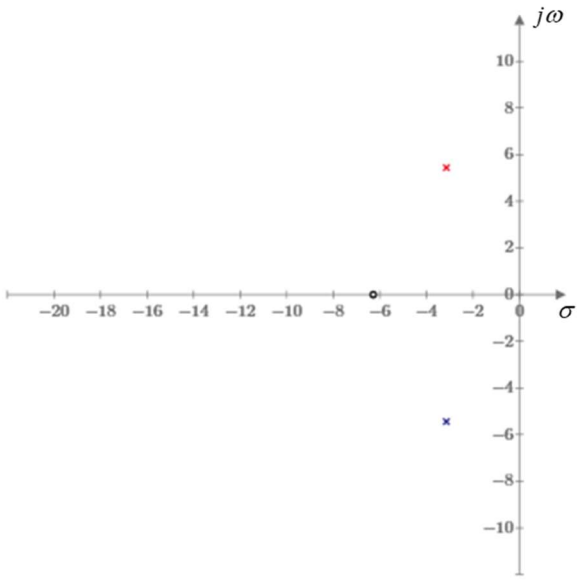

Figure 8-18 s-plane plot of the roots of equation (8.4-3) for $\omega_z = 1 \cdot 2\pi$, $\zeta = 0.5$, and $\omega_z = 1 \cdot 2\pi$

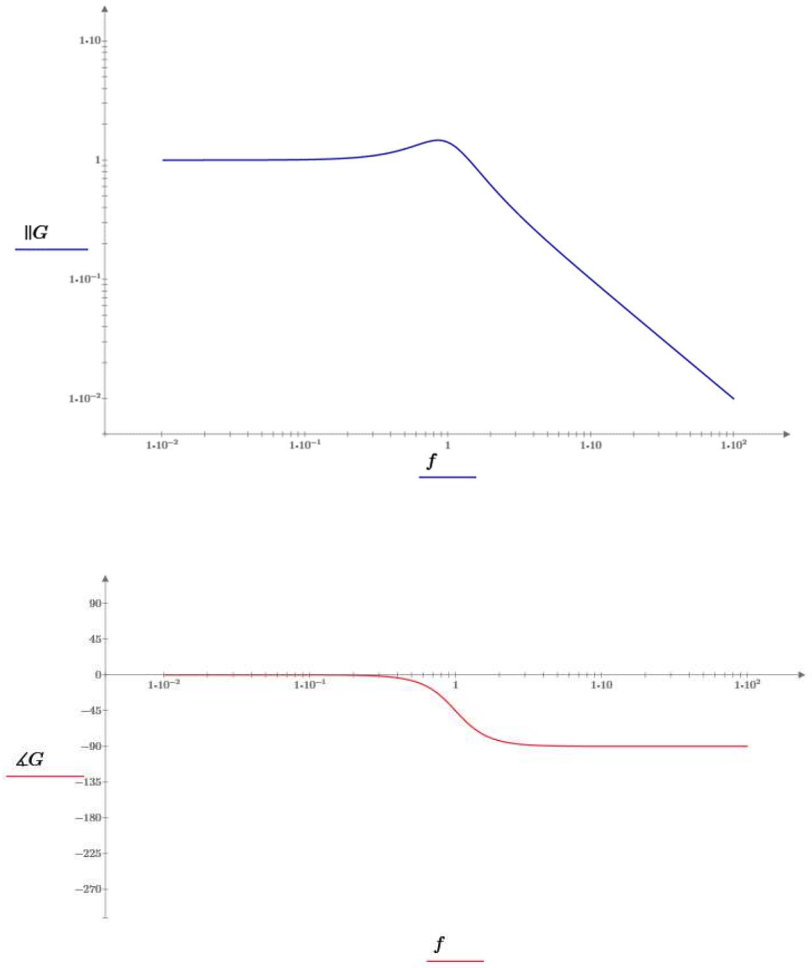

Figure 8-19 Magnitude and phase of the gain of equation (8.4-3) for $\omega_z = 1 \cdot 2\pi$, $\omega_n = 1 \cdot 2\pi$, and $\zeta = 0.5$

8.5 Root Locus

An s-plane plot of the roots of a differential equation as a function of a parameter that changes the location of the roots is called the root locus. The root locus can be used to determine how that parameter impacts the stability of the system. Root locus plots are commonly used in designing control systems, where the design parameter being varied is the loop gain of the control loop. But root locus plots are also useful for understanding the stability of any system with complex poles where the location of the poles can be expressed as a function of any design parameter that impacts the pole locations. For the control gain function, there are a series of heuristic rules that govern the trajectory of the poles as a function of the loop gain. But Mathcad can be used to solve for the root locus numerically for most any gain function.

The stability of a system is determined by the damping ratio of complex pole pairs. The angle of the pole is a function of the arccosine of the damping ratio, as shown in Figure 8-10. The larger the angle, the less stable the system as shown in Figure 8-11.

Figure 8-20 shows the trajectory of the poles for a constant ζ while varying ω_n. The poles move along a straight line at a distance of ω_n from the origin. These are lines of constant ζ. If the trajectory of the poles moves off a straight-line trajectory and move toward the imaginary axis, the system becomes less stable as the parameter is being varied. If the trajectory of the poles moves off the straight-line trajectory away from the imaginary axis, then the system becomes more stable as that parameter is varied. If the trajectory remains on the straight line, the bandwidth of the system increases or decreases while the damping ratio and stability remain constant.

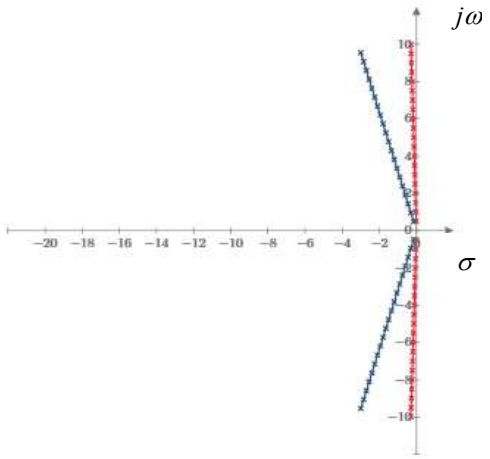

Figure 8-20 Locus of poles varying $0.5 \le \omega_n \le 10$ for $\zeta = 0.3$ (blue) and $\zeta = 0.03$ (red)

Figure 8-21 shows the trajectory of the polls for constant ω_n while varying ζ. For values of $\zeta \ge 1$ the poles are on the real axis. For values of $0 < \zeta < 1$ the poles split into a complex conjugate pair and move toward the imaginary axis at a radius of ω_n. In this plot, ζ is varied in equal increments, with the locations marked by the x's. This shows that the poles move much faster along the real axis as ζ approaches 1, and then more slowly again with decreasing ζ as they move away from the real axis as a complex conjugate pair and approach the imaginary axis. Once the poles leave the real axis and move closer to the imaginary axis, the damping ratio and stability of the system decreases as the controlling parameter is varied, while the natural frequency remains constant.

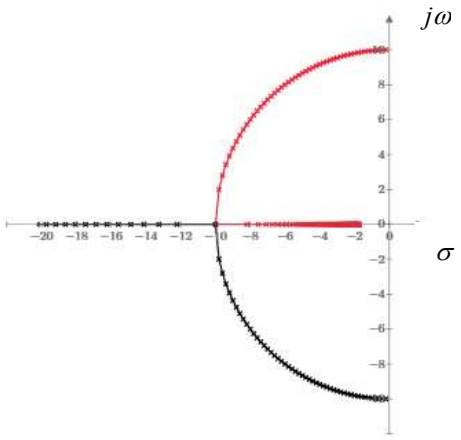

Figure 8-21 Locus of poles varying $3 \geq \zeta \geq 0.2$ for $\omega_n = 10$

The relationships between the pole locations and ω_n and ζ help with understanding the stability of a system based on the trajectory of the locus of the roots of the system equation.

8.6 Second Order System with a Zero

One of the models used for the rotational stability system is a second order differential equation that includes a zero in the numerator. This section characterizes that system.

The frequency domain form of the equation is

$$\frac{\alpha_{out}(s)}{\alpha_{in}(s)} = G_2(s) = G_0 \cdot \frac{\frac{s}{\omega_z} + 1}{\frac{s^2}{\omega_n^2} + \frac{2 \cdot \zeta \cdot s}{\omega_n} + 1} \tag{8.6-1}$$

Figure 8-22 shows the gain of (8.6-1) for various damping ratios and zero frequencies locations where the frequency of the zero is significantly lower than the frequency of the poles. In these plots, the pole frequency is 1 Hz, the damping ratios are 0.5 and 0.05, the zero frequencies are 0.1 Hz and 0.01 Hz, and the gain $G_0 = 1$. The gain rises at 20 dB/decade starting at the frequency of the zero. The two poles at resonance then cause the gain to turn around and fall at 20 dB/decade. If the frequency of the zero is moved down by a factor of 10, the gain of the function at its peak increases by a factor of 10, regardless of the value of the damping ratio.

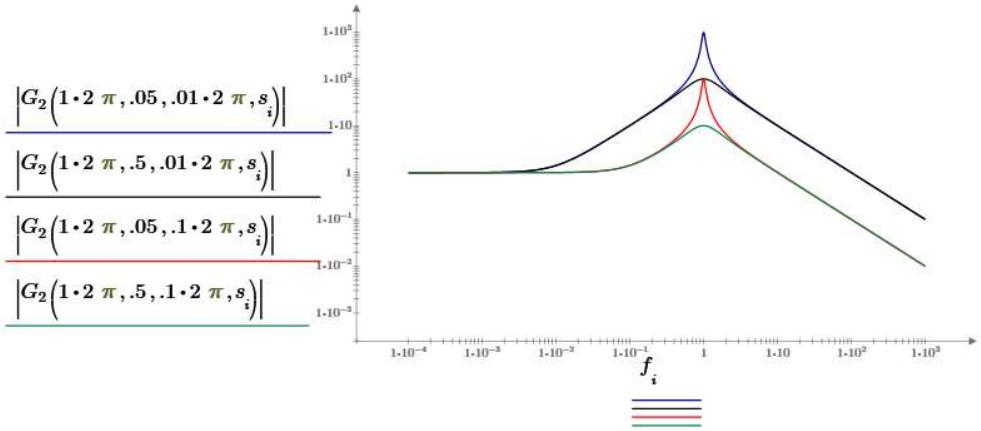

Figure 8-22 Second order equation with varying damping ratio, ζ, and zero location, ω_z

Figure 8-23 compares the second order system response with and without the zero. The effective gain at resonance due to the zero is the ratio of the pole to zero frequencies. If the second order system without the zero is multiplied by that gain, then the peak of its gain at resonance is the same as the second order system with the zero.

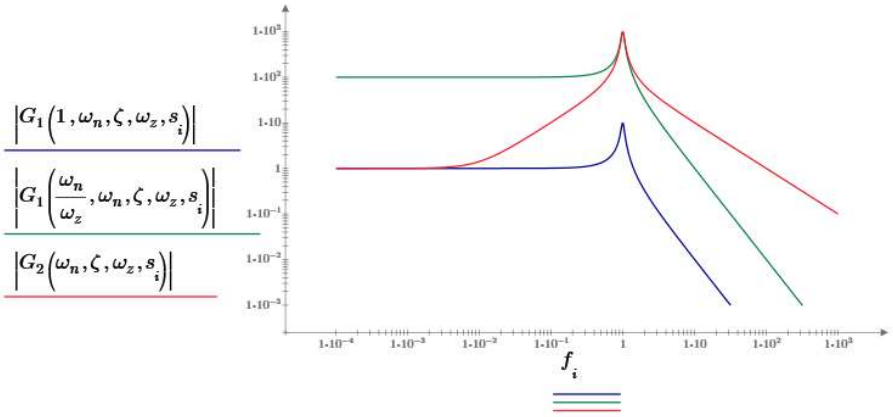

Figure 8-23 Comparing the second order system with and without the zero

The time domain step response of a system is found by taking the inverse Laplace transform of the frequency domain step function, $1/s$, multiplied by the frequency domain gain function. Using the symbolic engine in Mathcad, the step response for the second order equation (8.6-1), assuming the gain $C_0 = 1$, is

$$\mathcal{L}^{-1}\left(\frac{1}{s}\cdot G_2(s)\right)=\mathcal{L}^{-1}\left(\frac{1}{s}\cdot\frac{\frac{s}{\omega_z}+1}{\frac{s^2}{{\omega_n}^2}+\frac{2\cdot\zeta\cdot s}{\omega_n}+1}\right)=$$

$$\alpha_{out}(t)\Big|_{step}=\frac{{\omega_n}^2-\zeta\cdot\omega_n\cdot\omega_z}{\omega_z\cdot\sqrt{(-\zeta^2+1)\cdot{\omega_n}^2}}\cdot e^{-(\zeta\cdot\omega_n\cdot t)}\cdot\sin\left(t\cdot\sqrt{(-\zeta^2+1)\cdot{\omega_n}^2}\right)-e^{-(\zeta\cdot\omega_n\cdot t)}\cdot\cos\left(t\cdot\sqrt{(-\zeta^2+1)\cdot{\omega_n}^2}\right)+1 \tag{8.6-2}$$

The step response is plotted in Figure 8-24. The zero being well below the pole frequency results in a final step magnitude that is very small compared to the magnitude of the oscillations. The graph on the right shows the step response for the second order system without the zero for comparison. The frequency of oscillation and the decay envelope for the system with the zero are the same as the second order system without the zero, but the oscillations lead the system without the zero by 90 degrees because of the zero.

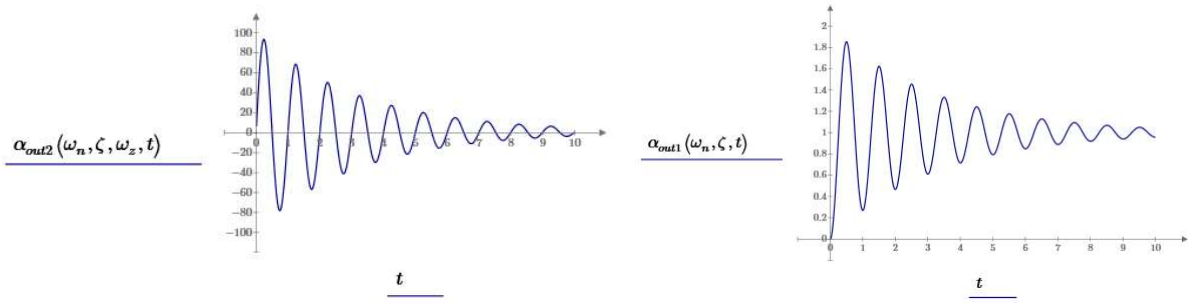

Figure 8-24 Plot of the step response of a second order system with a zero $\omega_z = 0.01Hz$, left, and no zero, right, for $\omega_n = 1Hz$ and $\zeta = 0.05$

Equation (8.6-1) will be used to represent a velocity function in the stability analysis. It will also be helpful to see the linear distance an object with this velocity travels. To find the distance, the velocity function is integrated in the time domain, or multiplied by $1/s$ in the frequency domain

$$\frac{1}{s}\cdot G_2(s)=G_3(s)=K_0\cdot\frac{1}{s}\cdot\frac{\frac{s}{\omega_z}+1}{\frac{s^2}{{\omega_n}^2}+\frac{2\cdot\zeta\cdot s}{\omega_n}+1} \tag{8.6-3}$$

and Figure 8-25 shows a plot of equation (8.6-3)

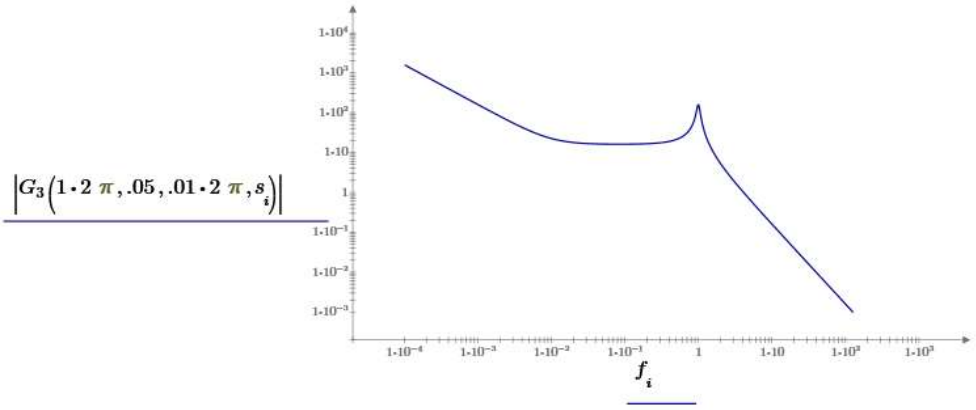

Figure 8-25 Plot of the velocity and distance functions

The step response for equation (8.6-3), as calculated by Mathcad, is given by

$$\mathcal{L}^{-1}\left(\frac{1}{s}\cdot G_3(s)\right)=\mathcal{L}^{-1}\left(\frac{1}{s^2}\cdot\frac{\frac{s}{\omega_z}+1}{\frac{s^2}{\omega_n{}^2}+\frac{2\cdot\zeta\cdot s}{\omega_n}+1}\right)=$$

$$\alpha_{out}(t)\Big|_{step}=\left(\begin{array}{l}\dfrac{\left(2\cdot\zeta^2-1\right)\cdot\omega_n\cdot\omega_z-\zeta\cdot\omega_n{}^2}{\omega_n\cdot\omega_z\cdot\sqrt{(-\zeta^2+1)\cdot\omega_n{}^2}}\cdot e^{-(\zeta\cdot\omega_n\cdot t)}\cdot\sin\left(t\cdot\sqrt{(-\zeta^2+1)\cdot\omega_n{}^2}\right)+\\ +\dfrac{2\cdot\zeta\cdot\omega_z-\omega_n}{\omega_n\cdot\omega_z}\cdot e^{-(\zeta\cdot\omega_n\cdot t)}\cdot\cos\left(t\cdot\sqrt{(-\zeta^2+1)\cdot\omega_n{}^2}\right)+\dfrac{\omega_n\cdot\omega_z\cdot t+\left(\omega_n-2\cdot\zeta\cdot\omega_z\right)}{\omega_n\cdot\omega_z}\end{array}\right) \tag{8.6-4}$$

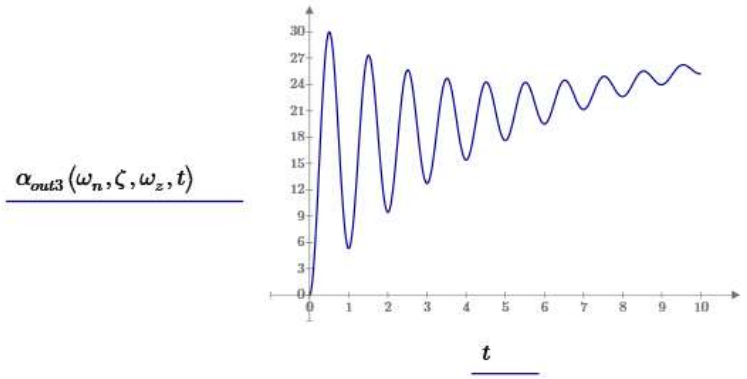

Figure 8-26 Plot of the second order step response for equation (8.6-3) for $\omega_n = 1Hz$ and $\zeta = 0.05$ with the zero $\omega_z = 0.01Hz$

Because there is a small offset in the step response of equation (8.6-1), the step response of the integral of equation (8.6-1) has an initial step and a long term drift due to the pole added by the integration.

9 Appendix 4 - Mapping Between 3-Dimensional Coordinate Systems

Although the dynamic stability model presented here is a 2-dimensional model, the rocket that is used to collect data to verify the model flies in 3-dimensional space. If the rocket has minimal z-axis spin and the rocket flies in a single plane, the 2-D model is an accurate model of its dynamic behavior. But to be accurate, even with minimal spin, the motion of the actual rocket flight must first be determined in 3-dimensions and then mapped to 2-dimensions.

In the 2-D system, the rocket can only rotate only about a single axis. A rotation through a single angle is all that is required to map the rocket axis into the ground frame axis system. In the 3-D system, the mapping from then x-y-z rocket axis system to the ground-based X-Y-Z system, is not as simple. As shown in Figure 9-1, the rocket can rotate about all three axes in the rocket frame of reference, and since the x-y-z axis system follows the rocket, the x-y-z axes can be in any orientation in the ground X-Y-Z coordinate system. There are several methods for determining the location of a coordinate point in one axis system in the other rotated coordinate system. Quaternions, one method, does the translation in a single rotation step. Euler's angles does the translation in three orthogonal rotations through two intermediate axis systems. Quaternions have advantages, including computational efficiency and a lack of singularities. Euler's angles, used here, are easier to understand and work fine for post-processing flight data.

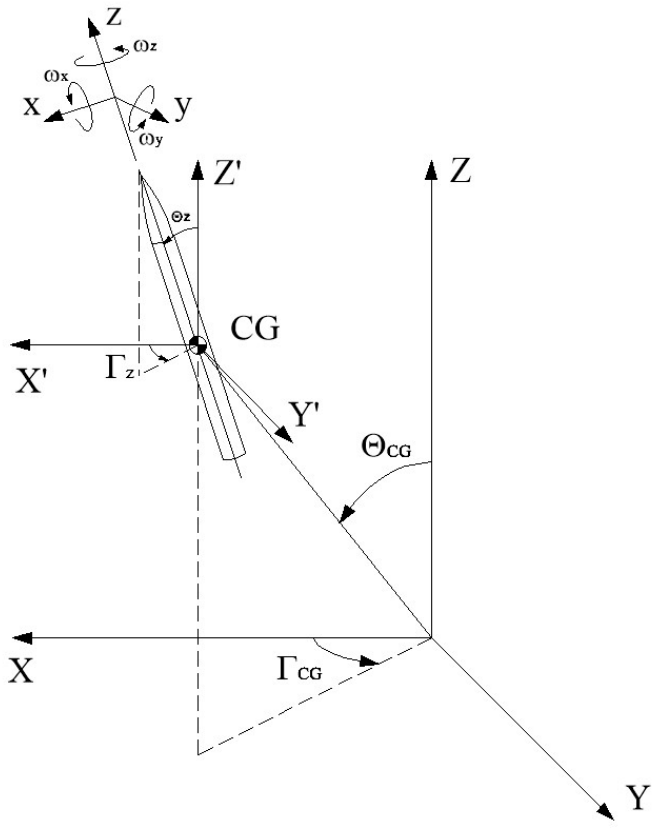

Figure 9-1 Orientation of the rocket in 3-dimensional space

Using Euler's angles, it takes three separate rotations to map between two 3-dimensional coordinate systems at arbitrary orientations relative to each other. Each rotation is described by an angle, so it takes three rotation angles to describe the orientation of one axis system relative to the other. Those rotation angles are called the Euler's angles and are denoted ϕ, θ, and ψ. The equations that are used to map between two coordinate systems are called Euler's angle equations.

Rotating an object about its x, y, and z-axes will result in a different final orientation depending upon the order in which the rotations are done. For a given rotation angle about each axis, the order sequence, x-y-z, y-x-z, or z-x-y, will result in different final locations for each sequence. The same order of rotation must be used to end up in the same final orientation each time a sequence is done. Therefore, the equations that are used to map between 3-D coordinate systems are unique to the order of each of the intermediate axis rotations used to derive the angle equations. A different order will result in a different set of Euler's equations and angles. For Euler's angles to work, the same rotational order used to derive the Euler's angles equations must then be used to translate between the two axis systems using those angles.

Three sets of three equations are needed when using Euler's angles. The first two sets of equations are used to translate a coordinate point between two rotated coordinate systems using Euler's angles. The third set of equations is used to find Euler's rotation angles for the current orientation of the two axes systems. The order convention means that all three sets of equations must have been derived using the same order of rotation convention.

There are numerous sources that cover the derivation of Euler's angles[33] that offer good explanations of the derivation. The equations used here are based upon the order of rotation conventions used in *Spacecraft Dynamics & Control*[34] in the order of rotation: ϕ about x, θ about y, and ψ about z.

Euler's equations translate the coordinates of a point in one axis system into the coordinates of that point in a second axis system, where the two axis systems can be at any spatial orientation relative to each other, as described by Euler's angles. This first set of Euler's equations map a point, (x, y, z) in the rocket frame, into a point (X, Y, Z) in the ground frame.

---

[33] Two examples are (Thomson, 1986, p. Chapter 3) and (Sidi, 2002, p. Appendix A)

[34] (Sidi, 2002, p. 321)

$$X_{Euler}(x,y,z) = (\cos\theta\cos\psi)\cdot x + (\cos\psi\sin\theta\sin\phi - \cos\phi\sin\psi)\cdot y + (\sin\psi\sin\phi + \cos\psi\cos\phi\sin\theta)\cdot z$$

$$Y_{Euler}(x,y,z) = (\cos\theta\sin\psi)\cdot x + (\sin\theta\sin\psi\sin\phi + \cos\psi\cos\phi)\cdot y + (\cos\phi\sin\theta\sin\psi - \cos\psi\sin\phi)\cdot z \quad (9.1\text{-}1)$$

$$Z_{Euler}(x,y,z) = (-\sin\theta)\cdot x + (\cos\theta\sin\phi)\cdot y + (\cos\theta\cos\phi)\cdot z$$

Conversely, a point in the ground frame can be mapped to the rocket frame by the second set of Euler's equations.

$$x_{Euler}(X,Y,Z) = (\cos\theta\cos\psi)\cdot X + (\cos\theta\sin\psi)\cdot Y - (\sin\theta)\cdot Z$$

$$y_{Euler}(X,Y,Z) = (\cos\psi\sin\theta\cdot\sin\phi - \cos\phi\sin\psi)\cdot X + (\sin\theta\sin\psi\sin\phi + \cos\psi\cos\phi)\cdot Y + (\cos\theta\sin\phi)\cdot Z$$

$$z_{Euler}(X,Y,Z) = (\sin\psi\sin\phi + \cos\psi\cos\phi\sin\theta)\cdot X + (\cos\phi\sin\theta\sin\psi - \cos\psi\sin\phi)\cdot Y + (\cos\theta\cos\phi)\cdot Z \quad (9.1\text{-}2)$$

The equations above require knowing Euler's angles at any moment in time. As the rocket rotates about its axes, the axes follow it, so the rocket axes are rotating in the ground-based frame of reference, and the Euler's angles are changing continuously. The sensor that is used to determine the rate of rotation is a rate gyroscope. A rate gyroscope provides the rate of rotation, ω, about each of the rocket's three axes, *x*, *y*, and *z*.

The rotation rate version of Euler's angles[35] are used to find Euler's angles. They determine the change in Euler's angles in terms of the rate of rotation about each of the rocket's x, y, and z-axes, ω_x, ω_y, and ω_z, the output of the rate gyroscope. Based on the same order convention used above, the continuous time version of these equations is

$$\frac{d\phi}{dt} = \omega_x + \frac{\sin\theta\sin\phi}{\cos\theta}\cdot\omega_y + \frac{\cos\phi\sin\theta}{\cos\theta}\cdot\omega_z$$

$$\frac{d\theta}{dt} = \cos\phi\cdot\omega_y - \sin\phi\cdot\omega_z \quad (9.1\text{-}3)$$

$$\frac{d\psi}{dt} = \frac{\sin\phi}{\cos\theta}\cdot\omega_y + \frac{\cos\phi}{\cos\theta}\cdot\omega_z$$

[35] These rotation rate equations are consistent with the conventions used above, but the derivation is shown in (Thomson, 1986, p. 38) using a different order of rotation convention

The rate equations give the continuous rate of change of Euler's angles for continuous rotation rates about each of the x, y, and z axes. If the rate of rotation about each of the axes is measured continuously from a known starting orientation, then the absolute orientation of the rocket axis system can be determined at any instant in time. Because the rotation about each of the three axes is being measured continuously, the order of rotation no longer matters, as the angular change about each of the axes in any instant of time approaches zero.

To find Euler's angles at any point in time, t_1, the rate equation is integrated, or summed continuously, from the starting point to that point in time

$$\psi(t_1) = \int_0^{t_1} \frac{d\psi(t)}{dt} dt \tag{9.1-4}$$

The rate gyro measures the rotation rate at a fixed sample rate, for example, 100 samples per second. If the sample rate is fast compared to the rate of rotation, it effectively looks like a continuous time measurement, that is, the sample rate must be much greater than the bandwidth of the rocket's rotational dynamics.

The data is handled as a discrete time system, so the continuous time differential equations become discrete time difference equations. To solve for Euler's angles from the change in Euler's angles, a discrete time integration is used where

$$\frac{d\psi}{dt} \rightarrow \frac{\Delta\psi}{\Delta t}$$

and

$$\Delta t = t_{samp} = t_n - t_{n-1}$$

And the integration is a continuous running sum

$$\psi = \psi + \Delta\psi \cdot t_{samp}$$

$$\phi = \Delta\phi + \phi \cdot t_{samp}$$

$$\theta = \theta + \Delta\theta \cdot t_{samp}$$

which leads to the solution for Euler's angles at each data point, *n*

$$\psi_n = \psi_{n-1} + \left[\frac{\sin\phi_{n-1}}{\sin\theta_{n-1}} \cdot \omega_{xn} + \frac{\cos\phi_{n-1}}{\sin\theta_{n-1}} \cdot \omega_{yn} \right] \cdot (t_n - t_{n-1})$$

$$\phi_n = \phi_{n-1} + \left[-\frac{\sin\phi_{n-1}\cos\theta_{n-1}}{\sin\theta_{n-1}} \cdot \omega_{xn} - \frac{\cos\phi_{n-1}\cos\theta_{n-1}}{\sin\theta_{n-1}} \cdot \omega_{yn} + \omega_{zn} \right] \cdot (t_n - t_{n-1}) \qquad (9.1\text{-}5)$$

$$\theta_n = \theta_{n-1} + \left[\cos\phi_{n-1} \cdot \omega_{xn} - \sin\phi_{n-1} \cdot \omega_{yn} + \omega_{zn} \right] \cdot (t_n - t_{n-1})$$

where $\psi_0 = 0$, $\phi_0 = 0$, and $\theta_0 = 0$. Once the value of Euler's angles are determined for each point in time as the rocket rotates about each of its axes, the location of any coordinate point in the rocket frame can be determined in the ground frame by using equations (9.1-1), and any coordinate point in the ground frame can be determined in the rocket frame by using equations (9.1-2).

The orientation of the rocket's z-axis in the X-Y-Z axis system can be used to determine the orientation of the rocket for an observer on the ground. Figure 9-2 shows an example of the path the tip of the nosecone takes during the rocket's flight. That point is determined by plotting the coordinate point (X,Y,Z) in the ground frame where (X,Y,Z) is determined by solving equations (9.1-1) for (x,y,z) = (0,0,1), or the unit vector of the z-axis of the rocket, U_z. For the z-axis unit vector, the equations (9.1-1) become

$$U_{zX} = X_{Euler}(0,0,1) = \sin\theta\sin\psi$$

$$U_{zY} = Y_{Euler}(0,0,1) = -\sin\theta\cos\psi \qquad (9.1\text{-}6)$$

$$U_{zZ} = Z_{Euler}(0,0,1) = \cos\theta$$

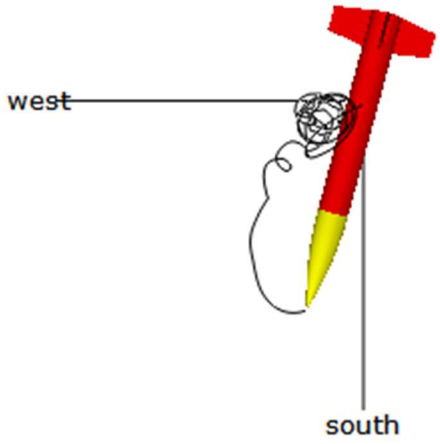

Figure 9-2 Visualization of the spherical path taken by the tip of the rockets nosecone during flight looking down toward the ground from above (SpeedRunner 75 5/21/2016)

The rotation of the rocket about its z-axis (spin) can be determined by either the x or the y-axis unit vector. Other quantities, such as distance, velocity, and acceleration, can also be translated between the frames of reference using Euler's angles.

Polar coordinates are used to describe the orientation of the rocket using the flight data. The 3-D angle of the rocket from vertical that is equivalent to the 2-D angle, α_y is calculated by finding the polar coordinates of the rocket's z-axis unit vector. Once the X, Y, and Z values are determine for the z-axis unit vector from equations (9.1-6), then its polar coordinates can be found.

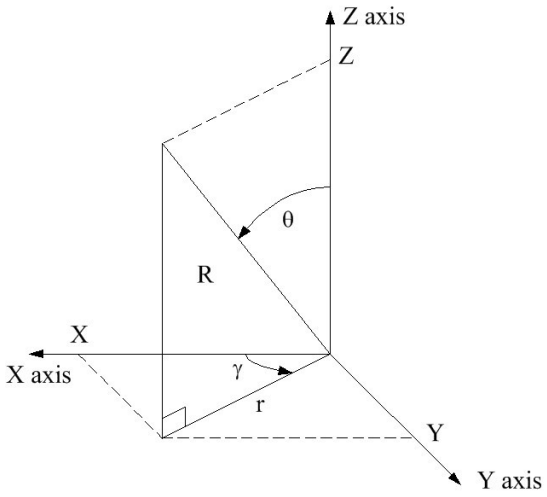

Figure 9-3 Spherical & Cartesian Coordinates

To go from Cartesian to spherical coordinates

$$r = \sqrt{X^2 + Y^2} \tag{9.1-7}$$

$$R = \sqrt{Z^2 + r^2} = \sqrt{X^2 + Y^2 + Z^2} \tag{9.1-8}$$

Then, the polar coordinates are

$$\Theta = \arcsin\frac{r}{R} = \arcsin\frac{\sqrt{X^2 + Y^2}}{\sqrt{X^2 + Y^2 + Z^2}} \tag{9.1-9}$$

$$\Gamma = \arcsin\frac{Y}{\sqrt{X^2 + Y^2}} \tag{9.1-10}$$

where Θ is the 3-D equivalent of the 2-D α_y.

10 Appendix 5 - Coupled Damping Comparison to LaBudde's Model

This summary shows the difference in nomenclature used by LaBudde[36] and this paper for calculating the coupled natural frequency and damping ratio. Both use Mandell's definition for C_1 and C_2, and a different definition of C_3. But once both sets of expressions are evaluated in terms of the rocket parameters, the expressions for the coupled natural frequency and damping ratios are the same.

Mandell/Barrowman Uncoupled

$$C_1 := \frac{\theta}{2} \cdot A_r \cdot C_{N\alpha} \cdot v_T^{\,2} \cdot (L_{CP} - L_{CG})$$

$$C_2 := \frac{\theta}{2} \cdot A_r \cdot C_{N\alpha} \cdot (L_{CP} - L_{CG})^2 \cdot v_T$$

$$\omega_n := \sqrt{\frac{C_1}{I_L}} \rightarrow \frac{\sqrt{2} \cdot \sqrt{\frac{A_r \cdot C_{N\alpha} \cdot v_T^{\,2} \cdot \rho \cdot (L_{CP} - L_{CG})}{I_L}}}{2}$$

$$\zeta := \sqrt{\frac{C_2^{\,2}}{4 \cdot C_1 \cdot I_L}} \rightarrow \frac{\sqrt{2} \cdot \sqrt{\frac{A_r \cdot C_{N\alpha} \cdot \rho \cdot (L_{CP} - L_{CG})^3}{I_L}}}{4}$$

LaBudde Coupled

$$C_3 := \frac{\frac{\theta}{2} \cdot A_r \cdot C_{N\alpha} \cdot v_T}{m_o} \qquad \text{assuming } v_Z = v_T$$

$$\omega_n'' := \sqrt{\frac{C_1 + C_2 \cdot C_3}{I_L}} \xrightarrow{simplify} \sqrt{\frac{A_r \cdot C_{N\alpha} \cdot v_T^{\,2} \cdot \rho \cdot (L_{CP} - L_{CG}) \cdot ((A_r \cdot C_{N\alpha} \cdot L_{CP} - A_r \cdot C_{N\alpha} \cdot L_{CG}) \cdot \rho + 2 \cdot m_o)}{4 \cdot I_L \cdot m_o}}$$

$$\zeta'' := \sqrt{\frac{(C_2 + C_3 \cdot I_L)^2}{4 \cdot (C_1 + C_2 \cdot C_3) \cdot I_L}} \xrightarrow{simplify} \sqrt{\frac{A_r \cdot C_{N\alpha} \cdot \rho \cdot \left(\left(L_{CP}^{\,2} - 2 \cdot L_{CG} \cdot L_{CP} + L_{CG}^{\,2}\right) \cdot m_o + I_L\right)^2}{4 \cdot I_L \cdot m_o \cdot (L_{CP} - L_{CG}) \cdot ((A_r \cdot C_{N\alpha} \cdot L_{CP} - A_r \cdot C_{N\alpha} \cdot L_{CG}) \cdot \rho + 2 \cdot m_o)}}$$

Fetter Coupled

$$C_3 := \frac{\theta}{2} \cdot A_r \cdot C_{N\alpha} \cdot v_T^{\,2}$$

$$C_1' := C_1 + \frac{C_2 \cdot C_3}{v_T \cdot m_o} \qquad C_2' := C_2 + \frac{I_L \cdot C_3}{v_T \cdot m_o}$$

$$\omega_n' := \sqrt{\frac{C_1'}{I_L}} \xrightarrow{simplify} \sqrt{\frac{A_r \cdot C_{N\alpha} \cdot v_T^{\,2} \cdot \rho \cdot (L_{CP} - L_{CG}) \cdot ((A_r \cdot C_{N\alpha} \cdot L_{CP} - A_r \cdot C_{N\alpha} \cdot L_{CG}) \cdot \rho + 2 \cdot m_o)}{4 \cdot I_L \cdot m_o}}$$

$$\zeta' := \sqrt{\frac{C_2'^{\,2}}{4 \cdot C_1' \cdot I_L}} \xrightarrow{simplify} \sqrt{\frac{A_r \cdot C_{N\alpha} \cdot \rho \cdot \left(\left(L_{CP}^{\,2} - 2 \cdot L_{CG} \cdot L_{CP} + L_{CG}^{\,2}\right) \cdot m_o + I_L\right)^2}{4 \cdot I_L \cdot m_o \cdot (L_{CP} - L_{CG}) \cdot ((A_r \cdot C_{N\alpha} \cdot L_{CP} - A_r \cdot C_{N\alpha} \cdot L_{CG}) \cdot \rho + 2 \cdot m_o)}}$$

[36] (LaBudde, 1999)

11 Key Variables

A_r	cross-sectional area of the rocket
C_1	rotational forcing coefficient
C_2	rotational damping coefficient
C_3	X-axis forcing coefficient
C_4	rotational velocity damping coefficient
C_1'	coupled forcing coefficient
C_2'	coupled damping coefficient
C_D	drag coefficient
$C_{L\alpha}$	lift coefficient
$C_{N\alpha}$	normal force coefficient
CP	center of pressure
CG	center of gravity
d_X	distance traveled along the ground frame X-axis
d_{Xss}	distance the rocket travels along the X-axis due to the small side-to-side motion
$d_{\alpha y}$	distance the rocket travels along the X-axis from the projection of the y-axis rotational velocity to the center of pressure
d_Z	distance traveled along the ground frame Z axis
F_D	the drag force – X and Y subscripts are used to denote the drag force along the X and Z axes
F_L	the lift force – X and Y subscripts are used to denote the lift force along the X and Z axes
F_N	the normal force
F_G	the force due to gravity
F_T	the thrust force – X and Y subscripts are used to denote the thrust force along the X and Z axes
g	acceleration due to gravity
$G_{\alpha y}$	rotational dynamics frequency domain gain function
$K_{\alpha y}$	dc gain of the linearized rotational dynamics frequency domain gain equation
K_{vX}	dc gain of the linearized X-axis frequency domain gain equation
I_L	longitudinal moment of inertia
L_{CP}	distance from the tip of the nosecone to the center of pressure

L_{CG} distance from the tip of the nosecone to the center of gravity

L_m length of the motor

L_{ne} length from the tip of the nosecone to the base of the rocket

m_o mass of the rocket

m_p mass of the propellant

M_R the total rotational moment about the center of the object – for the rocket, this would be the tip of the nosecone

M_{1y} rotational forcing moment

M_{2y} rotational damping moment

M_{2R} rotational jet damping moment

s complex frequency $s = j \cdot \omega$

t time

t_b burn time of the motor

U_{zX} the X-axis component of the z-axis unit vector in 3-dimensional space

U_{zY} the Y-axis component of the z-axis unit vector in 3-dimensional space

U_{Zz} the z-axis component of the Z-axis unit vector in 3-dimensional space

v_{CG} the velocity of the center of gravity of the rocket

v_T the velocity of the total oncoming airstream

v_w the velocity of the wind along the X-axis

v_X the velocity of the rocket along the X-axis

v_Z the velocity of the rocket along the Z-axis

v_{Xss} the small sinusoidal component of V_X due to coupling between the X-axis equation of motion and the rotational dynamics equation

v_Z the velocity of the rocket along the Z-axis

$v_{\omega y}$ the linear X-axis projection of the y-axis rotational velocity to the center of pressure

x, y, z axes in the rocket frame of reference

X, Y, Z axes in the inertial ground-based frame of reference

α_{at} angle of attack between the total oncoming airstream and the z-axis of the rocket

α_T angle from the Z-axis opposite the direction of the total oncoming airstream

α_y the angle indicating the total rotation about the y-axis axis. In the 2-D model, this is also the angle of the rocket's z axis measured from the Inertial Z axis as the y axis remains aligned with the Y axis

Δ	angle between the direction of travel of the center of gravity of the rocket and the direction the rocket is pointed
Γ	3-D polar coordinate angle of rotation about the Z-axis
ρ	density of air
θ_T	angle from the Z-axis of the angle of the total oncoming airstream
θ_{CG}	angle between the Z-axis and the direction of the movement of the center of gravity of the rocket
Θ	3-D polar coordinate angle from vertical in 3-dimensional space
ϕ, θ, ψ	Euler's angles of rotation
ω_{at}	rotation rate of the angle attack due to the rotational velocity used to calculate the rotational damping moment
ω_n	natural frequency of a second order system
ω_n'	coupled natural frequency of a second order system
ω_y	rate of rotation of the rocket axis frame about the y axis
ζ	damping ratio of a second order system
ζ'	coupled damping ratio of a second order system

12 References

Allen, H., & Perkins, E. (1951). *Characteristics of Flow Over Inclined Bodies of Revolution - RM A50L07.* NACA.

Barrowman, J. (1968). *TIR-33 Calculating the Center of Pressure of a Model Rocket.* Centuri Engineering Company.

Barrowman, J. (1970). *TIR-30 Stability of a Model Rocket In Flight.* Centuri Engineering Company.

Barrowman, J. S. (1967). *The Practical Calculation of the Aerodynamic Characteristics of Slender Finned Vehicles, Master's Thesis.* Washington, D.C.: The Catholic University of America.

Barrowman, J. S., & Barrowman, J. A. (1966). *The Theoretical Prediction of Center of Pressure, NARAM-8.* National Association of Rocketry.

Boyce, W. E., & DiPrima, R. C. (1969). *Elementary Differential Equations.* New York: John Wiley & Sons.

Davis, L., Follin, J. W., & Blitzer, L. (1958). *Exterior Ballistics of Rockets.* Princeton: D. Van Nostrand Company, Inc.

Feretich, B. (2015-2018). *http://www.rafresearch.com/rocketdatalogger/index.html*. Retrieved from RAF Research.

Fetter, T. (2014-2016). *Speedmotion Rockets*. Retrieved from http://speedmotionrockets.com/

Fetter, T. B. (2015, March/April-September/October). Flight Data Analysis using Excel. *Sport Rocketry*.

French, A. (1971). *Newtonian Mechanics.* New York: W.W. Norton & Companmy, Inc.

Galejs, R. J. (1999, May/June). What Barrowman Left Out. *Sport Rocketry*, pp. 17-19.

Gurkin, L. (1964). *Basic Missile Dynamic Stability, NARAM 6.* National Association of Rocketry.

LaBudde, E. V. (1999). *A Design Procedure for Maximizing Altitude Performance, NARAM 41.* National Association of Rocketry.

Liu, C., & Liu, J. W. (1975). *Linear Systems Analysis.* New York: McGraw-Hill.

Mandell, G. K. (1968-1969, Oct-Apr). Fundamentals of Dynamic Stability. *Model Rocketry Magazine*.

Mandell, G. K. (n.d.). *Fundamentals of Dynemic Stability, TR-201.* NARTS (National Association of Rocketry).

Mandell, G. K., Caporaso, G. J., & Bengen, W. P. (1973). *Topics in Advanced Model Rocketry.* Cambridge: MIT Press.

Mathcad Home Page. (n.d.). Retrieved from https://www.mathcad.com/en/

McCormick, B. W. (1995). *Aerodynamics Aeronautics and Flight Mechanics.* New York: John Wiley & Sons, Inc.

Micci, M. (1976). *Dynamic Stability Criteria for Model Rockets.* NAR.

Philips, C. (1979). *A Study of Rotational Motions in Rocket Flight Dynamics, NARAM 21.* NAR.

Roberge, J. (1975). *Operational Amplifiers Theory & Practice.* New York: John Wiley & Sons.

Sidi, M. J. (2002). *Spacecraft Dynamics & Control.* Cambridge University Press.

Thomson, W. T. (1986). *Introduction to Space Dynamics.* New York: Dover Publications, Inc.